The Astrophysical Journal, 894:109 (29pp), 2020 May 10 https://doi.org/10.3847/1538-4357/ab86bf

Magnetic Imprisonment of Dusty Pinballs by a Supernova Remnant

Brian J. Fry[1,2], Brian D. Fields[2,3], and and John R. Ellis[4,5,6]
[1] Department of Physics, United States Air Force Academy, Colorado Springs, CO 80840, USA
[2] Department of Astronomy, University of Illinois, Urbana, IL 61801, USA
[3] Department of Physics, University of Illinois, Urbana, IL 61801, USA
[4] Theoretical Physics and Cosmology Group, Department of Physics, King's College London, London WC2R 2LS, UK
[5] NICPB, Rävala pst. 10, 10143 Tallinn, Estonia
[6] Theory Division, Physics Department, CERN, CH-1211 Geneva 23, Switzerland
Received 2020 February 3; revised 2020 March 20; accepted 2020 April 4; published 2020 May 12

Abstract

Motivated by recent measurements of deposits of ^{60}Fe on the ocean floor and the lunar surface, we model the transport of dust grains containing ^{60}Fe from a near-Earth (i.e., within 100 pc) supernova (SN). We inject dust grains into the environment of an SN remnant (SNR) and trace their trajectories by applying a 1D hydrodynamic description assuming spherical symmetry to describe the plasma dynamics, and we include a rudimentary, 3D magnetic field description to examine its influence on charged dust grains. We assume the interstellar medium (ISM) magnetic fields are turbulent and are amplified by the SNR shock, while the SN wind and ejecta fields are negligible. We examine the various influences on the dust grains within the SNR to determine when/if the dust decouples from the plasma, how much it is sputtered, and where within the SNR the dust grains are located. We find that Rayleigh–Taylor instabilities are important for dust survival, as they influence the location of the SN's reverse shock. We find that the presence of a magnetic field within the shocked ISM material limits the passage of SN dust grains, with the field either reflecting or trapping the grains within the heart of the SNR. These results have important implications for in situ ^{60}Fe measurements and for dust evolution in SNRs generally.

Unified Astronomy Thesaurus concepts: Supernova dynamics (1664); Supernovae (1668); Astrophysical dust processes (99); Interstellar dust processes (838); Supernova remnants (1667)

Supporting material: animation

1. Introduction

Supernovae (SNe) are some of both the most destructive and creative events in the universe. An SN explosion blasts apart a massive star, and its outward propagating shock wave shatters dust grains floating in the interstellar medium (ISM). However, the explosion also leads to the formation of a new compact object, creates heavy elements beyond iron and nickel, and, as the SN remnant (SNR) expands, new dust grains condense from within the ejecta. This clash of simultaneously destroying and creating dust raises the question whether SN are net producers or demolishers of dust.

Looking at another facet of SNe: they are estimated to occur at a rate of 1–3 per century within the Milky Way (e.g., Adams et al. 2013, and references therein), and, given the size of the Milky Way, this suggests that one (probably more) has occurred close enough to have produced detectable effects on Earth. These effects could range from delivery of SN material onto the Earth's surface to biological effects. Studies of the possible biological effects of a near-Earth SN have a long history in the literature (e.g., Shklovskij 1969; Alvarez et al. 1980; Ellis & Schramm 1995; Melott et al. 2017; Fields et al. 2019), but the delivery of SN material onto Earth has only more recently been examined, first by Ellis et al. (1996; see also Korschinek et al. 1996), who suggested looking for long-lived radioactive isotopes ($\tau_{1/2} \sim$ Myr) such as ^{60}Fe and ^{244}Pu, whose presence would constitute direct evidence of such an event, since these isotopes are not manufactured within the solar system, and any pre-solar isotopes would have decayed by today (see also Korschinek & Faestermann 2019).

The first evidence for such extra-solar radioisotopes was found by Knie et al. (1999) in a sample of ferro-manganese (Fe-Mn) crust from Mona Pihoa in the South Pacific. Knie et al. used accelerator mass spectrometry (AMS) to find an anomaly in ^{60}Fe concentration that suggested that an SN occurred near Earth sometime within the last 5 Myr (the time within this range could not be specified). This study was later confirmed by Knie et al. (2004) using a different Fe-Mn crust sample from the equatorial Pacific Ocean floor, which found a distinct signal in ^{60}Fe abundance ~2.2 Myr ago. Later, Fitoussi et al. (2008) also found an ^{60}Fe signal in the Fe-Mn crust, but analysis of sea sediment samples from the northern Atlantic Ocean found no clear signal. Fitoussi et al. noted several reasons for the discrepancy, including variations in the background and differences in the uptake efficiencies between the Fe-Mn crust and sediment, or a signal duration much longer (and hence diluted) than the then-expected timescale of ~few kyr. Subsequently, results from Eltanin sediment samples from the southern Indian Ocean were reported in Feige (2014), confirming the Knie et al. (2004) Fe-Mn crust detection in these sea sediment samples. Most recently, Wallner et al. (2016), using AMS but in a different laboratory and with different samples, also found ^{60}Fe in Fe-Mn crusts and nodules, confirming the 2–3 Myr signal but also reporting evidence for a *second* signal at ~6–8 Myr. Wallner et al. (2016) also detected ^{60}Fe in several deep-ocean sediments, again finding the earlier signal, while measuring a deposition timescale of ≈1 Myr, consistent with the Fitoussi et al. (2008) result. Ludwig et al. (2016) detected ^{60}Fe in sediments by isolating the isotope from iron-bearing microfossils; they confirmed the deposition timescale ~1 Myr.

We note also that cosmic-ray studies by Kachelrieß et al. (2015) and Savchenko et al. (2015) found a signature in the

proton cosmic-ray spectrum suggesting an injection of cosmic-rays associated with an SN occurring ∼2 Myr ago, and the discovery of ^{60}Fe in cosmic-rays by Binns et al. (2016) suggest an SN origin within the last ∼2.6 Myr located $\lesssim$1 kpc of Earth, based on the ^{60}Fe lifetime and cosmic-ray diffusion. Additionally, lunar regolith samples (Cook et al. 2009; Fimiani et al. 2012, 2014, 2016) have also shown an excess of ^{60}Fe; although, only the presence of an excess is detectable, not the precise arrival time or fluence (Feige et al. 2013) because of the nature of the regolith. However, Fry et al. (2016) suggested the use of lunar regolith radioisotope distributions with lunar latitude as an "antenna" to find the direction to the source of the ^{60}Fe material.

Many studies have thus confirmed the 2–3 Myr ^{60}Fe signal, using a variety of sampling techniques from around the Earth and on the Moon. All sediment studies are consistent with a ∼1 Myr deposition time. It is thus well-established that (at least one) recent near-Earth SN deposited its ejecta on the Earth and Moon. On the other hand, different papers have reported fluences that have varied by an order of magnitude. The study by Fry et al. (2016) found that terrestrial atmospheric and oceanic processes could explain such differences in the fluence values between these studies, including the weak signal in the Fitoussi et al. sediment sample.

The possible nucleosynthesis site of the ^{60}Fe material was most thoroughly examined by Fry et al. (2015), who considered all known astrophysical sources of ^{60}Fe (including core-collapse SNe, neutron-star mergers, and thermonuclear/Type Ia SNe). They found that core-collapse SNe are excellent candidates; in particular, they found that an Electron-Capture SN (ECSN) arising from a Zero-Age Main Sequence (ZAMS) mass ≈8–10 $M_\odot$ ("$\odot$" refers to the Sun) to be the most likely progenitor. However, they were not able to rule out completely a Super Asymptotic Giant Branch (SAGB) star with a ZAMS mass ≈6.5–9 $M_\odot$ as a possible source, based on nucleosynthesis criteria alone. For this work, we will assume that the ^{60}Fe source is a core-collapse SN, and we will highlight the ECSN case.

With regards to the location of the ^{60}Fe-producing SN, Benítez et al. (2002) suggested that the source event occurred in the Sco–Cen OB association. This association was ∼130 pc away at the time of the ^{60}Fe-producing event, and its members were described in detail by Fuchs et al. (2006). Breitschwerdt et al. (2012, 2016), Feige (2016), Feige et al. (2017), and Schulreich et al. (2017, 2018) have modeled the formation of the Local Bubble and used hydrodynamic simulations to model SNe occurring within the Sco–Cen association and to track the ^{60}Fe dust entrained within the blast. Comparably, Sørensen et al. (2017) examined SN activity in open clusters within 1000 pc of Earth over the past 35 Myr and found several passing within 200 pc of Earth. Mamajek (2016) suggested that the Tuc–Hor group, which was within ∼60 pc of Earth at the time of the ^{60}Fe-producing event, could have provided an ECSN, based on the masses of the current group members. Hyde & Pecaut (2018) considered both the Sco–Cen and Tuc–Hor sites and found that Tuc–Hor could be the site of either the 2–3 or 6–8 Myr ago events, but they argued that the 2–3 Myr ago event arose from the Upper Centaurus Loop component of Sco–Cen, assigning the earlier event to Tuc–Hor. Additionally, Neuhäuser et al. (2019) sought to link the arrival of ^{60}Fe with a runaway star, finding that one runaway-pulsar-pair met their criteria; although, there was a discrepancy between the time of the ^{60}Fe signal peak (∼2.2 Myr ago) and the time of common distance (1.78 ± 0.21 Myr ago).

With regard to the deposition of SN ^{60}Fe on Earth, Fields et al. (2008) used hydrodynamic models to show that for plausible SN distances, the SNR plasma cannot penetrate the solar wind to 1 au. However, SN radioisotopes including ^{60}Fe are generally in refractory elements that readily form dust (Benítez et al. 2002). Athanassiadou & Fields (2011) and Fry et al. (2016) showed that SN material in the form of dust can have sufficient mass and velocity to overcome the solar wind and reach Earth. The ^{60}Fe detections thus imply that at least some SN iron was condensed into dust grains and survived passage to the solar system while still retaining high enough mass and velocity to pass within 1 au of the Sun. In the broader context of the nature of SNe, this raises the following question: *How can an SN, which is quite proficient at destroying dust, transport dust material effectively across light-years of interstellar space to the solar system without destroying it?*

Many studies have examined general dust processing (e.g., Dwek & Arendt 1992; Draine 2003, and references therein) and within an SNR, in particular (Nozawa et al. 2006, 2007; Kozasa et al. 2009). Several studies consider only one type of action such as formation (Cherchneff & Dwek 2009, 2010; Cherchneff & Sarangi 2011; Cherchneff 2013; Dwek 2016) or examine only one process such as charging (Lafon et al. 1981; Draine & Sutin 1987; Barkan et al. 1994) or sputtering (Scalo et al. 1977; Shull 1977; Tielens et al. 1987; Dwek et al. 1996; Jones et al. 1996; Janev et al. 2001). Other studies have focused on a specific event within the grain's journey in the SNR, such as the passage of the reverse shock (RS; Silvia et al. 2010, 2012; Biscaro & Cherchneff 2016). More comprehensive studies such as Nozawa et al. (2007), Nath et al. (2008), Bocchio et al. (2016), and Micelotta et al. (2016) follow the grains through the entire SNR but do not include magnetic fields, which could potentially affect the trajectory of the grains within the SNR.

To date, studies of near-Earth SNe, (e.g., Athanassiadou & Fields 2011; Fry et al. 2015, 2016; Breitschwerdt et al. 2016; Feige 2016; Feige et al. 2017; Schulreich et al. 2017) have assumed that the ^{60}Fe material would be coupled to the SNR plasma and most likely confined to the leading edge of the SNR. This paper relaxes this assumption, allowing the grains to decouple from the SNR plasma earlier in the SNR evolution, potentially escaping the SNR. We utilize a similar approach to that conducted by Nozawa et al. (2007), Nath et al. (2008), Micelotta et al. (2016), and Bocchio et al. (2016), namely, applying a hydrodynamic simulation of the SN evolution, then examining dust processes from those conditions. However, we include grain charging, a rudimentary treatment of the SNR's magnetic field (specifically, the ISM magnetic field) and examine the specific case of ^{60}Fe-containing dust grains from a near-Earth SN. Our work assumes the magnetic fields in the SN ejecta and stellar wind are negligible for the purpose of dust propagation; including those fields would only reinforce our main conclusions.

We find that:

1. Magnetic fields (specifically, the shocked ISM field) dominate the fate of larger Fe grains ($a_{\rm gr} \gtrsim 0.05\ \mu$m), effectively confining them within the inner SNR, while drag dominates the fate of smaller Fe grains, eventually slowing them to the SNR plasma velocity.

2. Dust grains exhibit "*pinball*" behavior due to magnetic reflections, and they ricochet in the interior of the SNR.
3. The inclusion of Rayleigh–Taylor instabilities is important, since the earlier passage of the RS exposes the dust grains to erosion and drag for a longer time period.
4. Grain propagation studies omitting the effects of grain–grain collisions and shock encounters may be missing important grain influences.
5. Our results indicate that the Sco–Cen association could not have hosted the SN progenitor, because the SN would not have been able to push the ISM magnetic field, $\boldsymbol{B}_{\rm ISM}$, beyond the solar system so as to allow the ^{60}Fe-containing dust grains to penetrate the solar system and reach Earth.
6. The Tuc–Hor association is still a possible source for the ^{60}Fe.

Our findings also suggest that earlier assumptions of dust grains being entrained in the leading edge of the SNR (e.g., Fry et al. 2015; Breitschwerdt et al. 2016; Feige 2016; Feige et al. 2017; Schulreich et al. 2017) are not appropriate.

2. SNR Evolution

An SNR will transition through four main phases as it evolves (Ostriker & McKee 1988; Padmanabhan 2001; Draine 2011; Janka et al. 2016). The first phase is free expansion, and it is characterized by a constant velocity after the explosion. The ejected material moves outward supersonically and produces a shock wave in the surrounding, ambient material (hereafter referred to as the "forward shock" or FS). The presence of an ambient medium causes the ejected material to slow down, but in the early phases of expansion, when the mass of the ejected material far exceeds that of the swept-up ambient material, this deceleration is negligible when examining the expansion of the FS. However, this slight deceleration creates a second shock wave (hereafter referred to as the "reverse shock" or RS), which communicates the presence of the ambient medium to the ejected material. Analytic solutions to this phase were found by Chevalier (1982), Chevalier et al. (1992), and Nadezhin (1985; referred to as Chevalier–Nadezhin); these self-similar solutions yield good descriptions for the position of the FS and incorporate the presence of an RS. In the free expansion phase, both the forward and reverse shocks are moving outward.

There are, however, some difficulties with the Chevalier–Nadezhin solutions. First, at the interface (also known as the contact discontinuity) between the ejecta and ambient medium, the Chevalier–Nadezhin density profile solutions produce singularities (resulting in either an infinite or zero density depending on the density profile of the ambient medium). Both cases are unphysical and, if one attempted to examine dust dynamics in such a state, the grain would encounter an imaginary wall or vacuum. Additionally, the Chevalier–Nadezhin solutions ignore the presence of Rayleigh–Taylor instabilities along the RS. Rayleigh–Taylor instabilities drive the RS further inward (Herant & Woosley 1994; Blondin & Ellison 2001; Blondin 2001) and, when considering dust, the location of the RS is of extreme importance since its passage shatters grains and exposes them to the hot SNR material.

As the FS sweeps up more material, the SNR transitions into the second, Energy-/Adiabatic-Conserving, phase. This phase is often called the Sedov–Taylor phase after Sedov (1959) and Taylor (1950) who found self-similar descriptions of the expansion. When the swept-up material is approximately equal in mass to the ejecta material, the RS will cease moving outward and be driven inward, deeper into the ejecta, eventually proceeding all the way to the center of the SNR. Studying dust dynamics during the Sedov–Taylor phase would be fairly straightforward, since the plasma density, velocity, and pressure within the SNR are described smoothly. However, because the dust grains are initially formed during the free expansion phase, a description that includes a transition between phases is required. Truelove & McKee (1999) found analytic solutions for this transition, describing the positions of the FS and RS through both phases. However, these do not include descriptions of the plasma properties needed to describe the grain dynamics (except as initial conditions) and ignore the effects of Rayleigh–Taylor instabilities along the RS.

As the SNR expands and cools, ions within the SNR shell will combine with electrons and radiate photons. As the SNR outer shell becomes radiative, the FS will lose thermal pressure support and the expansion will be determined by the momentum within the shell (Blondin et al. 1998; Draine 2011). This third phase is the Momentum-Conserving phase, with the SNR shell slowing as it collects more surrounding material (this phase is also referred to as the "snowplow" phase because of this accumulating action). The snowplow phase typically begins around 50,000 yr after the SN explosion, but, since the typical grain lifetime is around 100,000 yr (Draine 2011), a detailed examination of the grain properties at the end of the Sedov–Taylor phase will be needed first, since the dust could be severely (possibly completely) ablated before reaching the snowplow phase.

Eventually, the FS will slow to the sound speed of the ambient medium. At this point, the SNR effectively stops expanding, and the SNR enters the fade-away phase as the shock transitions to a sound wave in the ambient medium. The SNR will eventually be dispersed through random processes in the ISM. Any dust grains that survive to this stage will behave the same as they would in the general ISM.

Before specifying the SNR environment we assume, we first mention the quantities of the SNR environment we require in order to describe accurately the dynamics of our dust grains. Section 3 will describe in much greater detail why these quantities are important. The density, velocity, and temperature (and how they evolve with time) within the SNR are required, as these determine the drag experienced by the grains as well as the degree of erosion by the plasma. The composition of the plasma should also be detailed, since larger ions such as O/Si/S in sufficient concentrations can enhance erosion beyond that due to H and He. The grain's charge and the direction and strength of the SNR magnetic field are important since dust grains spiraling around magnetic field lines could potentially become trapped within the SNR, as we discuss in Section 3.1.2 below. The charge is dependent on the material of the dust grain, which is itself dependent on where the dust is formed within the ejecta. Finally, the location of the dust grain's birthplace in the ejecta is significant, since it also affects when it will encounter the RS and its initial position and velocity.

3. Grain Processes

We first examine the influences acting on the dust grain. The radioisotopes will be formed deep within the ejecta; as the SNR expands, the ejecta will cool, and overdensities in the ejecta will form clouds (also referred to as clumps; Silvia et al. 2010, 2012).

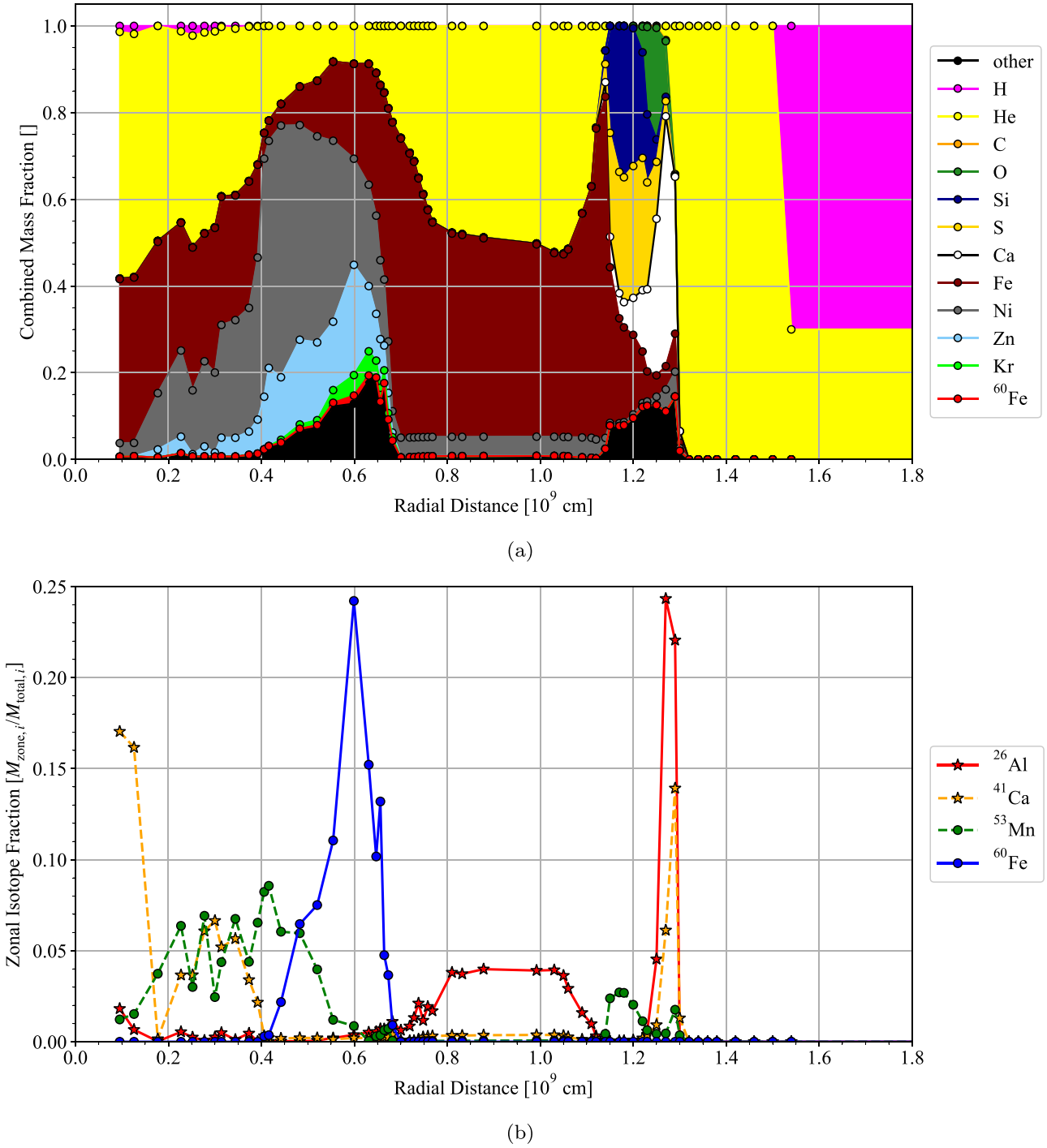

Figure 1. Nucleosynthesis products within each zone. The upper panel shows the mass fractions for the main stable nucleosynthesis products, and the lower panel shows the relative distribution of the main radioisotopes. Note that the mass fractions for each element are stacked, not absolute. To find the absolute mass fraction for an element, subtract the value of the element plotted just below it. By comparing the concentrations of the radioisotopes in panel (b) to the stable products in panel (a), we can estimate the dust molecules into which the radioisotopes are most likely to condense.

This will begin ∼1–5 yr after the SN. The radioisotopes will chemically bond with the surrounding elements forming molecules first, then combining to form larger and larger grains. We assume our primary radioisotopes (^{60}Fe, ^{26}Al, ^{53}Mn, ^{41}Ca) will form compounds like their stable isotopes. In the case of ^{60}Fe, the bulk of which forms in a primarily Fe-Ni region (see Figure 1), we assume it will condense and form into metallic Fe grains rather than silicates, oxides, or sulfides since the associated elements are not present in that region of the ejecta. Conversely, ^{26}Al, which is created in an O-rich region, will likely form into AlO and Al_2O_3 molecules, and some of the ^{53}Mn will likely form MnS since it is created in an S-rich region (Field 1975). Although mixing due to Rayleigh–Taylor instabilities is present, this mixing is macroscopic not microscopic, meaning the composition choice of our grains will not be affected. This is supported observationally by examinations of Cassiopeia A (Douvion et al. 1999) and discussed in detail in Cherchneff & Dwek (2010) and Cherchneff & Sarangi (2011). Knowing the type of compound the radioisotope resides in

is important since different compounds have different densities, are more/less resistant to erosion, and absorb/emit electrons and photons differently.

The grains will continue to grow until the elemental products run out, the density drops too low, or the RS arrives. Up to this point, the ejecta gas, overdense clouds, and the dust grains within have been traveling together with negligible relative velocities. The RS will then slow and heat the gas and send a shock wave through the cloud, crushing it and shattering some of the dust grains. Several studies have examined this process (Silvia et al. 2010, 2012; Biscaro & Cherchneff 2016), and our examination of the dust grains will begin just after this processing. The cloud containing the dust grains will dissipate, and the dust grains will be exposed to the hot SNR plasma. Because of their high mass compared to the surrounding gas, the dust grains will have decoupled from the plasma and will be moving with a large velocity relative to the plasma. A number of influences will now act on the dust grain (see Dwek & Arendt 1992, and references therein), and we will now examine the most important processes in greater detail. We assume the grains to be spherical in shape with radius, $a_{\rm gr}$, and uniform in composition.

To track the trajectory of a dust grain within the SNR, we solve a system of seven ordinary differential equations:

$$\begin{aligned}\frac{d\boldsymbol{r}_{\rm gr}}{dt} &= \boldsymbol{v}_{\rm gr}\\ \frac{d\boldsymbol{p}_{\rm gr}}{dt} &= \textstyle\sum_i \boldsymbol{F}_i(a_{\rm gr}, q_{\rm gr}, \rho, T, ...)\\ \frac{da_{\rm gr}}{dt} &= \textstyle\sum_i \mathcal{N}_i(a_{\rm gr}, q_{\rm gr}, \rho, T, ...)\end{aligned} \quad (1)$$

where the summed processes, i, are dependent on the grain properties (size, charge, etc.) and the SNR environment (density, temperature, etc.). In addition, we solve for the grain charge analytically:

$$q_{\rm gr} = q_{\rm gr}(a_{\rm gr}, v_{\rm gr}, \rho, T, ...). \quad (2)$$

Our specific initial grain conditions will be given in Section 5, but, in qualitative terms, we follow our dust grains from time t_0, which corresponds to the time the RS passes the location of the grain. While we expect dust grains to reside within overdense clouds, we assumed our dust grains to be at the leading edge of the cloud at the arrival of the RS. The dust grains are immediately exposed to the hot, SNR environment rather than being relatively protected until the cloud dissipates.[7] This represents the worst case scenario for dust grain survival. The initial velocity, v_0, is determined by the velocity of the surrounding gas at the time of condensation. We assume that dust condensation took place over 100–1000 days after the explosion (Sarangi & Cherchneff 2015; Cherchneff & Sarangi 2017; Sluder et al. 2018).[8] The initial position of the grain, r_0, is the location of the grain at the time the RS passes, and the initial grain size, a_0, will be the post-RS/post-shattering size (in case the RS caused any grain shattering). Since we do not model grain growth, we examine a range of sizes. Also, we do not include grain–grain interactions (e.g., impacts and charge influences; Bocchio et al. 2016 found that collisions were rare, with a collisional timescale of 8×10^5 yr, roughly the length of our simulation timescale) or grain heating (Bianchi & Schneider 2007; Nozawa et al. 2007; Bocchio et al. 2016 found grain sublimation to be negligible). Lastly, the initial charge will effectively be zero, $q_0 = 0$, since the grains are formed in a cool, dense cloud, and they will quickly charge/discharge to equilibrium (see Section 3.3).

3.1. Grain Dynamics

3.1.1. Drag Force

Because the dust grains have a relative velocity compared to the surrounding plasma, they will experience drag. Drag will be due to collisions with plasma particles, and since the plasma is ionized and the grains charged (see Section 3.3), Coulomb drag (also called plasma drag) may also be relevant. The combined drag of both sources is given by Draine & Salpeter (1979) and Draine (2011) as

$$\begin{aligned}F_{\rm drag} &= 2\pi a_{\rm gr}^2 k_{\rm B} T\\ &\times \left\{\textstyle\sum_j n_j [G_0(s_j) + Z_j^2 \Phi^2 \ln[\Lambda/Z_j] G_2(s_j)]\right\}\end{aligned} \quad (3)$$

(see Appendix G for descriptions of the variables).

3.1.2. Motion of a Charged Dust Grain in a Magnetic Field

Because there will be magnetic fields present within the SNR and the grain will be charged, we include the Lorentz force on the grain:

$$\boldsymbol{F}_{\rm mag} = \frac{q_{\rm gr}}{c}\boldsymbol{v}_{\rm rel} \times \boldsymbol{B}. \quad (4)$$

Because of flux freezing, the magnetic field, $\boldsymbol{B}$, will be moving with the plasma, so we use the grain's velocity relative to the plasma, $\boldsymbol{v}_{\rm rel} = \boldsymbol{v}_{\rm gr} - \boldsymbol{v}_{\rm plasma}$.

Under the influence of the Lorentz force, charged dust grains in a magnetic field will spiral around magnetic field lines (Northrop & Morfill 1984). The radius of this spiraling, $R_{\rm gyro}$, is given by Murray et al. (2004):

$$\begin{aligned}R_{\rm gyro} = 9.75 \times 10^{-4}\ {\rm pc} &\left(\frac{\rho_{\rm gr}}{7.87\ {\rm g\ cm^{-3}}}\right)\left(\frac{172.5\ {\rm V}}{|U_{\rm gr}|}\right)\\ \times &\left(\frac{1\ \mu{\rm G}}{B}\right)\left(\frac{v_{\perp,{\rm gr}}}{175\ {\rm km\ s^{-1}}}\right)\left(\frac{a_{\rm gr}}{0.1\ \mu{\rm m}}\right)^2,\end{aligned} \quad (5)$$

where $\boldsymbol{B}$ is the magnetic field, $\rho_{\rm gr}$ is the mass density, $\boldsymbol{v}_{\perp,{\rm gr}}$ is the velocity perpendicular to the magnetic field, $a_{\rm gr}$ is the radius, and $U_{\rm gr}$ is the potential of the grain. Additionally, the

[7] It is expected that the cloud dissipates in approximately three cloud crushing times, $\sim 3\tau_{\rm cc}$ where $\tau_{\rm cc} = (\rho_{\rm cloud}/\rho_{\rm ICM})^{1/2}\ (a_{\rm cloud}/v_{\rm RS})$ (Klein et al. 1994). Typically, the ratio of the cloud to the intercloud medium (ICM) densities is $(\rho_{\rm cloud}/\rho_{\rm ICM}) \sim 100$–$1000$ with a cloud size of $a_{\rm cloud} = 10^{16}$ cm (Silvia et al. 2010, 2012). In our simulation, the speed of the RS is $\sim$175 km s^{-1}, giving a cloud dissipation time of $3\tau_{\rm cc} \sim 540$–1700 yr. The dust grain would largely retain its initial velocity through the passage of the RS until the cloud has dissipated.

[8] Because of free expansion and the fact that we are not modeling grain growth, our results are not sensitive to the condensation time.

period of this spiraling can be determined,

$$\tau_{\rm gyro} = 34\ {\rm yr}\left(\frac{\rho_{\rm gr}}{7.87\ {\rm g\ cm^{-3}}}\right)\left(\frac{172.5\ {\rm V}}{|U_{\rm gr}|}\right) \times \left(\frac{1\ \mu{\rm G}}{B}\right)\left(\frac{a_{\rm gr}}{0.1\ \mu{\rm m}}\right)^2. \quad (6)$$

In the case of a magnetic field with varying magnitude, the spiraling dust grain will conserve adiabatic quantities (see, e.g., Section 12.5, Jackson 1998). Of particular interest for our examination is the adiabatic invariant $p_{\perp,{\rm gr}}^2/B$, where $p_{\perp,{\rm gr}}$ is the momentum of the grain perpendicular to the magnetic field and the parallel component $v_\parallel = \sqrt{v^2 - v_\perp^2}$, where v is the total velocity. Since magnetic fields do not perform work on the grain, we know the speed of the grain at later times will be the same as when it entered the field, $v = v_{\rm ini}$. If the magnetic field increases with position, $B(r)$, then by the adiabatic invariance, we have

$$\frac{v_\perp^2}{B(r)} = \frac{v_{\perp,{\rm ini}}^2}{B_{\rm ini}},$$
$$\Rightarrow v_\parallel^2 = v_{\rm ini}^2 - v_{\perp,{\rm ini}}^2\frac{B(r)}{B_{\rm ini}}. \quad (7)$$

As the magnetic field increases, $v_\perp$ will increase, which means $v_\parallel$ will decrease in order to maintain the original speed of the grain. There will be a position, $R_{\rm bounce}$, where the right side of Equation (7) vanishes, and the grain's movement along the magnetic field lines will reverse direction. Essentially, the grain will "bounce" off the stronger magnetic field. This is referred to as a magnetic mirror in Jackson (1998) and leads to the "pinball" behavior we discuss in Sections 5–7.

We can find an expression for the strength of the magnetic field able to bounce a dust grain assuming $\tau_{\rm gyro} \ll \tau_{\rm sputtering}$ (see Equation (13)). At bounce, $B_{\rm bounce} \equiv B(R_{\rm bounce})$,

$$v_{\rm ini}^2 = v_{\perp,{\rm ini}}^2\frac{B_{\rm bounce}}{B_{\rm ini}}, \quad (8)$$

and if we consider an average case ($v_\perp \sim v_\parallel$),

$$\langle v_{\perp,{\rm ini}}\rangle \sim \frac{1}{\sqrt{2}}v_{\rm ini}, \quad (9)$$

then the magnetic field at bounce is

$$v_{\rm ini}^2 \approx \frac{1}{2}v_{\rm ini}^2\frac{B_{\rm bounce}}{B_{\rm ini}} \quad (10)$$
$$\Rightarrow B_{\rm bounce} \approx 2B_{\rm ini}. \quad (11)$$

If the magnetic field varies with some characteristic length scale, $\lambda_{\rm mag}$, then when $R_{\rm gyro} \lesssim \lambda_{\rm mag}$, the grain will be "captured" by the magnetic field (i.e., the grain spirals around the magnetic field lines). After capture, if the magnetic field strength doubles, the dust grain will be reflected. We will see this effect is relevant when considering dust grains encountering shocked ISM material within an SNR.

3.2. Grain Sputtering

In addition to drag from the grains' high velocity relative to the plasma, the grains will also be eroded/sputtered by impacts with plasma particles. In addition to kinetic sputtering from bulk motion of plasma onto the grains, at high temperatures, the thermal velocities of plasma particles will also erode the grains. Because of high relative velocities and high temperatures within the SNR, we include both kinetic and thermal sputtering. The erosion rate due to sputtering (both kinetic and thermal) is given by Dwek & Arendt (1992), and we use the approach by Nozawa et al. (2006) and Biscaro & Cherchneff (2016), namely,

$$\frac{da_{\rm gr}}{dt} = -\frac{m_{\rm sp}}{4\rho_{\rm gr}}\sum_j \frac{n_j}{s_j}\left(\frac{8k_{\rm B}T}{\pi m_j}\right)^{1/2}\exp\left[-s_j^2\right] \times \int d\epsilon_j\sqrt{\epsilon_j}\exp\left[-\epsilon_j\right]\sinh\left(2s_j\sqrt{\epsilon_j}\right)Y_j^0(\epsilon_j) \quad (12)$$

(see Appendix H for descriptions of the variables).

For our grain parameters, the sputtering time for dust grains is (Draine 2011)

$$\tau_{\rm sputtering} = 10^6\ {\rm yr}\left[1 + \left(\frac{10^6\ {\rm K}}{T}\right)^3\right]\left(\frac{a_{\rm gr}}{0.1\ \mu{\rm m}}\right) \times \left(\frac{0.1\ {\rm cm^{-1}}}{n_{\rm ISM}}\right). \quad (13)$$

3.3. Grain Charging

As grains move within the SNR, they will acquire/lose electrons and ions due to impacts with the plasma and photons. Several processes can influence the total charge of the grain, so the total charging rate, $dq_{\rm gr}/dt$, is

$$\frac{dq_{\rm gr}}{dt} = \sum_j \mathcal{I}_j, \quad (14)$$

which is summed over j processes of currents, $\mathcal{I}_j$. These currents are due to impinging plasma particles, $\mathcal{I}_{\rm imp}$, and the associated secondary electrons emitted, $\mathcal{I}_{\rm see}$, transmitted plasma particles, $\mathcal{I}_{\rm trans}$, and photoelectron emission, $\mathcal{I}_\gamma$. The derivations are the same as used by Kimura & Mann (1998). However, these derivations are very computationally intensive (see Appendix E for an in-depth discussion). In order simplify calculations, we employ an analytic description of the charging processes.

If we compare the gyro period given in Equation (6) with a basic approximation for the charging time from accumulating/dispersing electrons/ions (Shukla & Mamun 2002),

$$\tau_{{\rm charge},e/i} = 0.06\ {\rm yr}\sqrt{\frac{T}{10^6\ {\rm K}}}\left(\frac{0.1\ {\rm cm^{-3}}}{n_{\rm ISM}}\right)\left(\frac{0.1\ \mu{\rm m}}{a_{\rm gr}}\right) \times \left(\frac{1}{1 + \sqrt{\frac{m_p}{m_e}}\exp\left[-\left(\frac{\Phi}{2}\right)\right]}\right), \quad (15)$$

we can see that the charging time is much less than the gyro period ($\tau_{{\rm charge},e} \ll \tau_{\rm gyro}$), allowing us to use an analytic approximation of the grain charge when solving for the grain's gyroscopic motions (this means that we do not solve for $dq_{\rm gr}/dt$ in our system of ordinary differential equations). In order to employ a faster description of grain charging processes, we apply an analytic approach introduced by

Shull (1978) and extended by McKee et al. (1987); in this approach, we solve numerically for the steady-state value of the grain potential at various plasma temperatures (T), relative velocities ($v_{\rm rel}$), and grain radii ($a_{\rm gr}$), then fit a function to the results. It should be noted that this approach inherently ignores the cooling/heating history of the grains, and the grain potential will be single-valued at a given temperature (for more information, see Meyer-Vernet 1982; Horanyi & Goertz 1990). However, because of Fe's low secondary electron emission yield ($\delta_{\rm max,Fe} = 1.3 < 6$), our Fe grains should have single-valued potentials across all temperature values.[9]

For a more detailed description of our analytic approximation, see Appendix F.

4. SNR Model Description

We need to model the SNR density, ρ, velocity, $\boldsymbol{v}$, pressure, P, temperature, T, and magnetic field, $\boldsymbol{B}$, and use the magnetohydrodynamics (MHD) equations as the framework. Since we are dealing with an SN explosion, the relative thermal velocities between particles will be small compared to the bulk velocity (meaning thermal conduction can be ignored), the plasma is collisionless (meaning resistivity and ohmic heating due to electron–ion collisions can be ignored), and the ejecta velocity is radial and much greater than the escape velocity ($v_{\rm ej} \gg v_{\rm esc}$) for the central compact object (meaning Coriolis and gravitational effects can be ignored). Additionally, if we limit our examination to the early phases of the SNR expansion (the free expansion and Sedov–Taylor phases), we can ignore radiative effects. Thus, we use the ideal MHD equations (in Lagrangian form and cgs/esu units):

$$\frac{D\rho}{Dt} = -\rho \boldsymbol{\nabla}\cdot\boldsymbol{v} \qquad \text{(Mass)}, \tag{16}$$

$$\frac{D\boldsymbol{v}}{Dt} = -\frac{1}{\rho}\boldsymbol{\nabla}P + \frac{\boldsymbol{J}}{\rho c}\times\boldsymbol{B} \qquad \text{(Momentum)}, \tag{17}$$

$$\frac{DP}{Dt} = -\Gamma P \boldsymbol{\nabla}\cdot\boldsymbol{v} \qquad \text{(Energy)}, \tag{18}$$

$$\frac{D\boldsymbol{B}}{Dt} = (\boldsymbol{B}\cdot\boldsymbol{\nabla})\boldsymbol{v} - \boldsymbol{B}(\boldsymbol{\nabla}\cdot\boldsymbol{v}) \qquad \text{(Induction)}, \tag{19}$$

where $\frac{D}{Dt} \equiv \frac{\partial}{\partial t} + \boldsymbol{v}\cdot\boldsymbol{\nabla}$, $\boldsymbol{J} = \frac{c}{4\pi}\boldsymbol{\nabla}\times\boldsymbol{B}$, and $\Gamma = 5/3$ for the medium we study. Additionally, we assume a polytropic, Newtonian fluid with $P = (\Gamma - 1)\mathbb{E}$ where $\mathbb{E}$ is the energy density. Expanding the momentum equation (Equation (17)), we find that

$$\frac{D\boldsymbol{v}}{Dt} = -\frac{1}{\rho}\boldsymbol{\nabla}P + \frac{1}{\rho c}\left(\frac{c}{4\pi}\right)(\boldsymbol{\nabla}\times\boldsymbol{B})\times\boldsymbol{B} \tag{20}$$

$$= -\frac{1}{\rho}\boldsymbol{\nabla}P + \frac{1}{4\pi\rho}\left((\boldsymbol{B}\cdot\boldsymbol{\nabla})\boldsymbol{B} - \frac{1}{2}\boldsymbol{\nabla}B^2\right). \tag{21}$$

The first term in the parentheses, $(\boldsymbol{B}\cdot\boldsymbol{\nabla})\boldsymbol{B}$, represents the magnetic tension ($\sim B^2/4\pi$, Galtier 2016)[10], and the second term, $\frac{1}{2}\boldsymbol{\nabla}B^2$, represents magnetic pressure $\sim B^2/8\pi$. In a typical SNR during the free expansion and Sedov–Taylor phases, expanding at $\sim$200 km s^{-1} with a peak density of $4m_H$ cm^{-3}, the ram pressure is $P_{\rm ram} = \rho v^2 \sim 10^{-9}$ dyne cm^{-2}. In contrast, for a typical ISM magnetic field ($B_{\rm ISM} \sim 1\ \mu$G), the magnetic tension and pressure are much weaker, $P_{\rm mag} \sim 10^{-13}$ dyne cm^{-2} (see Section 4.4). Because of this, they can be ignored, and Equations (16)–(18) simplify to

$$\text{Basic Fluid Equations}\begin{cases} \dfrac{D\rho}{Dt} &= -\rho\boldsymbol{\nabla}\cdot\boldsymbol{v}, \\ \dfrac{D\boldsymbol{v}}{Dt} &= -\dfrac{1}{\rho}\boldsymbol{\nabla}P, \\ \dfrac{DP}{Dt} &= -\Gamma P\boldsymbol{\nabla}\cdot\boldsymbol{v}. \end{cases} \tag{22}$$

These are the basic fluid equations we use, where we see that during the early stages of SNR evolution, the expansion can be determined without including the magnetic field influence.

4.1. Nucleosynthesis Products

Fry et al. (2015) found that an ECSN was the most likely source for the ^{60}Fe signal. This determination was based on the nucleosynthesis results in Wanajo et al. (2009, 2013a, 2013b), so we use the results of these nucleosynthesis simulations for several aspects of our model. First, the results of the nucleosynthesis simulations are the initial conditions for our hydrodynamics simulations. The nucleosynthesis results also describe the composition of the ejecta, allowing us to determine the types and concentrations of elements interacting with the grains as they transit the SNR. Lastly, the nucleosynthesis results give the initial positions of the radioisotopes within the ejecta. This allows us to determine the initial velocities and types of grains that will mostly likely be formed containing specific radioisotopes (Sarangi & Cherchneff 2013, 2015; Biscaro & Cherchneff 2014; Sluder et al. 2018). The major nucleosynthesis products and radioisotopes are shown with their initial positions in Figure 1.

We have assumed for definiteness an ECSN progenitor with a ZAMS mass of 8.8 $M_\odot$, leaving a 1.363 $M_\odot$ neutron star, and ejecting a 0.014 $M_\odot$ inner core that contains the SN synthesized products and a 1.249 $M_\odot$ outer envelope composed of 70% Hydrogen and 30% Helium (we assume large-scale convection that thoroughly mixes the envelope) giving a total ejecta mass of $M_{\rm ej} = 1.263\ M_\odot$. This is similar to the treatments by Janka et al. (2008) and Hoffman et al. (2008). The envelope is assumed to be in hydrostatic equilibrium and a single isothermal sphere with a temperature of 3500 K and completely ionized ($\mu_{\rm envel} = 0.61$) (for more detail, see Section 4.2). The energy delivered as kinetic energy into the ejecta is $E_{\rm SN} = 1.5 \times 10^{50}$ erg (Wanajo et al. 2009).

4.2. Hydrodynamic Initial Conditions

The density, velocity, and pressure profiles are based on the Wanajo et al. (2013a) nucleosynthesis results, the expected configuration of an ECSN progenitor, and the properties of the Local Bubble at the time of the SN. The ejecta is divided into an inner core region and an outer shell region based on the Wanajo et al. (2013a) results. The two-dimensional Wanajo et al. (2013a) results contained values at different azimuths and radii, so we averaged the values across azimuths, and fit a power-law profile to the density and velocity averages. A comparison of the averaged results and fits is shown in

[9] From Horanyi & Goertz (1990), the presence of multivalued potentials occurs for substances with $\delta_{\rm max} \gtrsim 6$.

[10] This term is sometimes referred to as "magnetic stress" (see, e.g., Davidson 2001).

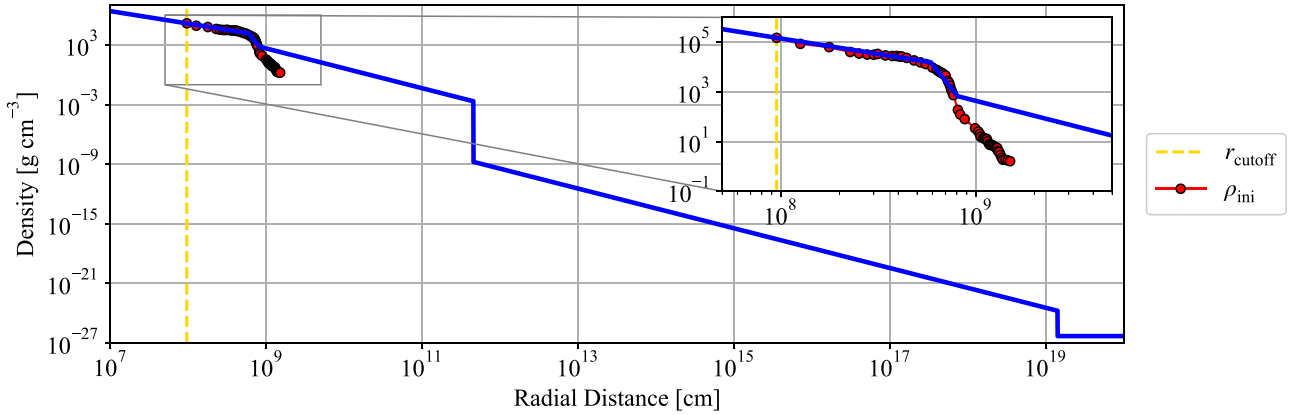

(a)

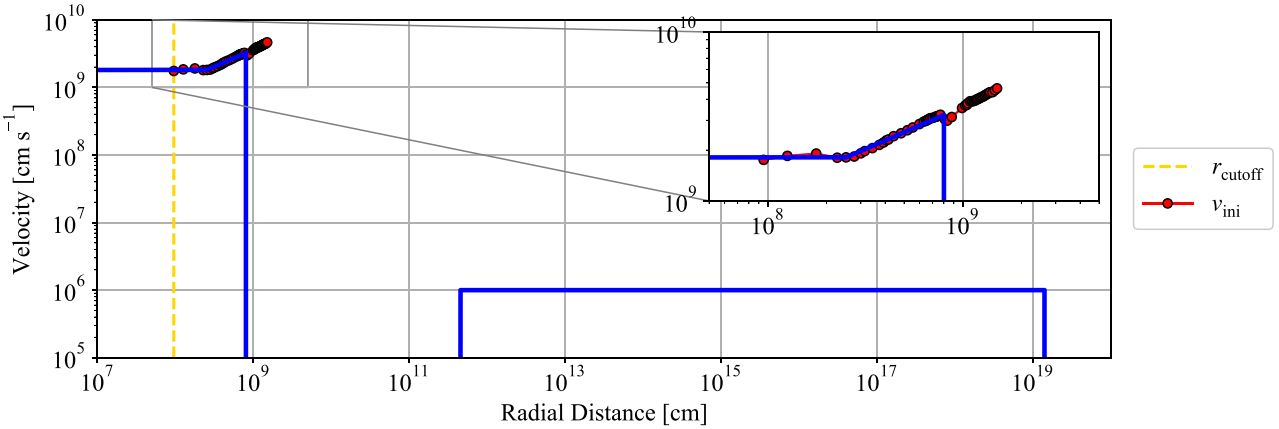

(b)

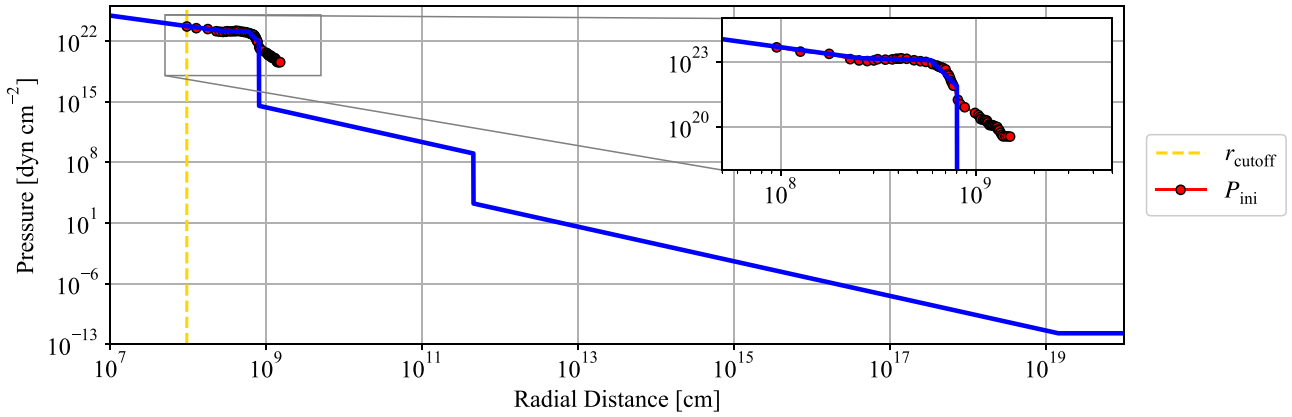

(c)

Figure 2. Initial density, velocity, and pressure profiles. Our initial profiles are shown in blue with the azimuthally averaged Wanajo et al. (2013a) ECSN results plotted in red. Because our model includes an outer envelope (similar to Janka et al. 2008), the envelope profile contains some of the nucleosynthesis products. The composition of the envelope was adjusted to include the nucleosynthesis products' mass, but these products were given the initial density, velocity, and pressure of the envelope.

Figures 2(a) and (b); note that the core cutoff positions for density and velocity ($r_{\rm core,1}$ and $r_{\rm core,2}$, respectively) are slightly different in order to provide a better fit.

The progenitor of an ECSN is assumed to be a super-AGB star (Smartt et al. 2009; Woosley & Heger 2015) with an envelope that has been completely mixed due to its thermal-pulsing (TP-SAGB) phase (Herwig 2005; Poelarends et al. 2008; Pumo et al. 2009; Pumo 2010; Jones et al. 2016). This implies that the progenitor will be a red supergiant and have an extended, isothermal envelope. We chose an envelope temperature of 3500 K (the approximate surface temperature of Betelgeuse; Freytag et al. 2002) with $\rho \propto r^{-2}$ and $v = 0$. The edge of the envelope, $r_{\rm envel}$ marks the edge of the progenitor, and we assume the presence of a pre-SN wind. Several studies have

examined the wind and mass loss during the TP-SAGB phase (see, e.g., Doherty et al. 2014, and references therein), and we assumed a mass loss of $\dot{M}_{\rm wind} = 7 \times 10^{-5}\,M_{\odot}\ {\rm yr}^{-1}$ and a wind velocity of $v_{\rm wind} = 10\,{\rm km\,s}^{-1}$.

The pre-SN stellar wind will extend until the ram pressure of the wind, $P_{\rm wind} = \rho v_{\rm wind}^2$, equals the pressure of the ISM, $P_{\rm ISM}$ (Castor et al. 1975). Because the Local Bubble shows evidence of multiple SNe (e.g., Breitschwerdt et al. 2016, and references therein), we assume the source of the ^{60}Fe signal to be the most recent SN and that this SN would have occurred in a region similar to that currently observed in the Local Bubble. Thus, we assumed ISM values of $n_{\rm ISM} = 0.005\,{\rm cm}^{-3}$, $\mu_{\rm ISM} = 0.61$, $P_{\rm ISM} = 1.8 \times 10^{-12}\,{\rm dyn\,cm}^{-2}$ (Fields et al. 2008), and $T_{\rm ISM} = 2.6 \times 10^{6}\,{\rm K}$.

Combining these parameters, we assume the following initial conditions for our hydrodynamic simulations:

$$\rho(r) = \begin{cases} \rho_{\rm core}(r) & r_{\rm cutoff} \leqslant r < r_{\rm core,2}, \\ \rho_{\rm shell}(r) & r_{\rm core,2} \leqslant r < r_{\rm shell}, \\ \rho_{\rm envel}(r) & r_{\rm shell} \leqslant r < r_{\rm envel}, \\ \rho_{\rm wind}(r) & r_{\rm envel} \leqslant r < r_{\rm wind}, \\ \rho_{\rm ISM} & r_{\rm wind} \leqslant r; \end{cases} \tag{23}$$

where

$$\begin{aligned} \rho_{\rm core}(r) &= 1.51 \times 10^{5}\ {\rm g\,cm}^{-3} \left(\frac{r}{9.52 \times 10^{7}\ {\rm cm}}\right)^{-5/4}, \\ \rho_{\rm shell}(r) &= 1.75\ {\rm g\,cm}^{-3} \left(\frac{r}{1.46 \times 10^{9}\ {\rm cm}}\right)^{-10}, \\ \rho_{\rm envel}(r) &= 743.67\ {\rm g\,cm}^{-3} \left(\frac{r}{7.68 \times 10^{8}\ {\rm cm}}\right)^{-2}, \\ \rho_{\rm wind}(r) &= \frac{\dot{M}_{\rm wind}}{4\pi v_{\rm wind} r^2}, \\ \rho_{\rm ISM} &= \mu_{\rm ISM} m_H n_{\rm ISM}; \end{aligned} \tag{24}$$

and

$$\begin{aligned} r_{\rm cutoff} &= 9.52 \times 10^{7}\ {\rm cm} \\ r_{\rm core,2} &= 5.88 \times 10^{8}\ {\rm cm} \\ r_{\rm shell} &= 8.01 \times 10^{8}\ {\rm cm} \\ r_{\rm envel} &= 4.51 \times 10^{11}\ {\rm cm} \\ r_{\rm wind} &= 1.40 \times 10^{19}\ {\rm cm}; \end{aligned} \tag{25}$$

$$v(r) = \begin{cases} v_{\rm core}(r) & r_{\rm cutoff} \leqslant r < r_{\rm core,1}, \\ v_{\rm shell}(r) & r_{\rm core,1} \leqslant r < r_{\rm shell}, \\ v_{\rm envel}(r) & r_{\rm shell} \leqslant r < r_{\rm envel}, \\ v_{\rm wind} & r_{\rm envel} \leqslant r < r_{\rm wind}, \\ v_{\rm ISM} & r_{\rm wind} \leqslant r; \end{cases} \tag{26}$$

where

$$\begin{aligned} v_{\rm core}(r) &= 1.81 \times 10^{9}\ {\rm cm\,s}^{-1}, \\ v_{\rm shell}(r) &= 1.81 \times 10^{9}\ {\rm cm\,s}^{-1} \left(\frac{r}{r_{\rm core,1}}\right)^{1/2}, \\ v_{\rm envel}(r) &= 0\ {\rm cm\,s}^{-1}, \\ v_{\rm wind}(r) &= 10\ {\rm km\,s}^{-1}, \\ v_{\rm ISM} &= 0\ {\rm cm\,s}^{-1}; \end{aligned} \tag{27}$$

and $r_{\rm core,1} = 2.52 \times 10^{8}\,{\rm cm}$;

$$P(r) = \begin{cases} P_{\rm core}(r) & r_{\rm cutoff} \leqslant r < r_{\rm core,2}, \\ P_{\rm shell}(r) & r_{\rm core,2} \leqslant r < r_{\rm shell}, \\ P_{\rm envel}(r) & r_{\rm shell} \leqslant r < r_{\rm envel}, \\ P_{\rm wind}(r) & r_{\rm envel} \leqslant r < r_{\rm wind}, \\ P_{\rm ISM} & r_{\rm wind} \leqslant r; \end{cases} \tag{28}$$

$$\begin{aligned} P_{\rm core}(r) &= \rho(r) v(r)^2, \\ P_{\rm shell}(r) &= \rho(r) v(r)^2, \\ P_{\rm envel}(r) &= \frac{\rho(r) k_{\rm B} T_{\rm envel}}{\mu_{\rm envel} m_H}, \\ P_{\rm wind}(r) &= \rho(r) v(r)^2, \\ P_{\rm ISM} &= P_{\rm ISM}. \end{aligned} \tag{29}$$

4.3. Hydrodynamic Simulations

Our hydrodynamic simulations use the RT1D code written by Duffell (2016). This is a 1D+, adaptive, moving mesh code that includes Rayleigh–Taylor instabilities in SNe. Although the code is one-dimensional, it includes the multidimensional effects of Rayleigh–Taylor instabilities as source terms in the fluid equations, chosen to represent turbulent perturbations averaged over a solid angle. This enables simulations of non-radiative SNR expansion based on the basic fluid equations, which run from the free expansion through the Sedov–Taylor phases. As noted by Duffell, the incorporation of Rayleigh–Taylor instabilities eliminates the singularities inherent in the Chevalier–Nadezhin solutions and provides a more accurate position of the RS than that found by Truelove & McKee (1999). The simulations are run in characteristic units; these are dimensionless units of the hydrodynamic quantities (i.e., in characteristic units, density is given by $\rho^{*} = \rho/\rho_{\rm ch}$, where $\rho_{\rm ch}$ is the characteristic density for the SN environment). The characteristic values' definitions and our adopted values are

$$\begin{aligned} r_{\rm ch} &\equiv \left(\frac{M_{\rm ej}}{\rho_{\rm ISM}}\right)^{1/3} = 25.6\ {\rm pc}, \\ t_{\rm ch} &\equiv \frac{M_{\rm ej}^{5/6}}{\rho_{\rm ISM}^{1/3} E_{\rm SN}^{1/2}} = 10,200\ {\rm yr}, \\ M_{\rm ch} &\equiv M_{\rm ej} = 1.263\,M_{\odot}, \\ \rho_{\rm ch} &\equiv \rho_{\rm ISM} = 0.00305 m_p\ {\rm cm}^{-3}, \\ v_{\rm ch} &\equiv \frac{r_{\rm ch}}{t_{\rm ch}} = 2440\ {\rm km\,s}^{-1}, \\ P_{\rm ch} &\equiv \rho_{\rm ch} v_{\rm ch}^2 = 3.05 \times 10^{-10}\ {\rm dyn\,cm}^{-2}, \\ T_{\rm ch} &\equiv \frac{\mu_{\rm ej} m_{\rm u} P_{\rm ch}}{k_{\rm B} \rho_{\rm ch}} \\ &= \frac{\mu_{\rm ej} m_{\rm u}}{k_{\rm B}} v_{\rm ch}^2 = 4.41 \times 10^{8}\ {\rm K}. \end{aligned} \tag{30}$$

These definitions are based on Truelove & McKee (1999) and assume a uniform ambient medium (for power-law, i.e., stellar wind, mediums, see also Truelove & McKee 1999;

Laming & Hwang 2003; Haid et al. 2016).[11] Since we are examining the SNR expansion both inside and outside the pre-SN stellar wind, we applied the uniform case since the forward shock is in a uniform medium for the vast majority of our simulation duration. As noted in Section 4.2, our choices for E_{SN} and M_{ej} correspond to our adopted ECSN model.

The hydrodynamics simulations were begun at $t = 300$ ms ($t^* = 9.285 \times 10^{-13}$) after the core bounce, which corresponds to the end of the Wanajo et al. (2013a) results, and run through $t = 512$ kyr ($t^* = 50$). This encompasses the entire free expansion and Sedov–Taylor phases. The position values began at the cutoff radial position, $r_{cutoff} = 9.52 \times 10^7$ cm ($r^*_{cutoff} = 1.206 \times 10^{-12}$), extended through the outermost radial position, $R = 25{,}600$ pc ($R^* = 1000$), and were initially divided into 1024 zones. In the simulation run, results were generated at 1000 logarithmically spaced time intervals. Each output includes the radial position of the zone's midpoint, zone radial width, density, velocity, pressure, mixture fraction (the fraction of the zone comprised of ejecta material), and the turbulent factor (which was a measure of the Rayleigh–Taylor fluctuations; for our purposes, this was not used). Because many of the results had nearly power-law profiles, 2D linear spline interpolation functions were generated for the common logarithms of the SNR quantities (i.e., $\log \rho^*$, $\log |v^*|$, etc.) done across $\log t^* \times \log r^*$. The temperature interpolation was done with $\log T^* = \log(P^*/\rho^*)$.

Additionally, with the assumption of spherical symmetry, the mass enclosed, $M_{enclosed}$, by a sphere at a given radial position, r, is described by

$$M_{enclosed} = \int_{r_{min}}^{r} 4\pi\rho(r')r'^2 dr', \tag{31}$$

where r_{min} is the innermost zone position in the RT1D simulation. Given the enclosed mass, the average elemental composition of SNR can be determined at any point. With the interpolation functions, we have the means to determine the density, velocity, temperature, and composition at all locations within the SNR.

The RT1D code allows simulations to be run with or without Rayleigh–Taylor instabilities included. Using the initial conditions defined in Section 4.2, without Rayleigh–Taylor instabilities, our dust grains encounter the RS after ~8600 yr, but with Rayleigh–Taylor instabilities, our dust grains encounter the RS much sooner, at ~5000 yr.

4.4. Magnetic Field

In our simulation, we split the magnetic field into three regions: the star/ejecta field, the stellar wind field, and the ISM field. In the star/ejecta region, we expect a surface field $B \sim 1$ G (this is the average surface field for Betelgeuse, which is similar in mass to our expected progenitor; Petit et al. 2013). In addition, massive stars generally seem to exhibit weak surface magnetic fields ($B \lesssim 1$ G, Augustson 2019). From magnetic flux conservation (e.g., Padmanabhan 2001), $B \approx B_{ini}(r_{ini}/r)^2$, and if we estimate that the dust will decouple from the plasma at ~1 pc (a *very* rough estimate), then the stellar field will have weakened to: $B \sim 10^{-8}\,\mu$G ($\Rightarrow R_{gyro} \sim 100$ kpc $> \lambda_{Milky\ Way}$, see Section 3.1.2). Furthermore, because the stellar wind magnetic field is the surface field stretched even further due to flux freezing within the pre-SN wind, we expect the stellar wind magnetic field to be weak as well. With this reasoning, we set $B_{star} = B_{wind} = 0$.

For the ISM magnetic field, because we focus our examination within the Local Bubble, the site of multiple SNe, we assume the initial magnetic field to be nonuniform and weakened compared to the average ISM ($\langle |\boldsymbol{B}_{ISM}| \rangle \sim 3.57\ \mu$G and $\sqrt{\langle B^2_{ISM} \rangle} \approx 8.94\ \mu$G; Balsara et al. 2001). Using flux conservation, from Padmanabhan (2001) again, and the fact that $\rho \propto r^{-3}$:

$$\Rightarrow B \approx B_{ini}\left(\frac{\rho}{\rho_{ini}}\right)^{2/3}, \tag{32}$$

so our initial magnetic field will have an average magnitude of $\langle |\boldsymbol{B}_{ini}| \rangle \approx 0.06\ \mu$G and dispersion of $\sqrt{\langle B^2_{ini} \rangle} \approx 0.15\ \mu$G.

As our model SN expands into the ISM, we expect it to encounter an ISM magnetic field that has been twisted by turbulence from the passages of previous SNe ejecta. This assumption is based on evidence that the Local Bubble has experienced multiple SNe, which means the ISM will be ionized. The presence of density perturbations within the ISM and ejecta lead to instabilities that will drive turbulence in the ISM plasma that will, in turn, drag the magnetic field with it. In order to generate a model for the magnetic field encountered by our dust grains, we will build our magnetic field in three parts, as follows:

1. Generate a grid of initial magnetic field values with an energy spectrum appropriate to turbulent media.
2. Interpolate between the grid values in order to describe the initial magnetic field at all points while remaining divergence free.
3. Transform the initial magnetic field to account for the passage of the FS and varying density in order to determine the final magnetic field encountered by our dust grains.

We assume that the turbulence in the ISM is homogeneous and isotropic and is fully developed and stationary (time-translation invariant). In order to generate a vector field with these properties, we use a random realization that generates a 3D grid of values with the desired specific energy spectrum, $\mathcal{E}_k \sim k^\eta$ (for more detail see Appendix B). This grid has discrete values from $k_{outer} = 2\pi/\lambda_{outer}$ to $k_{inner} = 2\pi/\lambda_{inner}$, where λ_{outer} is the outer turbulent scale where energy is injected, and λ_{inner} is the inner turbulent scale where energy is dissipated by viscous forces. For this work, we chose $\lambda_{outer} = 5$ pc (this is within the range of radio polarization variations in several SNRs, i.e., 3–13 pc; Fürst & Reich 2004; Uyaniker et al. 2004; Han et al. 2014; Ma et al. 2016), and due to limitations with high-resolution discrete Fourier transforms, we chose $\lambda_{inner} \lesssim 0.05$ pc. This 256^3 grid is then Fourier transformed from k space to real space, giving a cube of dimensions λ^3_{outer}. In order to minimize memory requirements, this volume is rotated to random orientations and stacked together in order to completely fill in the total simulation volume.[12]

[11] The characteristic temperature, T_{ch}, is more commonly defined as $T_{ch} = \left(\frac{3}{16}\right)\left(\frac{\mu m_p v^2_{ch}}{k_B}\right)$ (McKee & Draine 1991; Truelove & McKee 1999). This is a result of characteristic values defined based on jump conditions: $P_{ch} = \frac{\rho_{ISM} v^2_{ch}}{\Gamma+1} = \frac{\rho_{ch} k_B T_{ch}}{\mu m_p}$, $\rho_{ch} = \left(\frac{\Gamma+1}{\Gamma-1}\right)\rho_{ISM}$ with $\Gamma = 5/3$ (Draine 2011). This description is a more accurate gauge of the SN, but since our use of characteristic units is confined to unit conversions, our conclusions will not be affected by the distinction.

[12] It should be noted that we do not include a description of magnetic field amplification along the FS ($B_{ISM} \sim 1$ mG; Inoue et al. 2009; Xu & Lazarian 2017). As will be seen in Section 5, since our grains do not reach the FS, this should not affect our conclusions.

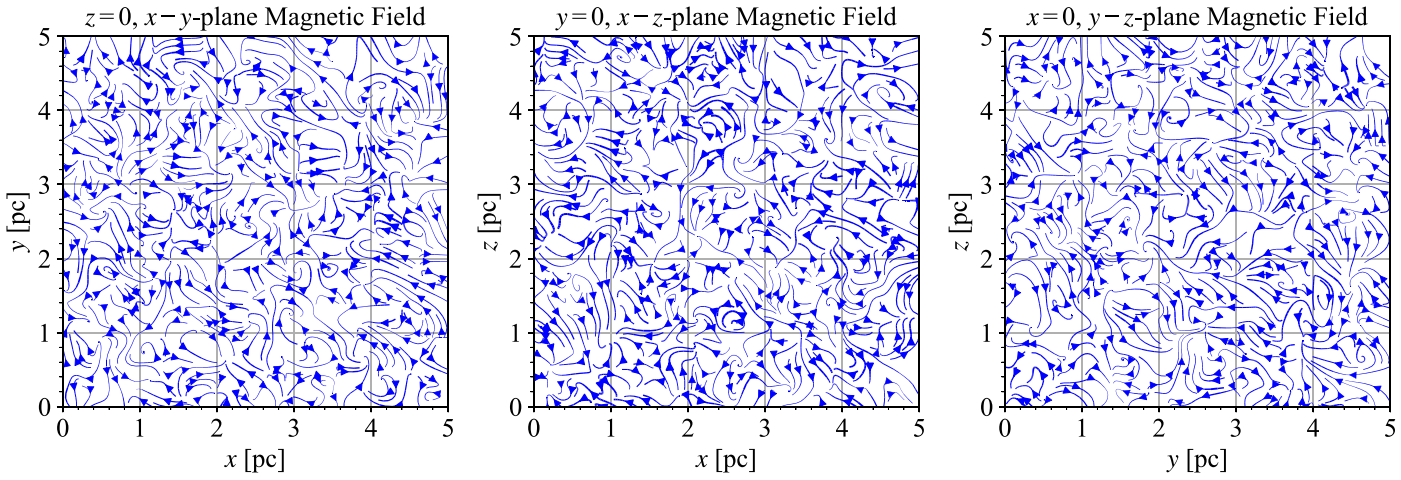

Figure 3. Sample turbulent field. The energy spectrum uses a Kolmogorov profile ($\mathcal{E}_k \sim k^{-5/3}$) with $\mathbb{C} = 1.144 \times 10^{-13}$ G^2 pc$^{17/3}$, $\lambda_{\rm outer} = 5$ pc, and $\lambda_{\rm inner} = 0.05$ pc.

In order to determine the value of the initial magnetic field everywhere and ensure that it has zero divergence, we use a radial basis function to interpolate between the turbulent grid vector values (McNally 2011; see Appendix C). An inherent property of this type of interpolation ensures $\boldsymbol{\nabla} \cdot \boldsymbol{B} = 0$ for our initial magnetic field even if the random grid values alone were not necessarily divergence free (for comparison, an alternate SNR turbulent magnetic field is given by West et al. 2017; see Figure 3).

Although magnetic fields are dynamically unimportant in the early evolution of an SNR, it is still possible to determine the evolution of the magnetic fields in terms of the other fluid quantities (Chevalier 1974) via the flux-freezing assumption. Namely, in order to determine the magnetic field, $\boldsymbol{B}$, we combine Equation (19) with Equation (16), $\frac{D}{Dt}\left(\frac{1}{\rho}\right) = \frac{\nabla \cdot \boldsymbol{v}}{\rho}$, yielding

$$\frac{D\boldsymbol{B}}{Dt} = (\boldsymbol{B} \cdot \boldsymbol{\nabla})\boldsymbol{v} - \boldsymbol{B}\left(\rho \frac{D}{Dt}\left(\frac{1}{\rho}\right)\right)$$

$$\Rightarrow \frac{1}{\rho}\frac{D\boldsymbol{B}}{Dt} + \boldsymbol{B}\frac{D}{Dt}\left(\frac{1}{\rho}\right) = \frac{1}{\rho}(\boldsymbol{B} \cdot \boldsymbol{\nabla})\boldsymbol{v}$$

$$\Rightarrow \frac{D}{Dt}\left(\frac{\boldsymbol{B}}{\rho}\right) = \left(\frac{\boldsymbol{B}}{\rho}\right) \cdot \boldsymbol{\nabla}\boldsymbol{v}. \quad (33)$$

When compared to the flux conservation Lagrangian derivative, $\frac{D}{Dt}(d\boldsymbol{l}) = d\boldsymbol{l} \cdot \boldsymbol{\nabla}\boldsymbol{v}$, this means that the magnetic flux is "frozen in" the fluid. Because Equation (33) relates the evolution of the magnetic field to the evolution of only the density (which can be determined using the fluid equations), we can solve for the evolution of the magnetic field using that of the density.

For an infinitesimally small fluid element, the magnetic field will be uniform through the entire fluid element, and we can decompose the vector $\boldsymbol{B}$ into a component parallel to the direction of expansion, $\boldsymbol{B}_\parallel$, and a component orthogonal to the direction of expansion, $\boldsymbol{B}_\perp$:

$$\boldsymbol{B}_\parallel \equiv (\boldsymbol{B} \cdot \hat{\boldsymbol{r}})\hat{\boldsymbol{r}}, \quad \boldsymbol{B}_\perp \equiv \boldsymbol{B} - (\boldsymbol{B} \cdot \hat{\boldsymbol{r}})\hat{\boldsymbol{r}}, \quad (34)$$

$$\boldsymbol{B} = \boldsymbol{B}_\perp + \boldsymbol{B}_\parallel, \quad B^2 = B_\perp^2 + B_\parallel^2, \quad (35)$$

where $\hat{\boldsymbol{r}}$ is the radial unit vector. Using the flux-freezing condition and spherical symmetry (de Avillez & Breitschwerdt 2005), we find the following relations for the initial and final magnetic fields (for further detail, see Appendix D):

$$B_{\parallel,\rm fin} = B_{\parallel,\rm ini}\left(\frac{r_{\rm ini}}{r_{\rm fin}}\right)^2, \quad (36)$$

$$B_{\perp,\rm fin} = B_{\perp,\rm ini}\left(\frac{\rho_{\rm fin} r_{\rm fin}}{\rho_{\rm ini} r_{\rm ini}}\right). \quad (37)$$

With this relation between the initial and final magnetic fields, we can relate their divergences as well,

$$\begin{aligned}\boldsymbol{\nabla} \cdot \boldsymbol{B}_{\rm fin} &= \boldsymbol{\nabla} \cdot \boldsymbol{B}_{\perp,\rm fin} + \boldsymbol{\nabla} \cdot \boldsymbol{B}_{\parallel,\rm fin} \\ &= \boldsymbol{\nabla} \cdot \boldsymbol{B}_{\perp,\rm ini}\left(\frac{\rho_{\rm fin} r_{\rm fin}}{\rho_{\rm ini} r_{\rm ini}}\right) + \boldsymbol{\nabla} \cdot \boldsymbol{B}_{\parallel,\rm ini}\left(\frac{r_{\rm ini}}{r_{\rm fin}}\right)^2 \\ &= \left(\frac{\rho_{\rm fin} r_{\rm fin}}{\rho_{\rm ini} r_{\rm ini}}\right)\boldsymbol{\nabla} \cdot \boldsymbol{B}_{\perp,\rm ini} + \left(\frac{r_{\rm ini}}{r_{\rm fin}}\right)^2 \boldsymbol{\nabla} \cdot \boldsymbol{B}_{\parallel,\rm ini}. \quad (38)\end{aligned}$$

Because our initial magnetic field has been interpolated to be divergence free, the magnetic field will remain divergence free at all times,

$$\begin{aligned}\boldsymbol{\nabla} \cdot \boldsymbol{B}_{\rm ini} = 0 &\Rightarrow \boldsymbol{\nabla} \cdot \boldsymbol{B}_{\perp,\rm ini} = \boldsymbol{\nabla} \cdot \boldsymbol{B}_{\parallel,\rm ini} = 0 \\ &\Rightarrow \boldsymbol{\nabla} \cdot \boldsymbol{B}_{\rm fin} = 0. \quad (39)\end{aligned}$$

5. Results

We have examined the trajectories for dust grains containing ^{60}Fe in an SNR expanding into an ISM containing a turbulent magnetic field with a Kolmogorov spectrum ($\eta = -5/3$). We assumed the grains contained material located originally at $r = 0.6 \times 10^9$ cm at the beginning of the hydrodynamic simulation; this corresponds to the highest concentration of ^{60}Fe within the ejecta (see Figure 1). The ^{60}Fe was assumed to condense into metallic Fe grains between 100–1000 days after the SN explosion, which corresponds to $r_{\rm gr} = 111$ au and $v_{\rm gr} = 382$ km s^{-1}. We assume that the grain is entrained within its surrounding dust cloud from the initial time step until encountering the RS at $t = 5000$ yr (with Rayleigh–Taylor instabilities present; by contrast without those instabilities, the

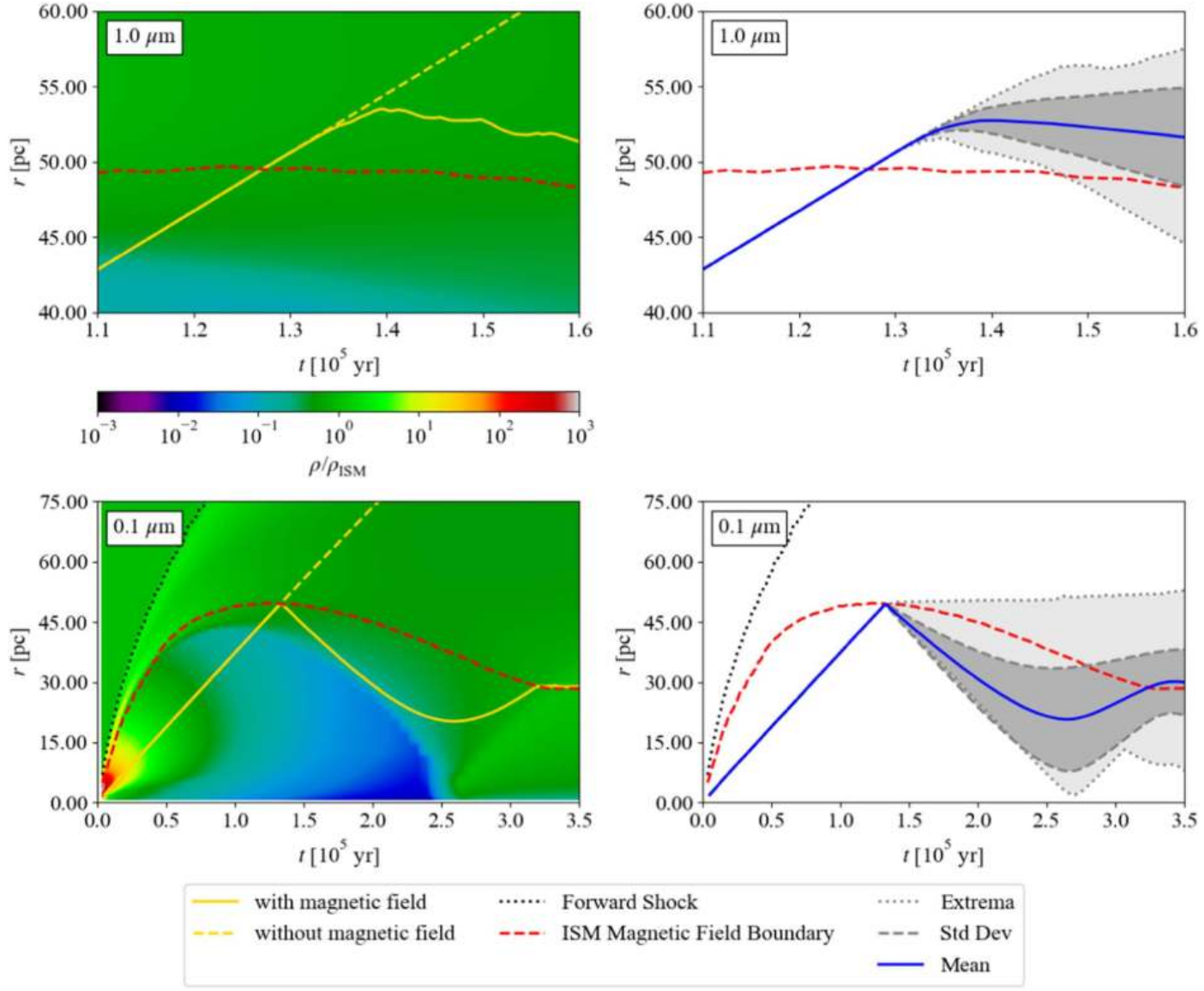

(a)

Figure 4. Panel (a): sample trajectories of metallic Fe grains of varying initial sizes on a density contour (left) and means/standard deviations/extrema of trajectories (right). The $\gtrsim$0.05 μm grains showed little influence by drag, traveling on similar trajectories when no magnetic field was present, but experiencing strong interactions in the presence of a magnetized ISM. Most 1 μm grains became trapped in the ISM magnetic field; their greater mass contributed to greater penetration before capture, but prevented later escape. In contrast, the 0.1 μm grains experienced mostly reflections at the first contact with the ISM magnetic field, while most grains became trapped at the second contact (although some grains do show additional reflections). The standard deviation assumes a normal distribution. Panel (b): sample trajectories of metallic Fe grains of varying initial sizes on a density contour (left) and means/standard deviations/extrema of trajectories (right). The $\lesssim$0.05 μm grains showed increasing influence by drag, delaying interaction with the magnetized ISM. Most 0.05 μm grains became trapped in the ISM magnetic field, although occasional reflections did occur. The 0.005 μm grains demonstrated no reflections and were completely trapped by the ISM magnetic field. Below $\leqslant$0.004 μm, drag and sputtering on dust grains becomes significant, with the smallest grains never reaching ISM material before being completely sputtered. The standard deviation assumes a normal distribution.

RS would not arrive until $t = 8600$ yr). As the RS passes, we assume that the grain is immediately exposed to the shocked SNR environment, and the simulation begins at $t_0 = 5000$ yr, $r_{\rm gr,0} = 1.96$ pc, $v_{\rm gr,0} = 382$ km s^{-1} (because we focused on the most stressing case, we performed runs only with Rayleigh–Taylor instabilities included).

To begin with, we examined the unmagnetized case. This serves as a basis of comparison for our magnetized examinations, as well as a comparison with previous works (see, e.g., Nozawa et al. 2007; Nath et al. 2008; Bocchio et al. 2016; Micelotta et al. 2016). For various grain sizes (0.005–1 μm), the grains demonstrate purely radial motion, gradually slowing as they approach the FS; see Figure 4, left panels. As should be expected, the larger grains maintain their velocities relative to smaller grains due to the former's greater mass. Qualitatively, we were able to reproduce the previous cited works' results.

Next, we examined a variety of post-RS grain sizes ranging from 0.005 to 1 μm with a magnetized ISM, and we ran the simulation 100 times to examine different configurations of the magnetic field; see Figure 4, right panels. The $a_{\rm gr,0} = 0.1$ μm grains showed the most noteworthy trajectories, with some being reflected nearly radially backwards into the SNR, and others being deflected along the edge of the SNR or becoming trapped. The $a_{\rm gr,0} = 1$ μm grains also showed strong

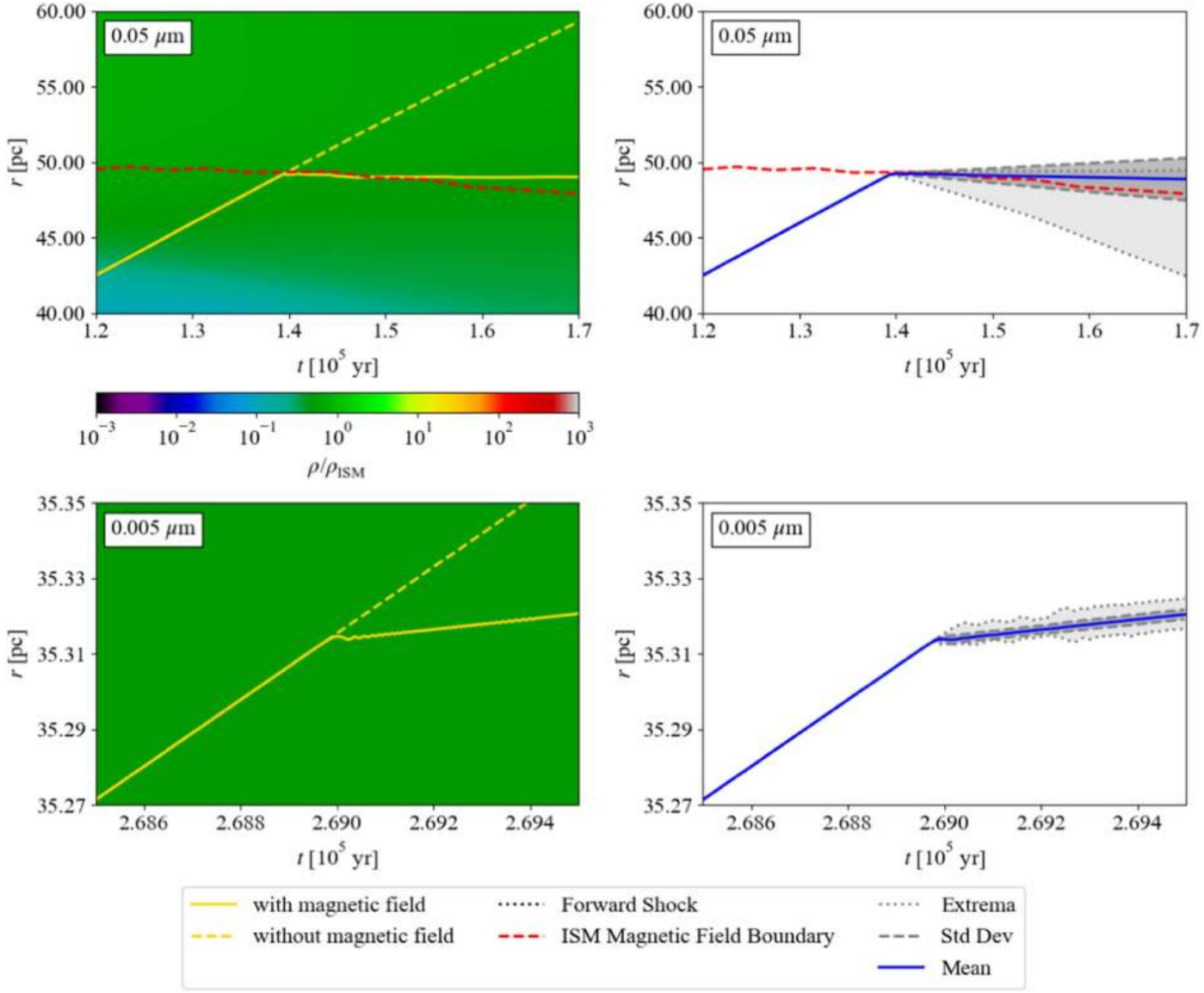

(b)

Figure 4. (Continued.)

reflections into the inner SNR as well as some trapping.[13] As the grains decrease in size, drag becomes more important delaying contact with the ISM magnetic field; $a_{\rm gr,0} = 0.05\ \mu$m grains will become mostly trapped by the ISM magnetic field, although some are reflected. The influence of drag on $a_{\rm gr,0} = 0.005\ \mu$m grains shows complete trapping and no reflections (see Figure 4). The $a_{\rm gr,0} \lesssim 0.002\ \mu$m grains completely sputter before reaching ISM material.

The $a_{\rm gr,0} = 0.1\ \mu$m grains' "pinball" behavior is particularly dramatic. They experience some drag and sputtering, but this effect is relatively minor since the relative velocity $v_{\rm rel} \lesssim 175\ {\rm km\ s^{-1}}$ for much of their transit; see Figure 5. There is no deflection (i.e., non-radial motion) of the grain's trajectory while the grain is traveling through pre-SN circumstellar material, see Figure 6. This is because there is (effectively) no magnetic field in this material. In contrast, shortly after encountering shocked ISM material, the frozen-in ISM magnetic field reflects the grain back into the SNR. This action is repeated as the grain transits the SNR and again encounters shocked ISM material. The charged dust grains ricochet inside the magnetized ISM material like pinballs (this boundary is roughly equivalent to the contact discontinuity; see, e.g., Wang & Chevalier 2002). Figure 7 shows that the grain penetrates the ISM material to some extent and allows us to verify that the grain is being reflected due to the magnetic field rather than a discontinuity inherent to our model.

Figure 8 shows results from 100 runs with an initial $a_{\rm gr,0} = 0.1\ \mu$m grain. Almost every grain is reflected nearly opposite to its initial radial direction, with some grains experiencing multiple reflections. These features appear as "U"- or "W"-shaped trajectories in Figure 8.

6. Predictions and Implications

6.1. Predictions: SN Dust Confinement and Evolution

The dust grain trajectories in our simulations are largely confined by the ISM magnetic field, and although our selection

[13] It should be noted that 1 μm is an *exceptionally* large dust grain, and we do not expect many, if any, such grains to form. We include them here for completeness.

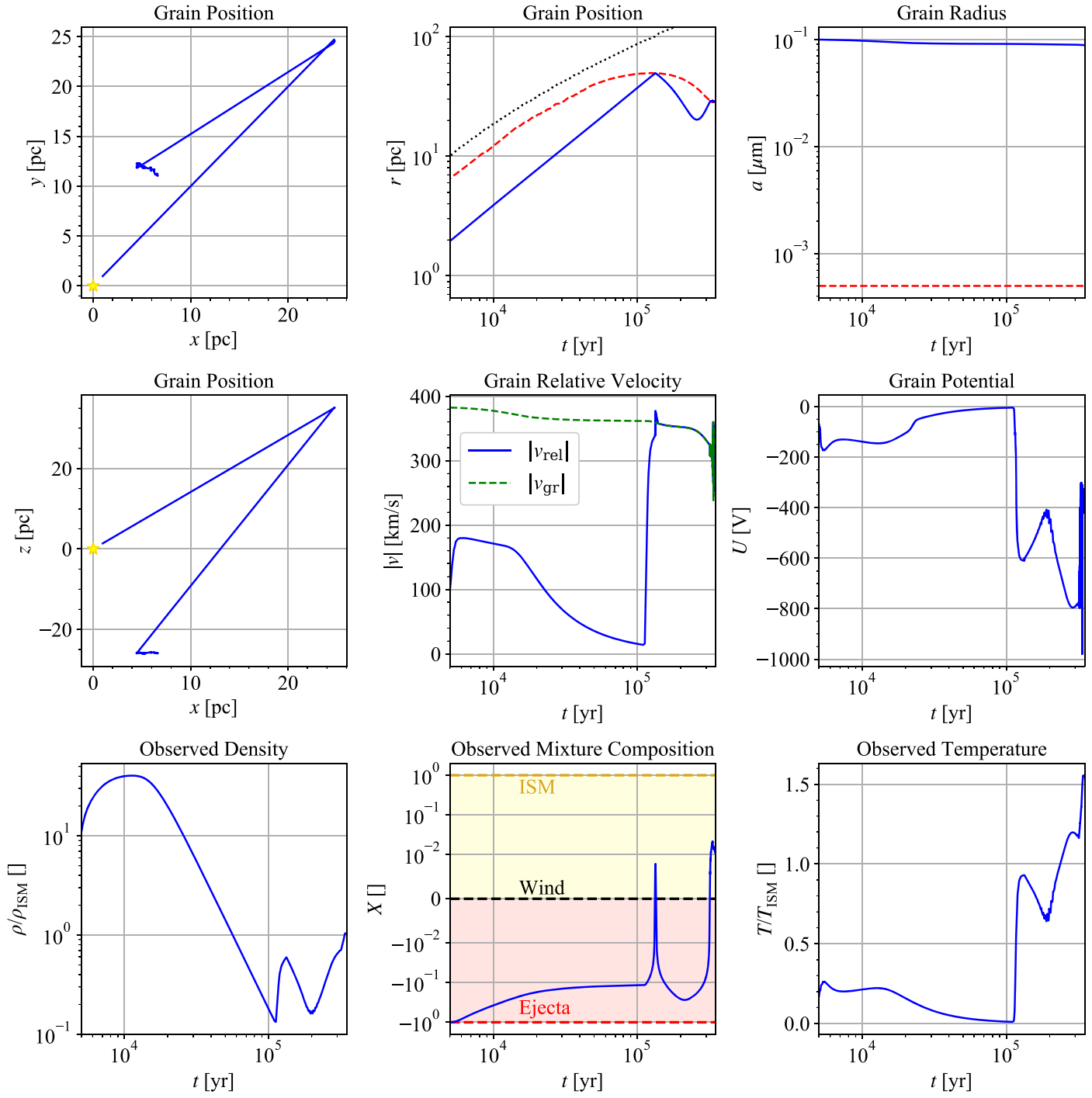

Figure 5. Summary of grain parameters for a sample 0.1 μm metallic Fe-grain. The top left and middle row left panels are projections of the grain's positions onto the x–y-(upper left) and x–z-planes (middle row left) with the yellow star representing the site of the SN. The upper center plot shows the grain's radial position, with the dotted, black line indicating the position of the forward shock and the dashed, red line indicating the boundary between the pre-SN stellar wind and the ISM material and ISM magnetic field. The first reflection occurs at $t \approx 1.3 \times 10^5$ yr, and the grain becomes trapped in the magnetic field at $t \approx 3 \times 10^5$ yr. The rate of deceleration due to drag changes as the grain moves through different densities (bottom left panel) and is most pronounced following reflections, when the relative velocity, $v_{\rm rel}$, between the grain and plasma is greatest (middle row center panel). The rate of grain erosion due to sputtering remains fairly constant throughout the entire simulation (upper right panel), but the grain potential makes sharp fluctuations while generally staying negative (middle row right panel) and strongly mirrors the surrounding plasma temperature fluctuations (bottom right panel). The dashed red line on the grain radius plot represents the sputtering limit; below this, the grain is assumed to have been destroyed. The bottom center panel shows the pre-SN material the grain passes through; −1 is pure ejecta, 0 is pure wind, and 1 is pure ISM material with fractional values representing mixtures (there is no ISM/ejecta mixing). The grain's reflection/trapping directly correlates to the grain's encounters with ISM material.

of SN parameters are motivated by the near-Earth scenario, this dust confinement effect should not be sensitive to that particular scenario. The grain reflections and trapping occurred in regions with magnetic field strengths ∼tens of nanogauss (nG). Even if our assumption that the ISM magnetic field scales as $B \sim \rho^{2/3}$ is not strictly adhered to, it is still expected that the magnetic field would scale in the range of $B \sim \rho^{[0,1]}$ (de Avillez & Breitschwerdt 2005). This would mean that regardless of the scaling used, dust grains would eventually encounter magnetic field strengths sufficient to cause

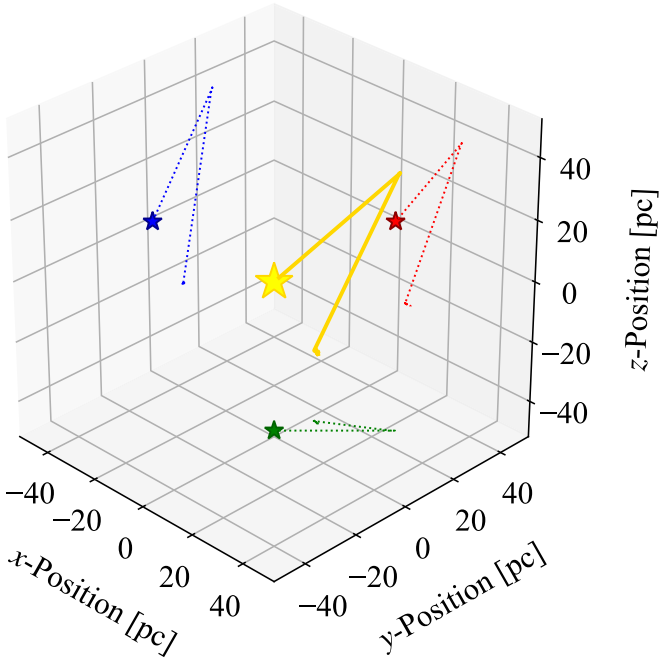

Figure 6. Three-dimensional plot of a sample 0.1 μm metallic Fe-grain. The yellow lines are the 3D plot of the grain trajectory, with the green, red, and blue lines showing the x–y-, x–z-, and y–z-planes, respectively. The stars represent the location of the SN. Note that this is the same sample shown in Figure 5. An animation is available. The video shows one rotation around the Z-axis. The realtime duration is 24 s.

(An animation of this figure is available.)

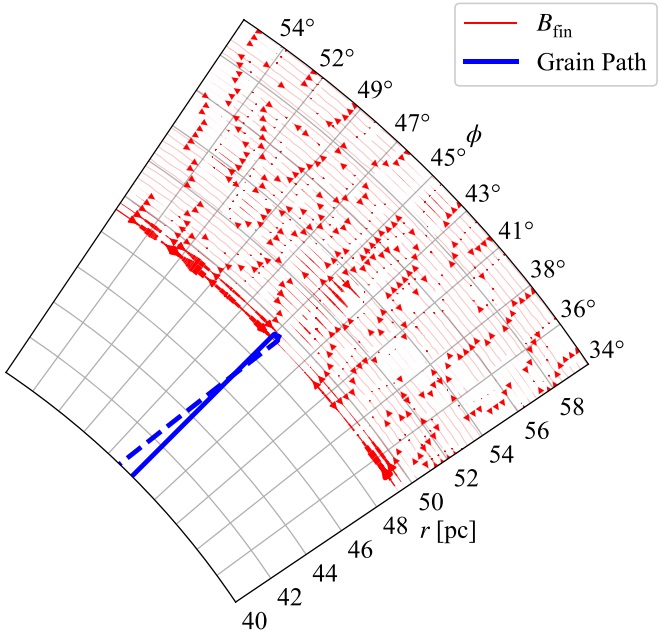

Figure 7. The azimuthal trajectory of a sample 0.1 μm metallic Fe-grain along its initial radial direction. The grain path is shown as a solid blue until reflection, and a dashed, blue line afterwards. The red lines are the magnetic field lines at the moment of reflection ($t \approx 130$ kyr, $r \approx 50$ pc). Note the stretching of the magnetic field lines parallel to the FS and the lack of a magnetic field interior to 49 pc representing pre-SN stellar and wind material. Because of mixing of the wind and ISM material, the magnetic field gradually increases in strength, until it is strong enough to reflect the dust grain.

reflections/trapping as they propagate radially outwards in our simulations (albeit at slightly different location depending on the scaling value). Further, our chosen magnetic field is weaker than the average ISM magnetic field, suggesting that dust confinement is a property of SNe in general rather than this specific scenario.

Given that propagation in the ISM magnetic field is the limiting mechanism for the larger SN dust grains, it is possible to estimate the maximum radial position for the dust grains within the SNR. Since the ISM material must be pushed away by the ejecta, we can assume the dust's maximum radial position is where the total ejected and stellar wind material equals the swept-up ISM material such that

$$M_{\rm ej} + M_{\rm wind} = M_{\rm swept-upISM} = \frac{4}{3}\pi\rho_{\rm ISM}R_{\rm dust}^3, \tag{40}$$

$$\Rightarrow R_{\rm dust} = 24\ {\rm pc}\left(\frac{M_{\rm ej}+M_{\rm wind}}{90\,M_\odot}\right)^{1/3}\left(\frac{0.61}{\mu_{\rm ISM}}\right)^{1/3} \times \left(\frac{0.1\ {\rm cm}^{-3}}{n_{\rm ISM}}\right)^{1/3}. \tag{41}$$

For an observational comparison, the core-collapse SNR Sagittarius (Sgr) A East is ~10 kyr old, and recent SOFIA observations have confirmed the presence of dust within the center of the SNR (Lau et al. 2015). The dust is confined to the inner ~2 pc diameter (Lau et al. 2015), while the outer radio shell (that corresponds to the FS) has a diameter of ~7 pc (Maeda et al. 2002; Lau et al. 2015). Using the estimated conditions of the progenitor: $M_{\rm ej} = 2\,M_\odot$ (Maeda et al. 2002), $M_{\rm wind} = 10\,M_\odot$ (Mezger et al. 1989), and $n_{\rm ISM} = 1000\,{\rm cm}^{-3}$ (Maeda et al. 2002; Lau et al. 2015), this gives $R_{\rm dust} = 0.57$ pc, which is in good agreement with the observed dust region of Sgr A East SNR.

6.2. Dust Delivery of Radioisotopes from Near-Earth SNe

The Sco–Cen OB association has frequently been expected to be the source of the ^{60}Fe given the large number of SN-capable progenitors within that association. However, based on these results, the possibility of a Sco–Cen progenitor ($D \sim 130$ pc) as the source of the ^{60}Fe seems extremely unlikely, given that magnetic fields restrict the movement of the larger (i.e., $a_{\rm gr} \gtrsim 0.002\,\mu$m) grains, and drag halts the movement of smaller grains. Although Sco–Cen may have yielded a larger, more powerful progenitor (e.g., a 15 $M_\odot$ CCSN; Hyde & Pecaut 2018), the additional explosive energy ($E_{\rm SN}$) is not expected to be able to push back the ISM magnetic field over 100 pc. ISM magnetic fields would severely restrict the passage of dust grains. In order for a Sco–Cen source of ^{60}Fe, *some mechanism(s) would be needed to either drive the ISM magnetic field back or allow charged dust grains to pass more efficiently*. However, Tuc–Hor is still a likely source, as our simulation showed consistent dust propagation out to ~50 pc, which (considering the uncertainty in the initial ISM density) is consistent with the distance to Tuc–Hor (~45–60 pc).

The implications of magnetic reflections are that the grains are not confined to the shell region as assumed by Fry et al. (2015, 2016), Breitschwerdt et al. (2016), Feige (2016), Feige et al. (2017), and Schulreich et al. (2017), but they are confined to the interior of the SNR. These reflections also alter the assumption of a plane-wave arrival of SN dust grains into the solar system. It even appears likely that, after the SNR envelops

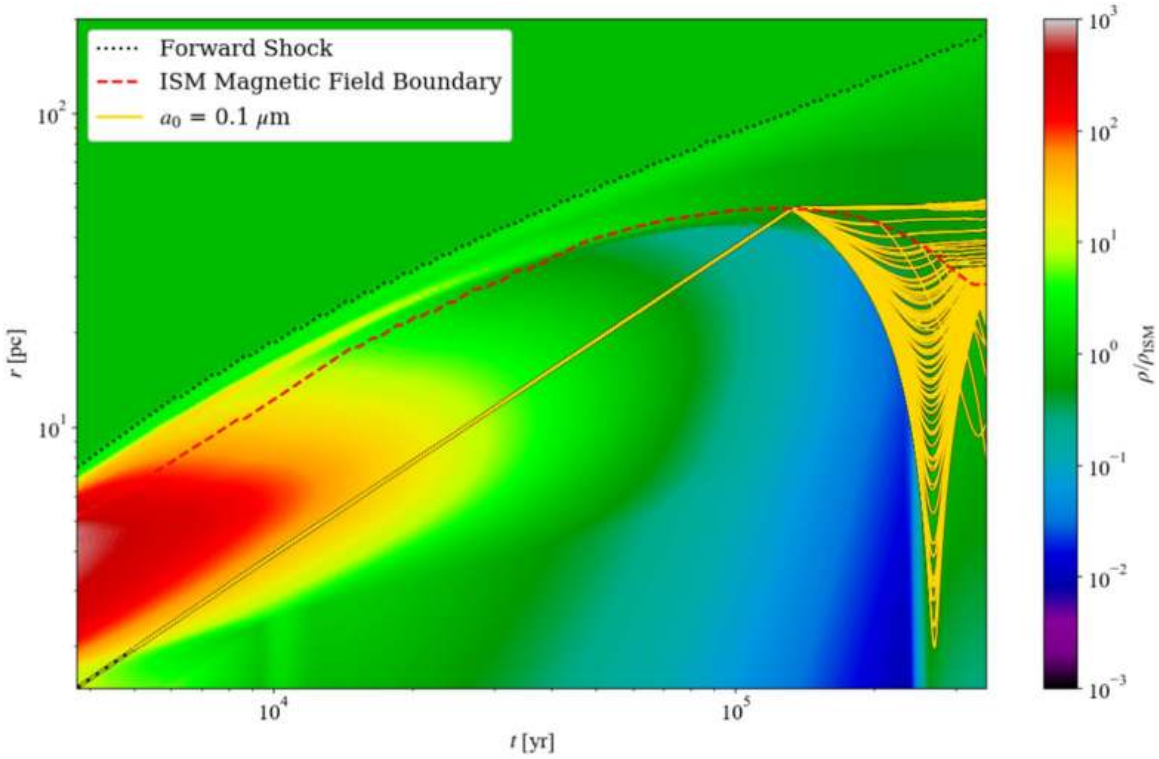

Figure 8. Multiple trajectories of metallic Fe grains on a density contour. Trajectories for 100 grains (plotted in yellow) are shown with an initial grain radius of $a_{\rm gr} = 0.1\ \mu$m and encounter the ISM magnetic field. The grain trajectory prior to cloud crushing is shown with dashed, yellow lines and solid, yellow lines when the cloud has dissipated and the grain is exposed to the SNR plasma. Note that most grains remain in the $r \lesssim 50$ pc region while bouncing within the shell. The FS is shown with the dotted, black curve, and the contact discontinuity between ejecta and ISM material is shown with a dashed, red line.

the solar system, some dust grains will bounce off the contact discontinuity and approach Earth from a direction nearly opposite of the SN! Further characterization of this passage is needed to determine the viability of using lunar samples to determine the direction to the SN as proposed by Fry et al. (2016). This potentially explains the surprisingly extended ~1 Myr duration of the signal (Fitoussi et al. 2008; Ludwig et al. 2016; Wallner et al. 2016; Fields et al. 2019) but negates the proposal by Fry et al. (2015) of using time-resolved samples as an alternate gauge of the SN's distance. On the other hand, the time-resolved samples will yield a measure of the SNR's propagation and internal dust distribution.

Finally, we note that our approach and findings are complementary with the work of Ellison et al. (1997). These authors showed that supernova dust should be dynamically decoupled from the plasma and that some grains can be accelerated. They argued that sputtering of these fast grains provides the nonthermal ions that are injected into and accelerated by the supernova shocks. Ellison et al. (1997) concluded that this mechanism could be the origin of the cosmic-ray enhancement in refractory elements. Our work extends and complements this picture: the ^{60}Fe-bearing dust that survives sputtering leads to the terrestrial and lunar signals, while the sputtered-ions supernova may be responsible for the ^{60}Fe seen in cosmic-rays by Binns et al. (2016).

6.3. Magnetic Field Discussion

In this exploratory calculation, we have treated the magnetic field in an idealized manner. We have neglected entirely any field in the supernova wind and ejecta, and we have treated the ISM field as a random Gaussian field with an entirely turbulent, power-law (i.e., $\mathcal{E}_k \sim k^{\eta}$) spectrum. These choices can influence our results.

The absence of magnetic fields in the supernova wind and ejecta leads to the undeflected, radial motion of the dust particles within this material. Then, the encounter with the ISM field results ultimately in magnetic mirroring and/or trapping. Mirroring occurs for grains moving from field strengths $B_{\rm min}$ to $B_{\rm max}$ with velocities that satisfy the "loss cone" condition (from Equation (7)):

$$\frac{v_{\parallel}}{v_{\perp}} < \sqrt{\frac{B_{\rm max}}{B_{\rm min}} - 1} \tag{42}$$

where $v_{\parallel}$ and $v_{\perp}$ are the velocity components parallel and perpendicular to the field, respectively. In the limit where $B_{\rm min} \to 0$, all are reflected. Under our expected magnetic field initial conditions, (see Section 4.4), our expected values for $v_{\parallel}/v_{\perp} \lesssim 1000$, suggesting that the vast majority of (but not all) encounters should experience magnetic reflections. Because our simulations allow for mixing between non-ISM and ISM material, the dust grain's encounter with a magnetic field is not abrupt, and so, magnetic reflections are not guaranteed in our simulation environment, and, in fact, not all encounters in our results do exhibit reflections. However, a more complete magnetic field description would better ensure that any grain behavior is not the result of a model's intrinsic construction.

Another choice was to use a completely turbulent (i.e., *disordered*) field with no uniform (i.e., *ordered*) component. If the field has a nonzero *ordered* component, this can direct the grains along field lines and impede motion perpendicular to the magnetic field. Examining a strictly uniform case and a

combination of uniform-turbulent configurations would further characterize the magnetic mirroring effect in future follow-up studies.

Lastly, the selection of a random Gaussian field leads to turbulent field behavior that has its dominant component on the largest scales ($\lambda_{\rm outer} = 5$ pc, see also Figure 3). This can create an overly smooth field at small scales as suggested by turbulence simulations (e.g., Wilson 1998; Burkhart et al. 2009) and as seen in solar wind data (e.g., Sorriso-Valvo et al. 1999). Examining the influence of this difference at small scales is beyond the scope of this work but should be included in future work to examine its influence on trapping and mirroring effects.

7. Conclusions

We have studied the motion and evolution of dust grains created in an unmagnetized SNR exploding into a magnetized ISM. The SNR evolution is described via a 1D+ model assuming spherical symmetry that includes angle-averaged effects of Rayleigh–Taylor instabilities and resultant mixing. The ISM magnetic fields are initialized with a turbulent magnetic field with a Kolmogorov spectrum and evolve kinematically via flux freezing; thus, they are altered by the shock. We included the effects of drag, sputtering, and charging on the dust grains, and simulate the motions of grains of different sizes.

In the absence of magnetic fields, or equivalently for uncharged dust, our results are similar to those of other groups (see, e.g., Nozawa et al. 2007; Nath et al. 2008; Bocchio et al. 2016; Micelotta et al. 2016). We assume that the grains are initially entrained with the gas from which they are born, and, thus, have radial trajectories. After the ejecta encounter the RS, the dust grains decouple from the decelerated gas and move toward the FS. For large grains, the effects of drag and sputtering are small enough that the grains survive to pass close to or across and beyond the FS into the ISM. The result would be a "halo" of the largest dust grains that precedes the FS.

However, we find that magnetic fields have a dramatic effect, leading to qualitatively new dust trajectories and fates compared to the unmagnetized case. In particular, we find that the dust grains typically suffer large deflections when encountering the shocked ISM, in which the pre-existing turbulent magnetic fields have been altered. The main effect we observe is magnetic trapping and mirroring, occurring at the interface between the SN ejecta and the shocked ISM. The reflected particle moves back into the SN ejecta, traversing the SNR until it encounters the ejecta/ISM interface again; effectively, the dust grain has become a pinball within the SNR. The resulting motion is thus a series of ricochets inside the SN ejecta region. The presence of ISM magnetic fields means that dust is not distributed throughout the entire SNR but confined much deeper within the SNR.

Our results show that the inclusion of Rayleigh–Taylor instabilities is important. Figure 8 shows that the grains enter the shocked medium as early as 5000 yr after the explosion, rather than later at $\sim 10^5$ yr when the RS proceeds inward to the center of the SNR. By entering the shocked plasma earlier, grains are subject to erosion and drag longer.

Lastly, the presence of magnetic reflections also suggests that grain–grain interactions and shattering due to shock crossings may not be entirely negligible. The grain reflections into the SNR greatly increase the likelihood of collisions compared to the purely radial trajectories assumed to date (an example of a grain–grain collision approach is used by Kirchschlager et al. 2019). Additionally, as seen in Figure 8, grains crossing the RS multiple times will be subject to repeated shattering, reducing the likelihood for long-term survival (see also Williams & Temim 2016).

The overarching message of our study is that magnetic fields have a dramatic effect on the evolution and survival of SN dust. This has important implications not only for the terrestrial and lunar deposition of ^{60}Fe and other radioisotopes but also for the evolution of dust in SNRs generally and possibly for the role of supernova dust in cosmic-ray acceleration. We will explore these implications more in future work.

Further simulations using other radioisotopes are planned. Based on these ^{60}Fe results, it appears that ^{26}Al and ^{41}Ca (which form in the front portion of the ejecta, making them more likely to encounter the RS before ^{60}Fe) will be exposed to the hot SNR plasma earlier. Simulations examining ^{26}Al could readily be compared to results from Feige et al. (2018). Since their density is less than metallic Fe, they will be more sensitive to drag and the magnetic fields due to their lower masses. A portion of ^{53}Mn is synthesized slightly deeper in the ejecta and may form MnS, but the bulk of ^{41}Ca and ^{53}Mn are deeper in the ejecta than ^{60}Fe. The question remains into what type of dust, if any, they will be incorporated. Additional simulations are also planned to characterize fully the dust grains' movements within the SNR. These include varying the ISM density and magnetic field, varying the grain composition/sizes further, and examining the case in which there is no H/He envelope around the pre-SN star (Fremling et al. 2016). Additionally, the use of a Non-Uniform Fast Fourier Transform (NUFFT) for the turbulent magnetic field description would allow for characterization down to the dissipation scale (see, e.g., Haines & Jones 1988; Hamilton 2000; Greengard & Lee 2004; Hamilton 2015).

B.J.F. would like to thank Paul Duffell for his assistance in using the RT1D code, and Shinya Wanajo for kindly sharing his ECSN nucleosynthesis data; this work would not have been possible without either. B.J.F. would also like to thank Jenny Feige for her comments and suggestions regarding this work. We are grateful for encouragement and illuminating discussions with Bruce Draine, Paul Ricker, Charles Gammie, Ada Ertel, and Jesse Miller. The work of J.E. is supported in part by STFC (UK) via the research grant ST/L000326/1 and in part by the Estonian Research Council via a Mobilitas Pluss grant.

Appendix A
List of Variables

Variable—Description (common value or unit of measure)
$*$—(as superscript) parameter in characteristic units (dimensionless)
$\|\|$—(as subscript) parallel component
$\perp$—(as subscript) perpendicular component
0—(as subscript) "initial value for simulation"
$a_{\rm gr}$—radius of dust grain (μm)
$a_{\rm cloud}$—radius of cloud (km)
$a_{\rm sc}$—screening length (μm)
A—magnetic vector potential (G cm)
$\mathbb{A}$—local vector potential (G cm^2)
α—angle (radians)
$\boldsymbol{b}$—perturbed magnetic field (G)
$\boldsymbol{B}$—magnetic field (G)
c—speed of light ($\sim 3 \times 10^5$ km s^{-1})

(Continued)

$C_{\rm abs}$—absorption cross section ($\rm cm^2$)
$C_{\rm coll}$—collisional cross section ($\rm cm^2$)
ch—(as subscript) "characteristic scale"
$\mathbb{C}$—scaling constant ($\rm G^2\ pc^2$)
χ—generic/dummy variable (dimensionless)
D—distance to Earth (pc)
$\mathbb{D}$—dilution factor (dimensionless)
δ_j—secondary electron yield (dimensionless)
$\delta_{\rm max}$—maximum yield from a bulk solid (dimensionless)
Δ_j—penetration threshold energy (eV)
e—elementary charge (4.803×10^{-10} Fr)
E—energy (erg)
E_1—energy constant (eV)
E_2—energy constant (keV)
$E_{\rm bind}$—binding energy (eV)
E_e—most probable energy from electrons (eV)
E_γ—most probable energy from photons (eV)
E_H—ionization energy of hydrogen (13.6 eV)
$E_{\rm ion}$—most probable energy from ions(eV)
$E_{\rm low}$—minimum photoelectric emission energy (eV)
$E_{\rm max}$—energy at maximum yield from a bulk solid (eV)
$E_{\rm min}$—minimum emission energy (eV)
$E_{\rm SN}$—energy of SN (erg)
$E_{\rm th}$—threshold energy (eV)
$\mathcal{E}$—specific energy ($\rm erg\ g^{-1}$)
$\mathbb{E}$—energy density ($\rm erg\ cm^{-3}$)
ϵ—reduced energy (dimensionless)
η—spectral index (dimensionless)
f_1—fitting function (dimensionless)
f_2—fitting function (dimensionless)
f_j—Maxwellian velocity distribution function (dimensionless)
fin—(as subscript) "final value"
$\boldsymbol{F}$—force (dyn)
$\mathcal{F}$—fluence ($\rm atoms\ cm^{-2}$)
$\mathbb{F}_{\rm mag}$—magnetic flux ($\rm G\ cm^2$)
$\mathbb{F}_{\gamma,h\nu}$—spectral photon flux ($\rm photons\ cm^{-2}\ s^{-1}\ eV^{-1}$)
g—maximum fraction energy transfer (dimensionless)
G_0—collisional drag function (dimensionless)
G_2—Coulomb drag function (dimensionless)
Γ—adiabatic index (dimensionless)
h—Planck's constant ($6.626 \times 10^{-27}\ \rm erg\ s^{-1}$)
ini—(as subscript) "initial value"
$\mathcal{I}$—charge current ($\rm Fr\ s^{-1}$)
$\boldsymbol{J}$—charge current density ($\rm Fr\ cm^{-2}\ s^{-1}$)
k—(as subscript) "Fourier counterpart"
$\boldsymbol{k}$—wavenumber ($\rm cm^{-1}$)
$k_{\rm B}$—Boltzmann constant ($1.38 \times 10^{-16}\ \rm erg\ K^{-1}$)
κ—sputtering free parameter (dimensionless)
l—length (cm)
λ—length scale (km)
Λ—charge parameter (dimensionless)
m—mass (e.g., of p^+, e^-, H, dust grain, etc.) (g)
$m_{\rm u}$—atomic mass unit (1.66×10^{-24} g)
$m_{\rm sp}$—sputtered mass (g)
$M_{\rm ej}$—mass of the ejecta ($M_\odot$)
$M_{\rm enclosed}$—mass enclosed in spherical shell ($M_\odot$)
$\dot{M}_{\rm wind}$—stellar wind mass loss ($M_\odot\ \rm yr^{-1}$)
$\mu_{\rm ej}$—mean mass of the ejecta (dimensionless)
$\mu_{\rm envel}$—mean mass of the stellar envelope (dimensionless)
$\mu_{\rm ISM}$—mean mass of the ISM (dimensionless)
n—number density ($\rm cm^{-3}$)
N—number of values/points (dimensionless)
$\mathcal{N}$—material current ($\rm cm\ s^{-1}$)
ν—frequency (Hz)
ω—grain penetration factor (dimensionless)
Ω—solid angle (sr)
p—momentum ($\rm g\ cm\ s^{-1}$)

(Continued)

P—pressure ($\rm dyn\ cm^{-2}$)
$\mathcal{P}$—specific power ($\rm erg\ cm^2\ g^{-1}$)
ϕ—angle (radians)
Φ—potential parameter (dimensionless)
ψ—radial basis function (dimensionless)
£$_e$—electron range power index (dimensionless)
$q_{\rm gr}$—charge of grain (Fr)
$\boldsymbol{r}$—radial position (cm)
$R_{\rm bounce}$—position at bounce (cm)
R_e—electron range (nm)
$R_{\rm gyro}$—gyro radius (pc)
R_m—reduced range (dimensionless)
$R_{\rm SN}$—position of forward shock (pc)
$\mathbb{R}$—range constant (nm)
ρ—mass density (e.g., of ISM, etc.) ($\rm g\ cm^{-3}$)
$\rho_{\rm gr}$—mass density of grain ($\rm g\ cm^{-3}$)
ϱ_e—energy distribution for secondary electrons emitted by electrons ($\rm eV^{-1}$)
ϱ_γ—energy distribution for secondary electrons emitted by photons ($\rm eV^{-1}$)
$\varrho_{\rm ion}$—energy distribution for secondary electrons emitted by ions ($\rm eV^{-1}$)
s—velocity parameter (dimensionless)
S—stopping cross section ($\rm cm^2\ erg$)
$\mathbb{S}$—scaling factor ($\rm cm^{-2}$)
σ_A—standard deviation of the magnetic vector potential ($\rm G\ pc^{-1}$)
ς—elastic reduced stopping cross section (1)
t—time (s)
T—temperature (K)
$T_5 \equiv T\ (10^5\ \rm K)^{-1}$ (dimensionless)
$\tau_{1/2}$—half-life (Myr)
$\tau_{\rm cc}$—cloud crushing time (yr)
$\tau_{\rm charge}$—charging time(yr)
$\tau_{\rm gyro}$—gyro period (yr)
θ—angle (radians)
$\boldsymbol{u}$—perturbed velocity ($\rm cm\ s^{-1}$)
$U_{\rm gr}$—potential of dust grain (V)
$\boldsymbol{v}$—velocity ($\rm cm\ s^{-1}$)
$v_7 \equiv v\ (10^7\ \rm cm\ s^{-1})^{-1}$ (dimensionless)
$\boldsymbol{v}_{\rm gr}$—velocity of grain relative to center of explosion ($\rm cm\ s^{-1}$)
$v_{\rm ej}$—velocity of the ejecta ($\rm km\ s^{-1}$)
$v_{\rm esc}$—escape velocity ($\rm km\ s^{-1}$)
$v_{\rm rel}$—relative velocity ($\rm km\ s^{-1}$)
$v_{\rm RS}$—relative velocity of reverse shock ($\rm km\ s^{-1}$)
$v_{\mathcal{T}}$—thermal velocity ($\rm km\ s^{-1}$)
$v_{\rm wind}$—stellar wind velocity ($\rm km\ s^{-1}$)
W—work function (eV)
ξ—sputtering function (dimensionless)
X—composition fraction (dimensionless)
Y^0—backward sputtering yield at normal incidence ($\rm atoms\ ion^{-1}$)
Z—charge number (dimensionless)

Appendix B
Turbulent Magnetic Field

We begin by assuming the ISM has fully developed and stationary (time-translation invariant) MHD turbulence that is homogeneous and isotropic. We define the turbulent field's total velocity, $\boldsymbol{v}$, and magnetic field, $\boldsymbol{B}$, at a point, $\boldsymbol{x}$, as

$$\begin{aligned} \boldsymbol{v}(\boldsymbol{x}) &= \langle \boldsymbol{v} \rangle + \boldsymbol{u}(\boldsymbol{x}) \rightleftharpoons \boldsymbol{v}_k = \langle \boldsymbol{v}_k \rangle + \boldsymbol{u}_k, \\ \boldsymbol{B}(\boldsymbol{x}) &= \langle \boldsymbol{B} \rangle + \boldsymbol{b}(\boldsymbol{x}) \rightleftharpoons \boldsymbol{B}_k = \langle \boldsymbol{B}_k \rangle + \boldsymbol{b}_k, \end{aligned} \tag{B1}$$

where $\langle \boldsymbol{v} \rangle$ and $\langle \boldsymbol{B} \rangle$ are the average velocity and magnetic fields, respectively, $\boldsymbol{u}$ and $\boldsymbol{b}$ are the perturbed velocity and magnetic fields, respectively, and the subscript, k, denotes the Fourier counterpart (i.e., $\boldsymbol{B}(\boldsymbol{x}) \rightleftharpoons \boldsymbol{B}_k$). Because the turbulence is homogeneous and

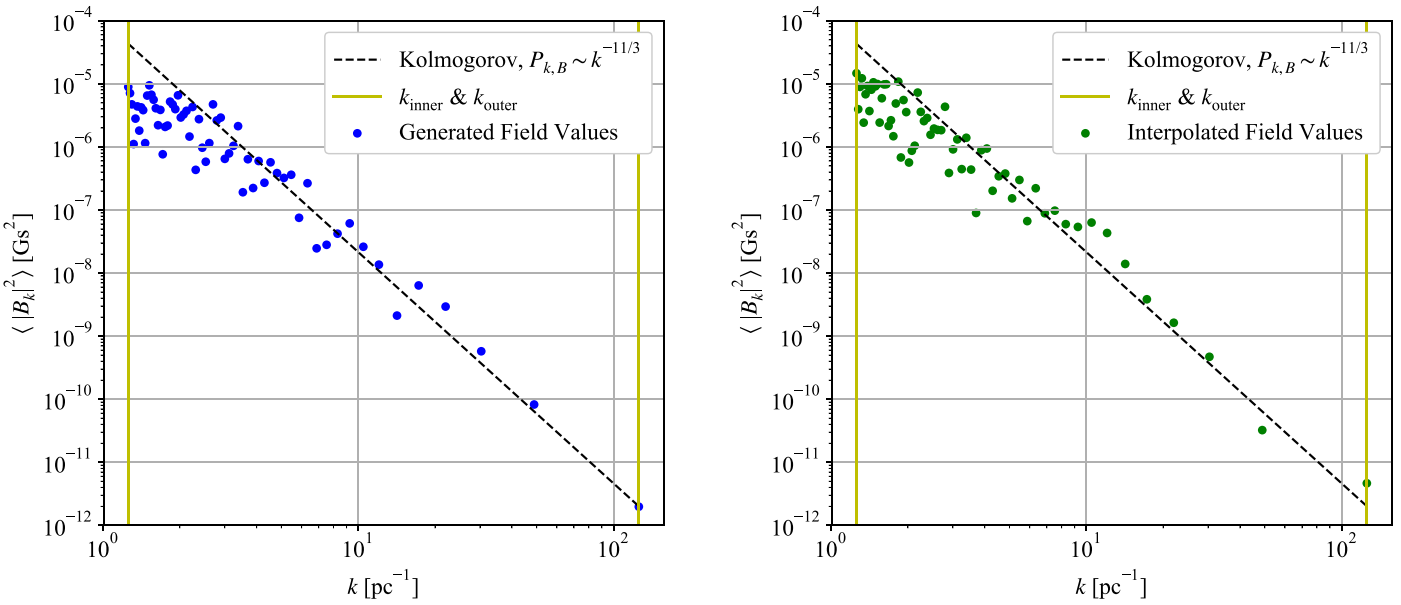

Figure B1. Sample power spectra for MHD turbulence. Panel (a) shows the generated grid power spectrum for a Kolmogorov profile ($\mathcal{E}_k \sim k^{-5/3}$) with $\mathbb{C} = 1$ G^2 pc$^{17/3}$, $\lambda_{\rm outer} = 5$ pc, and $\lambda_{\rm inner} = 0.05$ pc. Panel (b) shows the interpolated field power spectrum for the same profile. The dashed line is shown for reference.

isotropic, we assume $\langle \boldsymbol{B} \rangle \approx 0 \Rightarrow \boldsymbol{B}(\boldsymbol{x}) \approx \boldsymbol{b}(\boldsymbol{x})$. Additionally, by Fourier analysis, the specific energy spectrum, $\mathcal{E}_k$, of the turbulence is

$$\mathcal{E}_k = \frac{1}{2}\langle u_k^2 \rangle + \frac{1}{8\pi\rho}\langle b_k^2 \rangle, \tag{B2}$$

where ρ is the average mass density of the ISM. For fully developed turbulence, we assume equipartition between the kinetic and magnetic energies $\left(\frac{1}{2}\langle u_k^2 \rangle \approx \frac{1}{8\pi\rho}\langle b_k^2 \rangle\right) \Rightarrow \mathcal{E}_k \propto \langle b_k^2 \rangle$. In the typical description of turbulence, energy is injected into the system at some outer scale ($\lambda_{\rm outer} = 2\pi/k_{\rm outer}$) and cascades from larger to smaller scales according to a power-law relation ($\mathcal{E}_k \sim k^{\eta}$), until it is dissipated at some inner scale ($\lambda_{\rm inner} = 2\pi/k_{\rm inner}$) by viscous forces.

In order to create a vector field with this behavior, we use the technique outlined by Zel'dovich (1970) and Efstathiou et al. (1985) and applied to turbulence in several papers (e.g., Dubinski et al. 1995; Wallin et al. 1998; Wiebe & Watson 1998; Watson et al. 2001). Most of these examples used this technique to generate incompressible velocity fields (i.e., $\boldsymbol{\nabla} \cdot \boldsymbol{v} = 0$), but since we require our magnetic field to be divergence free (i.e., $\boldsymbol{\nabla} \cdot \boldsymbol{B} = 0$), this technique is appropriate here as well.

First, we calculate the specific power spectrum, $\mathcal{P}$, from the energy spectrum of the desired field,

$$\mathcal{E}_k dk = \mathcal{P}_k d^3k \Rightarrow \mathcal{P}_{k,\boldsymbol{B}} \equiv \langle |B_k|^2 \rangle \sim k^{\eta-2}. \tag{B3}$$

The magnetic field is divergence free, $\boldsymbol{\nabla} \cdot \boldsymbol{B} = 0$, so

$$\boldsymbol{B} = \boldsymbol{\nabla} \times \boldsymbol{A} \rightleftharpoons \boldsymbol{B}_k = i\boldsymbol{k} \times \boldsymbol{A}_k, \tag{B4}$$

where $\boldsymbol{A}$ is the vector potential of the magnetic field. This implies that the power spectrum of the potential is

$$\mathcal{P}_{k,\boldsymbol{A}} \equiv \langle |A_k|^2 \rangle \sim k^{\eta-4}, \tag{B5}$$

for the Fourier components that are described by a Gaussian distribution (Dubinski et al. 1995). In order to prevent an increase in the spectrum beyond scales where the energy is injected, a cutoff wavenumber is introduced so that (Dubinski et al. 1995)

$$\mathcal{P}_{k,\boldsymbol{A}} \equiv \langle |A_k|^2 \rangle \sim (k^2 + k_{\rm outer}^2)^{(\eta-4)/2}. \tag{B6}$$

The vector components of $\boldsymbol{A}_k$ (both real and imaginary) are generated via a Gaussian distribution (Wallin et al. 1998)

$$f(A_k;\, \sigma_A) = \frac{1}{\sigma_A\sqrt{2\pi}} \exp\left[-\left(\frac{A_k^2}{2\sigma_A^2}\right)\right], \tag{B7}$$

$$\langle |A_{k,\{x,y,z\}}^{\{\rm Re,Im\}}|^2 \rangle = \sigma_A^2 = \mathbb{C}(k^2 + k_{\rm outer}^2)^{(\eta-4)/2}, \tag{B8}$$

$$\begin{aligned} A_{k,x} &= A_{k,x}^{\rm Re} + iA_{k,x}^{\rm Im}, \\ A_{k,y} &= A_{k,y}^{\rm Re} + iA_{k,y}^{\rm Im}, \\ A_{k,z} &= A_{k,z}^{\rm Re} + iA_{k,z}^{\rm Im}, \\ \boldsymbol{A}_k &= \langle A_{k,x}, A_{k,y}, A_{k,z} \rangle, \end{aligned} \tag{B9}$$

where σ_A is the standard deviation, and $\mathbb{C}$ is a constant that is the same for all components and is adjusted to scale to the desired value of $\langle B \rangle$. The value of $\boldsymbol{B}_k$ is then found by Equation (B4), then the inverse Fourier transform of $\boldsymbol{B}_k$ is taken to find $\boldsymbol{B}(\boldsymbol{x})$. The corresponding positions for $\boldsymbol{B}(\boldsymbol{x})$ are found by $\{x, y, z\} = 2\pi/\{k_x, k_y, k_z\}$; see Figure B1.

The spectral index, η, is chosen based on the desired phenomenology; for example, the Kolmogorov spectrum (Kolmogorov 1941; Goldreich & Sridhar 1995): $\eta = -5/3$, the Iroshnikov–Kraichnan/strong spectrum (Iroshnikov 1964; Kraichnan 1965): $\eta = -3/2$, and the universal/weak spectrum: $\eta = -2$. The Kolmogorov spectrum assumes an incompressible fluid, which is not the case in most astrophysical environments. Nevertheless, as noted by Dubinski et al. (1995) and Goldreich & Sridhar (1995), this spectrum

appears in many contexts including solar wind turbulence (Matthaeus & Goldstein 1982).

This procedure will create a turbulent field within a $\lambda_{\rm outer}^3$ grid; see Figure 3. In order to fill in more volume while minimizing computation time and memory, the entire simulation volume (200^3 pc^3) is divided into $\lambda_{\rm outer}^3$ boxes, and each box is filled with 1 of 24 randomly chosen, possible orientations of the generated turbulent field. These grid values of $\boldsymbol{B}(\boldsymbol{x})$ can now be interpolated in order to find the initial $\boldsymbol{B}(\boldsymbol{x})$ field at all points.

Appendix C
Interpolating the Magnetic Field

In creating a scheme for interpolating a magnetic field, $\boldsymbol{B}$, from N data points/values, it is first helpful to stipulate the properties of the final scheme. First, the interpolated field must satisfy Gauss' Law for Magnetic Fields, i.e., the magnetic field should be divergence free everywhere ($\boldsymbol{\nabla}\cdot\boldsymbol{B}=0$). Second, the scheme should yield the value of the data input magnetic field, $\boldsymbol{B}_i$, at each data point, $\boldsymbol{x}_i$, i.e., $\boldsymbol{B}(\boldsymbol{x}_i)=\boldsymbol{B}_i(\boldsymbol{x}_i)$; see also McNally (2011).

To begin, let an individual magnetic field, $\boldsymbol{B}_i$, be the curl of a vector potential, $\boldsymbol{A}_i$, such that $\boldsymbol{B}_i=\boldsymbol{\nabla}\times\boldsymbol{A}_i$. The total magnetic field is the superposition of the N individual fields,

$$\boldsymbol{B}=\sum_{i=1}^{N}\boldsymbol{B}_i=\sum_{i=1}^{N}\boldsymbol{\nabla}\times\boldsymbol{A}_i. \tag{C1}$$

In addition, we define another vector field, $\psi(\boldsymbol{r})\mathbb{A}$, at a position, $\boldsymbol{r}$, such that $\mathbb{A}$ is the value of the field at $\boldsymbol{r}=0$ and $\psi(\boldsymbol{r})$ is a scaling function with the properties that $\psi=1$ at $\boldsymbol{r}=0$, $\psi\to 0$ as $\boldsymbol{r}\to\infty$, and $\psi\geqslant 0\,\forall\boldsymbol{r}$. Although several functions satisfy these properties, for convenience, we chose $\psi(\boldsymbol{r})\equiv\exp\left[-\mathbb{S}r^2\right]$ where $r^2=x^2+y^2+z^2$ and x, y, and z are the components of $\boldsymbol{r}$. The scaling factor, $\mathbb{S}$, adjusts the influence of the data value at radius r. We chose a value of the reciprocal mean of the squared radii to the data points: $\mathbb{S}_i=1/\langle r_i^2\rangle$.

We then define the vector potential, $\boldsymbol{A}_i$, at a position, $\boldsymbol{x}$, in terms of the new vector, $\psi_i\mathbb{A}_i$, as

$$\boldsymbol{A}_i(\boldsymbol{x})=\boldsymbol{\nabla}\times(\psi(\boldsymbol{x}-\boldsymbol{x}_i)\mathbb{A}_i), \tag{C2}$$

where $\mathbb{A}_i$ is the value of the vector potential at $\boldsymbol{x}_i$. This means that the entire vector potential, $\boldsymbol{A}_i$, can be defined in terms of a single vector, $\mathbb{A}_i$.

Combining Equations (C1) and (C2), we can define the total magnetic field, $\boldsymbol{B}(\boldsymbol{x})$ at a position $\boldsymbol{x}$, as the superposition of N vectors, $\mathbb{A}_i$, scaled by a radial basis function, ψ, as

$$\begin{aligned}\boldsymbol{B}(\boldsymbol{x})&=\textstyle\sum_{i=1}^{N}\boldsymbol{\nabla}\times\boldsymbol{A}_i(\boldsymbol{x})=\sum_{i=1}^{N}\boldsymbol{\nabla}\times(\boldsymbol{\nabla}\times(\psi(\boldsymbol{x}-\boldsymbol{x}_i)\mathbb{A}_i))\\&=\textstyle\sum_{i=1}^{N}[\boldsymbol{\nabla}(\boldsymbol{\nabla}\cdot(\psi(\boldsymbol{x}-\boldsymbol{x}_i)\mathbb{A}_i))\\&\quad-\boldsymbol{\nabla}^2(\psi(\boldsymbol{x}-\boldsymbol{x}_i)\mathbb{A}_i)].\end{aligned} \tag{C3}$$

At this point, the N values of $\mathbb{A}_i$ are unknown, but since we are interpolating over N data points, $\boldsymbol{B}_i$, we can set up a system of N equations to solve for the unknowns such that

$$\boldsymbol{B}_j(\boldsymbol{x}_j)=\sum_{i=1}^{N}\boldsymbol{\nabla}\times(\boldsymbol{\nabla}\times(\psi(\boldsymbol{x}_j-\boldsymbol{x}_i)\mathbb{A}_i)). \tag{C4}$$

This ensures the second property of our desired scheme is met, namely $\boldsymbol{B}(\boldsymbol{x}_i)=\boldsymbol{B}_i(\boldsymbol{x}_i)$.

Lastly, because we originally defined the magnetic field as the curl of a vector potential, it will be divergence free by construction, since the divergence of a curl is always zero $\boldsymbol{\nabla}\cdot(\boldsymbol{\nabla}\times\boldsymbol{A})=0$. However, we can check our final scheme as well to verify that our introduction of an addition vector field, $\mathbb{A}$, has not altered this property. Using Equation (C3), we find that

$$\begin{aligned}\boldsymbol{\nabla}\cdot\boldsymbol{B}&=\textstyle\sum_{i=1}^{N}[\boldsymbol{\nabla}\cdot\boldsymbol{\nabla}(\boldsymbol{\nabla}\cdot(\psi(\boldsymbol{x}-\boldsymbol{x}_i)\mathbb{A}_i))\\&\quad-\boldsymbol{\nabla}\cdot(\boldsymbol{\nabla}^2(\psi(\boldsymbol{x}-\boldsymbol{x}_i)\mathbb{A}_i))]\\&=\textstyle\sum_{i=1}^{N}[\boldsymbol{\nabla}^2(\boldsymbol{\nabla}\cdot(\psi(\boldsymbol{x}-\boldsymbol{x}_i)\mathbb{A}_i))\\&\quad-\boldsymbol{\nabla}^2(\boldsymbol{\nabla}\cdot(\psi(\boldsymbol{x}-\boldsymbol{x}_i)\mathbb{A}_i))]=0.\end{aligned} \tag{C5}$$

Therefore, our interpolated magnetic field remains divergence free.

Appendix D
Flux Freezing with Spherical Symmetry

In the case of a spherical expansion of a plasma, the magnetic fields will be "frozen" in the plasma as it expands. If the expansion of the fluid can be determined entirely by the basic (i.e., non-MHD) fluid equations, then it is possible to solve for the magnetic field as the plasma expands. Using the integral definition of magnetic flux, $\mathbb{F}_{\rm mag}=\int\boldsymbol{B}\cdot d\boldsymbol{A}$, the initial and final magnetic fluxes through the surface containing a fluid element will be the same, i.e., $\mathbb{F}_{\rm mag,ini}=\mathbb{F}_{\rm mag,fin}$. Since we are following a particular fluid element, the mass contained within will remain the same as well, i.e., $m_{\rm ini}=m_{\rm fin}$.

Using a spherical coordinate system with the origin at the center of the expansion, we define a fluid element with differential volume of

$$dV=r^2\sin\theta\;dr\;d\theta\;d\phi, \tag{D1}$$

and differential areas of

$$dA_{\rm face}=r^2\sin\theta\;d\theta\;d\phi=r^2d\Omega, \tag{D2}$$

$$dA_{\rm top}=r\sin\theta\;dr\;d\phi, \tag{D3}$$

$$dA_{\rm side}=r\;dr\;d\theta, \tag{D4}$$

with $dA_{\rm face}$ the surface facing the direction of expansion, $dA_{\rm top}$ the upper surface, and $dA_{\rm side}$ one of the side surfaces of the fluid element. The remaining three surfaces of the fluid element have the same areas, but because of Gauss' Law ($\oint\boldsymbol{B}\cdot d\boldsymbol{A}=0$), we focus on three sides only.

As the fluid element moves away from the origin, by spherical symmetry, the angular properties of the fluid element will remain the same such that

$$\begin{aligned}&d\theta_{\rm ini}=d\theta_{\rm fin},\quad d\phi_{\rm ini}=d\phi_{\rm fin},\quad \sin\theta_{\rm ini}=\sin\theta_{\rm fin},\\&\sin\theta_{\rm ini}\,d\theta_{\rm ini}\,d\phi_{\rm ini}=\sin\theta_{\rm fin}\,d\theta_{\rm fin}\,d\phi_{\rm fin}\\&\quad\Rightarrow d\Omega_{\rm ini}=d\Omega_{\rm fin}.\end{aligned} \tag{D5}$$

Additionally, the fluid element will compress and expand, but while its mass will remain constant, its density will change such that

$$\rho_{\rm ini}=\frac{m_{\rm ini}}{r_{\rm ini}^2dr_{\rm ini}d\Omega_{\rm ini}},\qquad \rho_{\rm fin}=\frac{m_{\rm fin}}{r_{\rm fin}^2dr_{\rm fin}d\Omega_{\rm fin}}, \tag{D6}$$

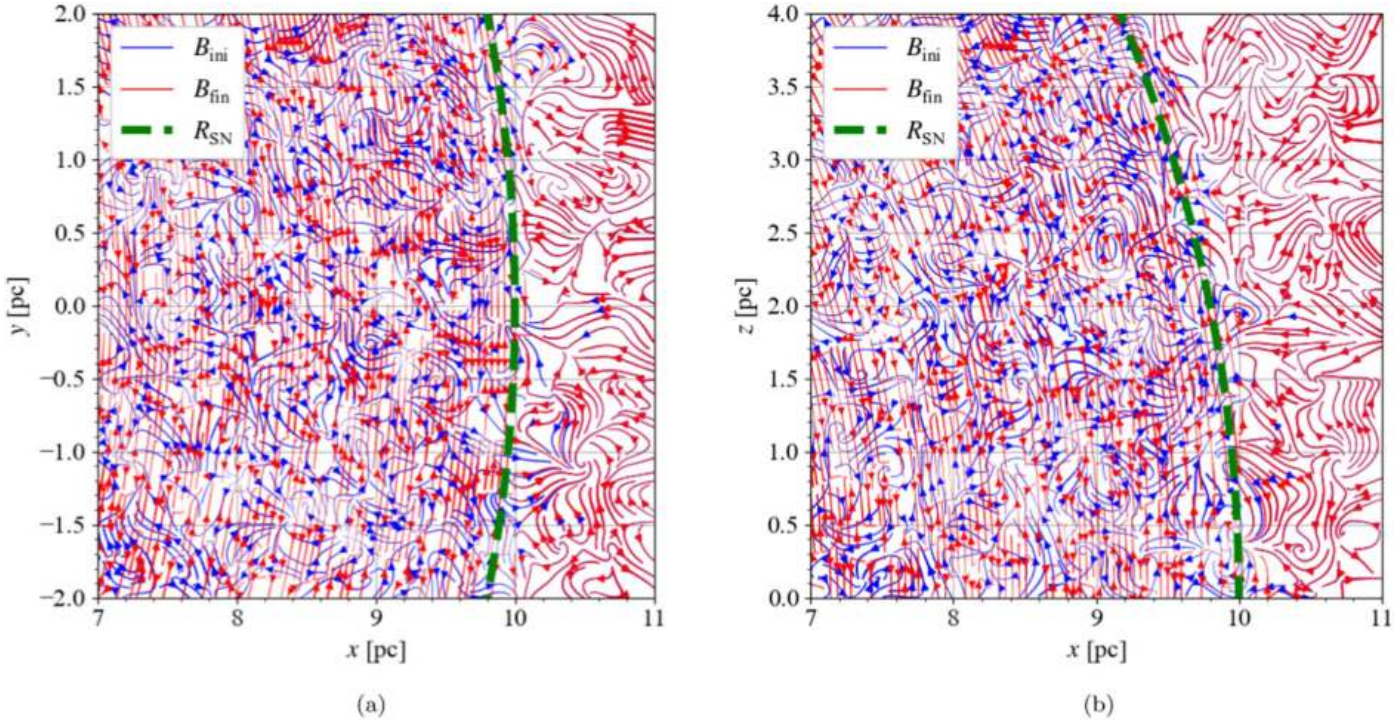

Figure D1. Comparison of initial and final magnetic field conditions after the passage of a shock wave with a generic Sedov profile. The initial magnetic field (shown in blue) is stretched and compressed (red lines) as the shock wave passes through the medium. Here, the spherical shock is centered at the origin and has a radius of 10 pc (dashed green line). Note that the slight variations between the initial and final magnetic fields just ahead of the shock wave are a product of the plotting algorithm, not the calculation.

$$\Rightarrow \rho_{\rm ini} r_{\rm ini}^2 dr_{\rm ini} = \rho_{\rm fin} r_{\rm fin}^2 dr_{\rm fin}$$
$$\Rightarrow \frac{dr_{\rm ini}}{dr_{\rm fin}} = \frac{\rho_{\rm fin} r_{\rm fin}^2}{\rho_{\rm ini} r_{\rm ini}^2}. \quad \text{(D7)}$$

For an infinitesimally small fluid element, the magnetic field will be uniform throughout the entire fluid element, and we can decompose the vector $\boldsymbol{B}$ into a component parallel to the direction of expansion, $\boldsymbol{B}_\parallel$, and a component orthogonal to the direction of expansion, $\boldsymbol{B}_\perp$,

$$\boldsymbol{B}_\perp \equiv \boldsymbol{B} \times \hat{\boldsymbol{r}}, \quad \boldsymbol{B}_\perp \equiv \boldsymbol{B} - (\boldsymbol{B} \cdot \hat{\boldsymbol{r}})\hat{\boldsymbol{r}}, \quad \text{(D8)}$$
$$\boldsymbol{B} = \boldsymbol{B}_\perp + \boldsymbol{B}_\parallel, \quad B^2 = B_\perp^2 + B_\parallel^2. \quad \text{(D9)}$$

With these definitions, we can calculate the flux through each surface as

$$d\mathbb{F}_{\rm mag} = \boldsymbol{B} \cdot d\boldsymbol{A} \quad \text{(D10)}$$
$$\Rightarrow d\mathbb{F}_{\rm mag,face} = B_\parallel r^2 d\Omega$$
$$\Rightarrow B_{\parallel,\rm ini} r_{\rm ini}^2 d\Omega_{\rm ini} = B_{\parallel,\rm fin} r_{\rm fin}^2 d\Omega_{\rm fin}$$
$$B_{\parallel,\rm fin} = B_{\parallel,\rm ini}\left(\frac{r_{\rm ini}}{r_{\rm fin}}\right)^2. \quad \text{(D11)}$$

Defining α as the angle between the normal of the top surface and $\boldsymbol{B}_\perp$, we have

$$d\mathbb{F}_{\rm mag,top} = B_\perp \cos\alpha \;\; r \sin\theta \;\; dr \;\; d\phi$$
$$\Rightarrow B_{\perp,\rm ini} \cos\alpha_{\rm ini} \;\; r_{\rm ini} \sin\theta_{\rm ini} \;\; dr_{\rm ini} \;\; d\phi_{\rm ini}$$
$$= B_{\perp,\rm fin} \cos\alpha_{\rm fin} \;\; r_{\rm fin} \sin\theta_{\rm fin} \;\; dr_{\rm fin} \;\; d\phi_{\rm fin}$$
$$\Rightarrow B_{\perp,\rm fin} = B_{\perp,\rm ini}\left(\frac{\cos\alpha_{\rm ini}}{\cos\alpha_{\rm fin}}\right)\left(\frac{r_{\rm ini}}{r_{\rm fin}}\right)\left(\frac{dr_{\rm ini}}{dr_{\rm fin}}\right).$$

Using Equation (D7), we have

$$B_{\perp,\rm fin} = B_{\perp,\rm ini}\left(\frac{\cos\alpha_{\rm ini}}{\cos\alpha_{\rm fin}}\right)\left(\frac{r_{\rm ini}}{r_{\rm fin}}\right)\left(\frac{\rho_{\rm fin} r_{\rm fin}^2}{\rho_{\rm ini} r_{\rm ini}^2}\right) \quad \text{(D12)}$$
$$\Rightarrow B_{\perp,\rm fin} = B_{\perp,\rm ini}\left(\frac{\cos\alpha_{\rm ini}}{\cos\alpha_{\rm fin}}\right)\left(\frac{\rho_{\rm fin} r_{\rm fin}}{\rho_{\rm ini} r_{\rm ini}}\right) \quad \text{(D13)}$$

$$d\mathbb{F}_{\rm mag,side} = B_\perp \sin\alpha r \sin\theta \; dr \; d\phi$$
$$\Rightarrow B_{\perp,\rm ini} \sin\alpha_{\rm ini} r_{\rm ini} \sin\theta_{\rm ini} \; dr_{\rm ini} \; d\phi_{\rm ini}$$
$$= B_{\perp,\rm fin} \sin\alpha_{\rm fin} r_{\rm fin} \sin\theta_{\rm fin} \; dr_{\rm fin} \; d\phi_{\rm fin}$$
$$\Rightarrow B_{\perp,\rm fin} = B_{\perp,\rm ini}\left(\frac{\sin\alpha_{\rm ini}}{\sin\alpha_{\rm fin}}\right)\left(\frac{r_{\rm ini}}{r_{\rm fin}}\right)\left(\frac{dr_{\rm ini}}{dr_{\rm fin}}\right). \quad \text{(D14)}$$

Using Equation (D7), we have

$$B_{\perp,\rm fin} = B_{\perp,\rm ini}\left(\frac{\sin\alpha_{\rm ini}}{\sin\alpha_{\rm fin}}\right)\left(\frac{r_{\rm ini}}{r_{\rm fin}}\right)\left(\frac{\rho_{\rm fin} r_{\rm fin}^2}{\rho_{\rm ini} r_{\rm ini}^2}\right) \quad \text{(D15)}$$
$$\Rightarrow B_{\perp,\rm fin} = B_{\perp,\rm ini}\left(\frac{\sin\alpha_{\rm ini}}{\sin\alpha_{\rm fin}}\right)\left(\frac{\rho_{\rm fin} r_{\rm fin}}{\rho_{\rm ini} r_{\rm ini}}\right). \quad \text{(D16)}$$

In order for both Equations (D13) and (D16) to be true, we must have

$$\Rightarrow \frac{\cos\alpha_{\rm ini}}{\cos\alpha_{\rm fin}} = \frac{\sin\alpha_{\rm ini}}{\sin\alpha_{\rm fin}} = 1 \quad \text{(D17)}$$
$$\Rightarrow B_{\perp,\rm fin} = B_{\perp,\rm ini}\left(\frac{\rho_{\rm fin} r_{\rm fin}}{\rho_{\rm ini} r_{\rm ini}}\right). \quad \text{(D18)}$$

Combining Equations (D11) and (D18) gives a means of relating initial conditions and final densities to the final

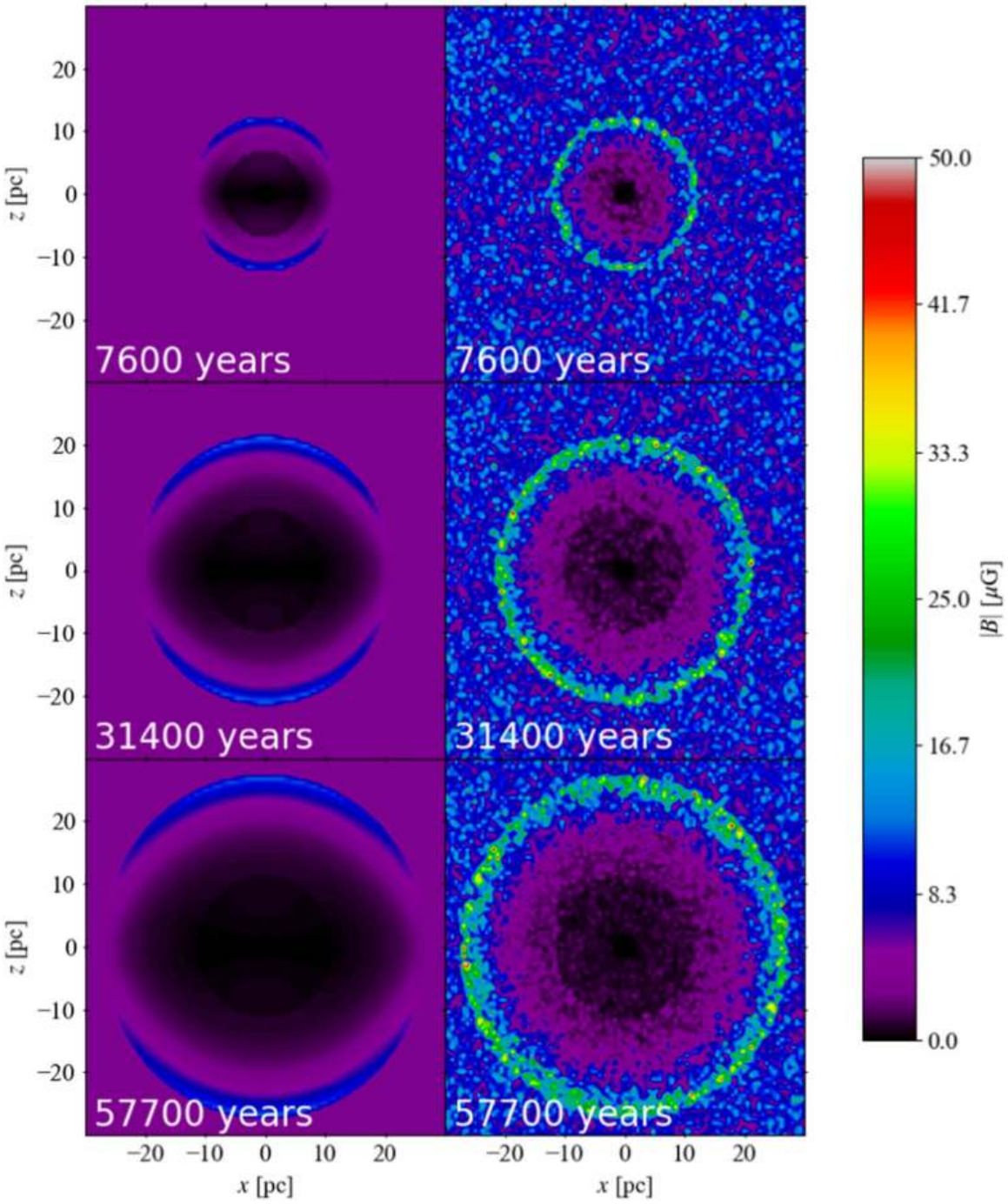

Figure D2. Outputs from magnetic field model for comparison to Figure 1 of Balsara et al. (2001). The left column shows the uniform magnetic field case; the right column shows the turbulent magnetic field case. The output times are at 7600, 31,400, and 57,700 yr for the top, middle, and bottom row panels, respectively.

magnetic field. An example of the flux-freezing transformation is shown in Figure D1.

To check the reasonableness of our approach, we compared our method to a 3D, full-MHD simulation of the magnetic field. Balsara et al. (2001) carried out three-dimensional MHD simulations of SNe occurring in a uniform and turbulent, magnetized ISM. Using the same initial conditions as Balsara et al. (2001; namely, $n_{\rm ISM} = 1\,{\rm cm}^{-3}$, $T_{\rm ISM} = 8000\,{\rm K}$, $M_{\rm ej} = 5\,M_{\odot}$, $E_{\rm SN} = 10^{51}$ erg, $\langle |\boldsymbol{B}_{\rm ISM}| \rangle = 3.57\,\mu{\rm G}$ and $\sqrt{\langle B_{\rm ISM}^2 \rangle} = 8.94\,\mu{\rm G}$ with a Kolmogorov spectrum), we compared our results to Balsara et al. (2001); see Figure D2 and compare to Figure 1 of Balsara et al. (2001). At the final time step, $t = 57{,}700$ yr, our SN model results (in comparison with Balsara et al.) are: $R_{\rm SN} = 27\,{\rm pc}$ (25.5 pc), $T_{\rm SN} = 7.2 \times 10^5\,{\rm K}$ ($4.2 \times 10^5\,{\rm K}$), $v_{\rm SN} = 133\,{\rm km\,s^{-1}}$ ($174\,{\rm km\,s^{-1}}$), $P_{\rm SN} = 3.7 \times 10^{-10}\,{\rm dyn\,cm^{-2}}$ ($5.2 \times 10^{-10}\,{\rm dyn\,cm^{-2}}$), $\rho_{\rm SN} = 3.3\rho_{\rm ISM}$ ($3.3\rho_{\rm ISM}$), and $B_{\rm postshock} = 3B_{\rm preshock}$ ($2.4B_{\rm preshock}$; although Balsara et al. notes the expected value is $3.3B_{\rm preshock}$). Balsara et al. noted their resolution prevented them from getting the full magnetic compressional effect. Given the qualitative and fairly close quantitative agreement between our hydrodynamic/magnetic field approach and the 3D, full-MHD approach used by Balsara et al. (2001), we expect our approach to

be a sufficiently good approximation of 3D MHD for the time period we examine.

Appendix E
Grain Charging: Processes

As grains move within the SNR, they will acquire/lose electrons and ions due to impacts with the plasma or photons. Several processes can influence the total charge of the grain; so the total charging rate, $dq_{\rm gr}/dt$, is

$$\frac{dq_{\rm gr}}{dt} = \sum_i \mathcal{I}_i, \tag{E1}$$

which is summed over i processes of currents, $\mathcal{I}_j$. These currents are due to impinging plasma particles, $\mathcal{I}_{\rm imp}$, and the associated secondary electrons emitted, $\mathcal{I}_{\rm see}$, transmitted plasma particles, $\mathcal{I}_{\rm trans}$, and photoelectron emission, $\mathcal{I}_\gamma$. The following derivations are the same as those used by Kimura & Mann (1998).

E.1. Impinging Ions/Electrons

Charging by impinging plasma particles is caused by incident ions/electrons, j, impacting the surface of the grain, sticking, and altering the grain charge. It is given by Dwek & Arendt (1992) as

$$\mathcal{I}_{\rm imp} = 2\pi e \sum_j \left\{ Z_j \int_{v_{\rm A}}^{\infty} dv_T \times \int_0^{\pi} d\theta\, C_{{\rm coll},j}(v_T) f_j(v_T, \theta) v_T^3 \sin\theta \right\}, \tag{E2}$$

where v_T is the thermal velocity of the plasma. The minimum impinging velocity, $v_{\rm A}$, is given by

$$v_{\rm A} = \begin{cases} 0 & Z_j \Phi_j \leqslant 0, \\ (2 Z_j e U_{\rm gr}/m_j)^{1/2} & Z_j \Phi_j > 0, \end{cases} \tag{E3}$$

with the collisional cross section, $C_{{\rm coll},j}(v_T)$, given by

$$C_{{\rm coll},j}(v_T) = \pi a_{\rm gr}^2 \left(1 - \frac{2 Z_j e U_{\rm gr}}{m_j v_T^2}\right). \tag{E4}$$

Because the dust grains will potentially have large relative velocities to the plasma, as well as large thermal velocities, we assume a Maxwellian velocity distribution, $f_j(v_T, \theta)$,

$$f_j(v_T, \theta) = n_j \left(\frac{m_j}{2\pi k_{\rm B} T}\right)^{3/2} \times \exp\left[-\frac{m_j}{2 k_{\rm B} T}(v_T^2 + v_{\rm rel}^2 - 2 v_T v_{\rm rel} \cos\theta)\right], \tag{E5}$$

where θ is the angle between the thermal and relative velocities.

E.2. Secondary Electron Emission

If the impinging plasma particles have sufficient initial energy, $E_{\rm ini} = 2 k_{\rm B} T + \frac{1}{2} m_j v_{\rm rel}^2 + Z_j e U_{\rm gr}$ (Draine & Salpeter 1979; McKee et al. 1987; Kimura & Mann 1998), then after initially ejecting an electron, there is sufficient energy to eject additional electrons. In this situation, the current of secondary electrons, $\mathcal{I}_{\rm see}$, is

$$\mathcal{I}_{\rm see} = 2\pi e \sum_j \left\{ \delta_j(E_{\rm ini}) \int_{E_{\rm min}}^{\infty} dE \varrho_j(E) \times \int_{v_{\rm A}}^{\infty} dv_T \int_0^{\pi} d\theta\, C_{{\rm coll},j}(v_T) f_j(v_T, \theta) v_T^3 \sin\theta \right\}, \tag{E6}$$

where the minimum required energy is $E_{\rm min} = \max[0, eU_{\rm gr}]$. The type and energy of impacting plasma particles will determine the effectiveness of secondary emission, so the secondary electron yield, $\delta_j(E_{\rm ini})$, is given for electrons by Draine & Salpeter (1979)

$$\delta_e(E_{\rm ini}) = \delta_{\rm max} \frac{8(E_{\rm ini}/E_{\rm max})}{(1 + E_{\rm ini}/E_{\rm max})^2} \left(1 - \exp\left[-\frac{4 a_{\rm gr}}{3\lambda_{\rm esc}}\right]\right) \times f_1\left(\frac{4 a_{\rm gr}}{3R}\right) f_2\left(\frac{a_{\rm gr}}{\lambda_{\rm esc}}\right), \tag{E7}$$

where the fitting functions, f_1 and f_2, are given by

$$f_1(\chi) = \frac{1.6 + 1.4\chi^2 + 0.54\chi^4}{1 + 0.54\chi^4}, \tag{E8}$$

$$f_2(\chi) = \frac{1 + 2\chi^2 + \chi^4}{1 + \chi^4}, \tag{E9}$$

and the escape length for electrons, $\lambda_{\rm esc}$, is

$$\lambda_{\rm esc} = R_e(E_{\rm max})/R_m(\pounds_e)^{\pounds_e}, \tag{E10}$$

where the value of R_m is given for various materials in Table E1. The maximum yields from a bulk solid, $\delta_{\rm max}$, at energy, $E_{\rm max}$, are assumed to be 1.3 and 400 eV, respectively (Lide 2008). The secondary yield for ions is given by the empirical formula in Draine & Salpeter (1979),

$$\delta_{\rm ion}(E_{\rm ini}) = 0.1 Z_j^2 \frac{1 + (m_H/m_j)(E_{\rm ini}/E_1)}{[1 + (m_H/m_j)(E_{\rm ini}/E_2)]^2} \times \begin{cases} 1 & U_{\rm gr} \leqslant 0, \\ 1 + \left(\dfrac{U_{\rm gr}}{1{\rm V}}\right) & U > 0, \end{cases} \tag{E11}$$

where $E_1 = 500$ eV and $E_2 = 35$ keV.

Lastly, the energy distributions ϱ_j for secondary electrons emitted by electrons and ions are given by

$$\varrho_e(E) = \frac{E}{2E_e^2}\left[1 + \frac{1}{2}\left(\frac{E}{E_e}\right)^2\right]^{-3/2}, \tag{E12}$$

Table E1
Summary of Sputtering Yield and Escape Length ($\lambda_{\rm esc}$) Parameters

Dust Species	$E_{\rm bind}$ (eV)	$Z_{\rm target}$	$m_{\rm target}$ ($m_{\rm u}$)	κ	$\pounds_e$	$R_m(\pounds_e)$
Fe	4.31	26	56	0.23	1.5662	1.1891

Note. Values are from Nozawa et al. (2006, and references therein). Electron stopping ranges are based on outputs from the CASINO software (Drouin et al. 2007).

Table E2
Stopping Ranges for Various Particles onto Iron

$$R_{\text{incident}\rightarrow\text{target}} = \mathbb{R}\left(\frac{E}{1\text{ keV}}\right)^{\beta}$$

Incident[a,b]	Target	$\mathbb{R}$ (nm)	β
e^-	Fe	5.1457	1.5662
H	Fe	7.8944	0.9667
He	Fe	4.6270	0.9490
C	Fe	2.2539	0.8049
N	Fe	2.0788	0.7794
O	Fe	1.9576	0.7627
Ne	Fe	1.7949	0.7360
Mg	Fe	1.6854	0.7061
Si	Fe	1.5552	0.6753
S	Fe	1.5055	0.6499
Ca	Fe	1.4367	0.6139
Fe	Fe	1.4116	0.5679
Ni	Fe	1.4014	0.5609
Zn	Fe	1.4128	0.5413
Kr	Fe	1.4238	0.5076

Notes.
[a] Electron stopping ranges are based on outputs from the CASINO software (Drouin et al. 2007).
[b] Ion stopping ranges are based on outputs from the SRIM software (Ziegler & Biersack 1985; Ziegler et al. 2010).

$$\varrho_{\text{ion}}(E) = \frac{1}{E_{\text{ion}}}\left[1 + \frac{1}{2}\left(\frac{E}{E_{\text{ion}}}\right)^2\right]^{-2}, \tag{E13}$$

where the most probable energies are $E_e = 2\,\text{eV}$ and $E_{\text{ion}} = 1\,\text{eV}$.

E.3. Transmission of Ions/Electrons

The transmission (also referred to as tunneling; Chow et al. 1993) current of ions/electrons, $\mathcal{I}_{\text{tran}}$, accounts for the plasma particles with sufficient velocity to penetrate completely through the grain without being captured such that

$$\mathcal{I}_{\text{tran}} = -2\pi e \sum_j \left\{ Z_j \int_{v_{\text{B}}}^{\infty} dv_T \times \int_0^{\pi} d\theta\, C_{\text{coll},j}(v_T) f_j(v_T, \theta) v_T^3 \sin\theta \right\}, \tag{E14}$$

where the minimum velocity, v_{B}, required to pass through the grain is (Draine & Salpeter 1979; McKee et al. 1987; Kimura & Mann 1998)

$$v_{\text{B}} = \begin{cases} \sqrt{\dfrac{\left(2k_{\text{B}}T + \frac{1}{2}m_j v_{\text{rel}}^2\right)\omega_j}{m_j}} & Z_j\Phi_j \leqslant 0, \\ \sqrt{\dfrac{\left(2k_{\text{B}}T + \frac{1}{2}m_j v_{\text{rel}}^2\right)(\omega_j + Z_j\Phi_j)}{m_j}} & Z_j\Phi_j > 0. \end{cases} \tag{E15}$$

From Draine & Salpeter (1979), the energy, $\left(k_{\text{B}}T + \frac{1}{2}m_j v_{\text{rel}}^2\right)\omega_j$, required to penetrate a grain is given by

$$\left(k_{\text{B}}T + \frac{1}{2}m_j v_{\text{rel}}^2\right)\omega_j = \begin{cases} \Delta_j & Z_j < 0, \\ \Delta_j + E_{\text{Bohr}} & Z_j > 0. \end{cases} \tag{E16}$$

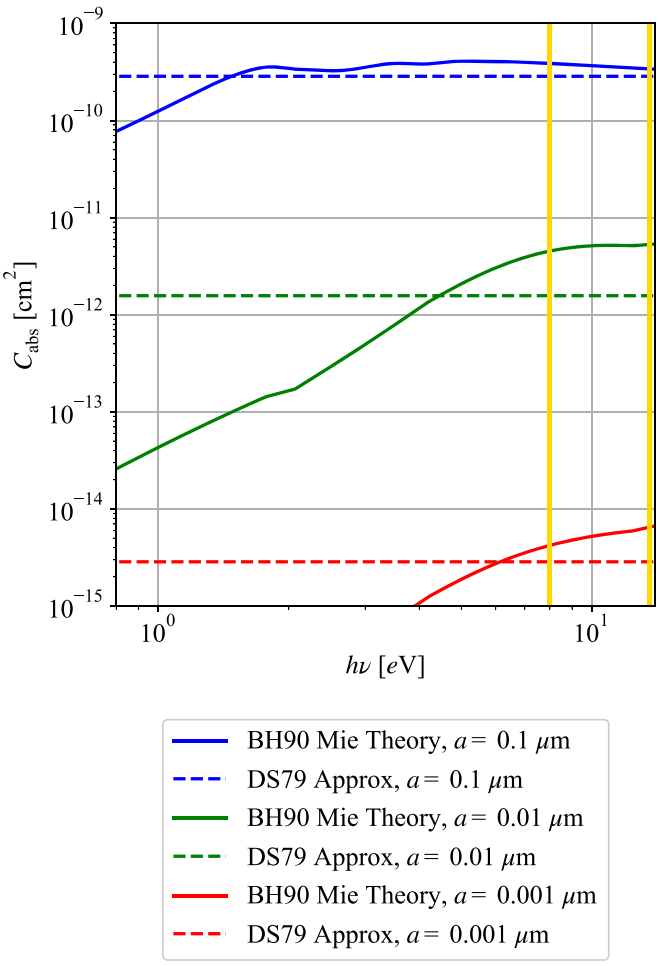

Figure E1. Comparison of absorption cross section, C_{abs}, calculations. The C_{abs} calculated using Mie theory is shown with solid lines, and the approximation used by Draine & Salpeter (1979) is shown with dashed lines. For the energy range appropriate for the photoelectron emission (~8–13.6 eV, shown with yellow, vertical lines), the approximation provides a reasonable approximation with far fewer calculations.

Additionally, we assume that the ions emerge neutral because of recombination if their energy is below the Bohr Energy, $E_{\text{Bohr}} = (m_j/m_e)\,E_H$ with $E_H = 13.6\,\text{eV}$.

The penetration threshold energy, Δ_j, is found using an energy-range relation and the size of the dust grain (Fitting 1974)

$$R_j(\Delta_j) \equiv 4a_{\text{gr}}/3. \tag{E17}$$

The energy-range relation is based on measured stopping ranges for various particles into materials, and we used outputs from the SRIM software (Ziegler & Biersack 1985; Ziegler et al. 2010) and the CASINO software (Drouin et al. 2007) for ion and electron stopping in materials, respectively, and fit power-law profiles to the results in the form

$$R_j(E) = \mathbb{R}_j E^{\beta_j}. \tag{E18}$$

A compilation of the fit values is listed in Table E2.

E.4. Photoelectron Emission

The dust grains will be exposed to UV photons, and, depending on the grain material, electrons will be emitted from the surface of the grain. The photoelectric current, $\mathcal{I}_\gamma$, then is

given by

$$\mathcal{I}_\gamma = e\int_{W+E_{\min}}^{\infty} d(h\nu)\,C_{\rm abs}(h\nu)\,\mathbb{F}_{\gamma,h\nu}(h\nu)\,Y_\gamma(h\nu) \times \int_{E_{\min}}^{E_{\max}} dE\,\varrho_\gamma(E), \tag{E19}$$

where $E_{\max} = h\nu - W$, h is Planck's constant, ν is the photon frequency, and W is the work function required to emit an electron. Following the example of Kimura & Mann (1998), we set $E_{\rm work} = W$. The photoelectric yield, $Y_\gamma(h\nu)$, is the number of electrons emitted per absorbed photon (Draine & Salpeter 1979) such that

$$Y_\gamma(h\nu) = \frac{(h\nu - E_{\rm work} + E_{\rm low})^2 - E_{\rm low}^2}{(h\nu)^2 - E_{\rm low}^2} \times \left[1 - \left(1 - \frac{\lambda_{\rm esc}}{a_{\rm gr}}\right)^3\right], \tag{E20}$$

where $E_{\rm work} = 8$ eV and $E_{\rm low} = 6$ eV. The energy distribution, $\varrho_\gamma(E)$, of photoelectrons (Grard 1973) is

$$\varrho_\gamma(E) = \frac{E}{E_\gamma^2}\exp\left[-\frac{E}{E_\gamma}\right], \tag{E21}$$

where $E_\gamma = 1$ eV.

Because the SNR is expected in our study to be non-radiative, we assume that the spectral photon flux, $\mathbb{F}_{\gamma,h\nu}(h\nu)$, is a blackbody at temperature, T, at the location of the grain inside the SNR (with a dilution factor, $\mathbb{D} = 10^{-22}$; Draine & Salpeter 1979) such that

$$\mathbb{F}_{\gamma,h\nu}(h\nu) = \frac{2\pi\nu^2}{hc^2}\left(\frac{1}{\exp\left[\frac{h\nu}{k_{\rm B}T}\right] - 1}\right)\mathbb{D}, \tag{E22}$$

or the average interstellar background (see, e.g., Draine 2011) outside the SNR. Additionally, the absorption cross section of the grain, $C_{\rm abs}(h\nu)$, is dependent on the photon energy, grain size, and complex index of refraction. The complex indices of refraction for iron from Pollack et al. (1994) were used and $C_{\rm abs}(h\nu)$ was calculated using Mie theory and the procedure from Bohren & Huffman (1983). However, this method is extremely calculation-intensive, and in order to simplify calculations, the $C_{\rm abs}(h\nu)$ approximation given by Draine & Salpeter (1979) was used,

$$C_{\rm abs}(h\nu) = \frac{\pi a_{\rm gr}^3}{a_{\rm gr} + 0.01\ \mu{\rm m}}. \tag{E23}$$

This approximation shows good agreement with calculation using Mie theory for iron within the region in which we are interested. Comparisons for various grain sizes are shown in Figure E1.

Appendix F
Grain Charging: Analytic Description

Within the SNR, the grain charge transitions through a range of values depending on the dominant charging process. Figure F1 shows the results for selected values and the analytic fitting function, which takes the form

$$\begin{aligned}\Phi = {} & [\Phi_{\rm imp}(1 - \Psi_{\rm B}) + \Phi_{\rm stationary} + \Phi_{\rm see1}\Psi_{\rm B} \\ & + \Phi_{\rm see2}\Psi_{\rm B}\Psi_{\rm C}]\Psi_{\rm A}\Psi_{\rm F}(1 - \Psi_{\rm D}) \\ & + \Phi_{\rm tran}\Psi_{\rm D}\Psi_{\rm E} + \Phi_{\rm thermal}\Psi_{\rm B}(1 - \Psi_{\rm D})(1 - \Psi_{\rm F}),\end{aligned} \tag{F1}$$

where the "Φ" quantities represent the corresponding charging regime, and the "Ψ" quantities are scaling functions that scale and transition between the different charging regimes.

At temperatures where the thermal velocity is much smaller than the relative velocity ($v_T \ll v_{\rm rel}$), the side of the grain that is opposite from the relative motion is effectively shielded from impacting electrons/ions. Additionally, because the relative velocity dominates, the electrons and ions will impact the grain at similar frequencies; this results in a nearly neutral grain charge (e.g., for $v_{\rm rel} = 10^{1.5}\,{\rm km\,s^{-1}}$, this occurs for $T < 3\times10^3$ K; see Figure F1).

As the thermal velocity approaches the relative velocity ($v_T \lesssim v_{\rm rel}$), the frequency of impinging electrons will dominate over impinging ions, driving the grain charge negative,

$$\Phi_{\rm imp} = -0.084 + 1.112\times10^{-3}v_7^2 + \left(\frac{T_{\rm rel}}{T_5}\right)^{0.75}, \tag{F2}$$

$$\Psi_{\rm A} = \frac{T_5^{\Theta_{\rm A}}}{T_{\rm imp}^{\Theta_{\rm A}} + T_5^{\Theta_{\rm A}}} \times \max\left[0, \frac{T_{\rm tran} - T_{\rm imp}}{|T_{\rm tran} - T_{\rm imp}|}\right], \tag{F3}$$

with

$$\begin{aligned} v_7 &= \left(\frac{v_{\rm rel}}{10^7\ {\rm cm\ s^{-1}}}\right), \\ T_5 &= \left(\frac{T}{10^5\ {\rm K}}\right), \\ T_{\rm rel} &= 0.2506\ v_7^2, \\ T_{\rm imp} &= 0.3433\ v_7^2, \\ T_{\rm tran} &= \frac{10.57}{1 - \exp\left[-\left(\frac{\lambda_{\rm esc}}{a_{\rm gr}}\right)^{0.75}\right]}, \\ \Theta_{\rm A} &= 36.99, \end{aligned}$$

(e.g., for $v_{\rm rel} = 10^{1.5}\,{\rm km\,s^{-1}} \triangleq T \approx 3\times10^3$ K).

When the thermal velocity is about the same value as the relative velocity ($v_T \approx v_{\rm rel}$), the grain charge will approach (but not reach in this case because of the inclusion of additional charging processes) its stationary value, $\Phi_{\rm stationary}$ (Spitzer 1941),

$$\exp\left[\Phi_{\rm stationary}\right] = \sqrt{\frac{m_e}{m_{\rm ion}}}(1 - \Phi_{\rm stationary}). \tag{F4}$$

In solving for the steady-state values, we chose an approximate composition of the ECSN ejecta: $n_{\rm H} \approx 0.01\,{\rm cm^{-3}}$, $n_{\rm He} \approx 1\,{\rm cm^{-3}}$, $n_{\rm Fe} \approx 0.6\,{\rm cm^{-3}}$, and $n_{\rm Ni} \approx 0.4\,{\rm cm^{-3}}$. For this composition, since He is much more numerous than H, and He is much more mobile compared to the Fe and Ni atoms, the plasma will behave similar to a pure-He environment, so $m_{\rm ion} \approx 4\ m_{\rm u}$, at least with respect to grain charging, and $\Phi_{\rm stationary} \approx -3.049$ (e.g., for $v_{\rm rel} = 10^{1.5}\,{\rm km\,s^{-1}} \triangleq T \in (3\times10^3, 3\times10^4)$ K).

At higher thermal velocities, secondary electron emission will begin to dominate ($v_T \gtrsim v_{\rm rel}$), increasing the grain charge

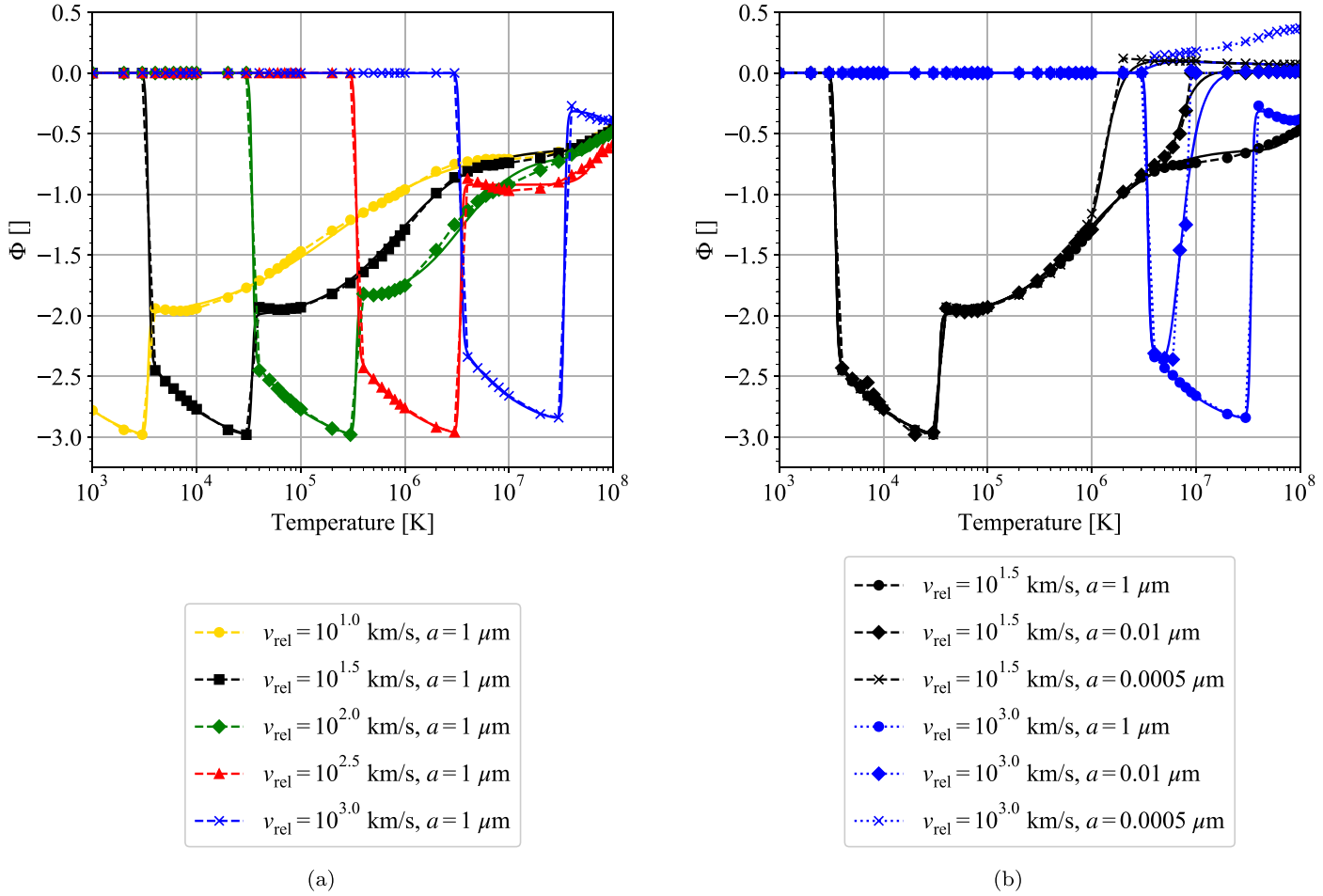

Figure F1. Sample potential parameters, Φ, within the SNR for Fe grains. Panel (a) shows the potential parameter for a 1 μm grain at various relative velocities, and panel (b) shows the potential parameter for various grain sizes. In both panels, the numerically solved values (not including field emission) are shown with data marks and dashed–dotted lines, while the analytical fit is shown with solid lines.

such that

$$\Phi_{see1} = 1.740(1 - \exp[-0.1037\, v_7^2]) + 1.005, \quad \text{(F5)}$$

$$\Phi_{see2} = \max[0, -0.2267\, v_7^2 + 1.430], \quad \text{(F6)}$$

$$\Psi_B = \frac{T_5^{\Theta_B}}{T_{see1}^{\Theta_B} + T_5^{\Theta_B}}, \quad \text{(F7)}$$

$$\Psi_C = \frac{T_5^{\Theta_C}}{T_{see2}^{\Theta_C} + T_5^{\Theta_C}}, \quad \text{(F8)}$$

with

$$T_{see1} = 3.404\ v_7^2,$$
$$T_{see2} = 34.82\ v_7^{1.223},$$
$$\Theta_B = 38.48,$$
$$\Theta_C = 0.3545 \ln[v_7] + 1.563,$$

(e.g., for $v_{rel} = 10^{1.5}$ km s^{-1} $\hat{=}$ $T \in (3 \times 10^4, 10^6)$ K).

Near $T = 10^6$ K, the transmission/tunneling current will become important, further increasing the grain charge as

$$\Phi_{tran} = 0.1953 T_5^{-0.162}, \quad \text{(F9)}$$

$$\Psi_D = \exp\left[-\left(\frac{T_{cr}}{T_5}\right)^4\right], \quad \text{(F10)}$$

$$\Psi_E = \exp\left[-10^{-4}\left(\frac{a_{gr}}{\lambda_{esc}}\right)^4\right], \quad \text{(F11)}$$

with

$$T_{cr} = \max[T_{tran}, T_{imp}],$$

(e.g., for $v_{rel} = 10^{1.5}$ km s^{-1} $\hat{=}$ $T \in (10^6, 3 \times 10^7)$ K).

At higher temperatures, the electrons and ions will again impact the grain at relatively similar frequencies, resulting in a relatively neutral grain charge,

$$\Phi_{thermal} = 0.1862 \ln[T_5] - 1.756, \quad \text{(F12)}$$

$$\Psi_F = \exp\left[-\left(\frac{T_5}{T_{thermal}}\right)^4\right], \quad \text{(F13)}$$

with

$$T_{thermal} = \max[703.8, 9.964\, v_7^2], \quad \text{(F14)}$$

(e.g., for $v_{rel} = 10^{1.5}$ km s^{-1} $\hat{=}$ $T > 3 \times 10^7$ K).

Within the SNR, because of the extremely small dilution factor ($\mathbb{D} = 10^{-22}$, Equation (E22)), photoelectron emission plays almost no role in grain charging. However, outside the SNR, it becomes the dominant process, driving the grain potential to $U_{gr} = 5.6$ V, since it will be in interstellar space and subject to the ISRF (Draine & Salpeter 1979; Draine 2011).

Lastly, we also establish potential limits to account for field emission (McKee et al. 1987),

$$\Phi_{\rm min} \leqslant \Phi \leqslant \Phi_{\rm max},$$

with

$$\Phi_{\rm min} = -11.6\left(\frac{a_{\rm gr}}{0.1\ \mu{\rm m}}\right)\left(\frac{10^5\ {\rm K}}{T}\right),$$
$$\Phi_{\rm max} = 348\left(\frac{a_{\rm gr}}{0.1\ \mu{\rm m}}\right)\left(\frac{10^5\ {\rm K}}{T}\right). \quad \text{(F15)}$$

This completes our description of the grain charge so that

$$U_{\rm gr}(r) = \begin{cases} \Phi k_{\rm B}T/e & r \leqslant R_{\rm SN}, \\ 5.6\ {\rm V} & r > R_{\rm SN}. \end{cases} \quad \text{(F16)}$$

Appendix G
Grain Dynamics

The combined drag of both collisional and Coulomb sources is given by Draine & Salpeter (1979) and Draine (2011) as

$$F_{\rm drag} = 2\pi a_{\rm gr}^2 k_{\rm B}T \times \left\{\sum_j n_j[G_0(s_j) + Z_j^2\Phi^2\ln[\Lambda/Z_j]G_2(s_j)]\right\}, \quad \text{(G1)}$$

where

$$G_0(s) \equiv \left(s^2 + 1 - \frac{1}{4s^2}\right){\rm erf}\ [s] + \frac{1}{\sqrt{\pi}}\left(s + \frac{1}{2s}\right)\exp[-s^2], \quad \text{(G2)}$$

$$G_2(s) \equiv \frac{{\rm erf}\ [s]}{s^2} - \frac{2}{s\sqrt{\pi}}\exp[-s^2], \quad \text{(G3)}$$

$$\Phi \equiv \frac{eU_{\rm gr}}{k_{\rm B}T}, \quad \text{(G4)}$$

$$s_j \equiv \left(\frac{m_j v_{\rm rel}^2}{2k_{\rm B}T}\right)^{1/2}, \quad \text{(G5)}$$

$$\Lambda \equiv \frac{3}{2a_{\rm gr}e|\Phi|}\left(\frac{k_{\rm B}T}{\pi n_e}\right)^{1/2}, \quad \text{(G6)}$$

$${\rm erf}\ [\chi] \equiv \frac{2}{\sqrt{\pi}}\int_0^\chi \exp[-\Upsilon^2]d\Upsilon, \quad \text{(G7)}$$

where we use cgs/esu units. The $G_0(s)$ term accounts for collisional drag, and the $G_2(s)$ term accounts for Coulomb drag. Approximations exist for both, but we used the exact forms given here for completeness. The drag force is summed over all plasma species, j, within the plasma (e.g., p^+, e^-, α, C, etc.), each with number density n_j. The velocity parameter, s, depends on the relative velocity between the grain and plasma, $v_{\rm rel}$, mass of the impacting plasma particle, m_j, and the temperature of the plasma, T (we assume all constituents are at the same temperature, i.e., $T_j = T\ \forall\ j$). Similarly, the potential parameter, Φ, depends on the electric potential of the grain, $U_{\rm gr} = q_{\rm gr}/a_{\rm gr}$, where $q_{\rm gr}$ is the charge of the grain. The charge number of the plasma particle is Z_j, $k_{\rm B}$ is the Boltzmann constant, and e is the elementary charge.

Appendix H
Grain Sputtering

The erosion rate due to sputtering (both kinetic and thermal) is given by Dwek & Arendt (1992), and we use the approach by Nozawa et al. (2006) and Biscaro & Cherchneff (2016), given as

$$\frac{da_{\rm gr}}{dt} = -\frac{m_{\rm sp}}{4\rho_{\rm gr}}\sum_j \frac{n_j}{s_j}\left(\frac{8k_{\rm B}T}{\pi m_j}\right)^{1/2}\exp[-s_j^2] \times \int d\epsilon_j \sqrt{\epsilon_j}\exp[-\epsilon_j]\sinh(2s_j\sqrt{\epsilon_j})Y_j^0(\epsilon_j), \quad \text{(H1)}$$

where $m_{\rm sp}$ is the mass of the sputtered atom (i.e., the average atomic mass for the dust composition, $m_{\rm sp,Fe} = 56m_{\rm u}$), and $\rho_{\rm gr}$ is the density of the dust grain. Additionally, the angle-averaged sputtering yield given by $\langle Y_j(E_j)\rangle_\theta = 2Y_j^0(E_j)$ (Draine & Salpeter 1979), and the backward sputtering yield at normal incidence, $Y_j^0(E)$, is given by Bohdansky (1984)

$$Y_j^0(\epsilon_j) = 160\ \frac{\rm atoms}{\rm ion}\left(\frac{S_j(E)}{1{\rm erg\ cm}^2}\right)\left(\frac{4.31\ {\rm eV}}{E_{\rm bind}}\right) \times \left(\frac{\xi_j(\zeta_j)}{\kappa\zeta_j + 1}\right)\left(1 - \left(\frac{E_{\rm th}}{E}\right)^{2/3}\right) \times \left(1 - \left(\frac{E_{\rm th}}{E}\right)\right)^2, \quad \text{(H2)}$$

where κ is a free parameter that is adjusted to fit experimental data, $E_{\rm bind}$ is the surface binding energy (see Table E1), and $\zeta_j = m_{\rm target}/m_j$ is the ratio of the target atom mass, $m_{\rm target}$, to the incident atom mass, m_j. The threshold energy, $E_{\rm th}$, to induce sputtering is given by Andersen & Bay (1981) and Bohdansky (1984) as

$$E_{\rm th} = \begin{cases} \dfrac{E_{\rm bind}}{g_j(1 - g_j)} & \text{for } m_j/m_{\rm target} \leqslant 0.3, \\ 8E_{\rm bind}\left(\dfrac{m_j}{m_{\rm target}}\right)^{1/3} & \text{for } m_j/m_{\rm target} > 0.3, \end{cases} \quad \text{(H3)}$$

where $g_j = 4m_j m_{\rm target}(m_j + m_{\rm target})^{-2}$ is the maximum fraction of energy transfer in a head-on elastic collision. The stopping cross section, $S_j(E)$, is given by Sigmund (1981) as

$$S_j(E) = 4\pi a_{\rm sc}Z_jZ_{\rm target}e^2\frac{m_j}{m_j + m_{\rm target}}\varsigma_j(\epsilon_j), \quad \text{(H4)}$$

and the screening length, $a_{\rm sc}$, for interaction between nuclei is

$$a_{\rm sc} = 0.885a_{\rm Bohr}(Z_j^{2/3} + Z_{\rm target}^{2/3})^{-1/2}, \quad \text{(H5)}$$

where $a_{\rm Bohr} = 0.529$ Å is the Bohr radius. An approximation of the function, $\varsigma_j(\epsilon_j)$ is given by Matsunami et al. (1984) as

$$\varsigma_j(\epsilon_j) = \frac{3.441\sqrt{\epsilon_j}\ln[\epsilon_j + 2.718]}{1 + 6.35\sqrt{\epsilon_j} + \epsilon_j(6.882\sqrt{\epsilon_j} - 1.708)}, \quad \text{(H6)}$$

where the reduced energy, ϵ_j, is

$$\epsilon_j = \left(\frac{m_{\rm target}}{m_j + m_{\rm target}}\right)\left(\frac{a_{\rm sc}}{Z_jZ_{\rm target}e^2}\right)E. \quad \text{(H7)}$$

The function $\xi_j(\zeta_j)$, depends on the energy distribution deposited into the target, and we used the derivation by Nozawa et al. (2006) for $\zeta_j \in [0.3, 56]$:

$$\xi_j(\zeta_j) = \begin{cases} 0.2 & \zeta_j \leqslant 0.5, \\ 0.1\zeta_j^{-1} + 0.25(\zeta_j - 0.5)^2 & 0.5 < \zeta_j \leqslant 1, \\ 0.3(\zeta_j - 0.6)^2 & 1 < \zeta_j. \end{cases} \quad \text{(H8)}$$

ORCID iDs

Brian J. Fry https://orcid.org/0000-0002-2786-5667

References

Adams, S. M., Kochanek, C. S., Beacom, J. F., Vagins, M. R., & Stanek, K. Z. 2013, ApJ, 778, 164
Alvarez, L., Alvarez, W., Asaro, F., & Michel, H. 1980, Sci, 208, 1095
Andersen, H. H., & Bay, H. L. 1981, in Sputtering by Particle Bombardment. I. Physical Sputtering of Single-Element Solids, ed. B. Rainer (Berlin: Springer-Verlag), 145
Athanassiadou, T., & Fields, B. D. 2011, NewA, 16, 229
Augustson, K. C. 2019, arXiv:1912.06422
Balsara, D., Benjamin, R. A., & Cox, D. P. 2001, ApJ, 563, 800
Barkan, A., D'angelo, N., & Merlino, R. L. 1994, PhRvL, 73, 3093
Benítez, N., Maíz-Apellániz, J., & Canelles, M. 2002, PhRvL, 88, 081101
Bianchi, S., & Schneider, R. 2007, MNRAS, 378, 973
Binns, W. R., Israel, M. H., Christian, E. R., et al. 2016, Sci, 352, 677
Biscaro, C., & Cherchneff, I. 2014, A&A, 564, A25
Biscaro, C., & Cherchneff, I. 2016, A&A, 589, A132
Blondin, J. M. 2001, in AIP Conf. Proc. 565, Young Supernova Remnants, ed. S. S. Holt & U. Hwang (Melville, NY: AIP), 59
Blondin, J. M., & Ellison, D. C. 2001, ApJ, 560, 244
Blondin, J. M., Wright, E. B., Borkowski, K. J., & Reynolds, S. P. 1998, ApJ, 500, 342
Bocchio, M., Marassi, S., Schneider, R., et al. 2016, A&A, 587, A157
Bohdansky, J. 1984, NIMPRB, 2, 587
Bohren, C. F., & Huffman, D. R. 1983, Absorption and Scattering of Light by Small Particles (New York: Wiley)
Breitschwerdt, D., de Avillez, M. A., Feige, J., & Dettbarn, C. 2012, AN, 333, 486
Breitschwerdt, D., Feige, J., Schulreich, M. M., et al. 2016, Natur, 532, 73
Burkhart, B., Falceta-Gonçalves, D., Kowal, G., et al. 2009, ApJ, 693, 250
Castor, J., McCray, R., & Weaver, R. 1975, ApJL, 200, L107
Cherchneff, I. 2013, ESA Publ. Ser., 60, 175
Cherchneff, I., & Dwek, E. 2009, ApJ, 703, 642
Cherchneff, I., & Dwek, E. 2010, ApJ, 713, 1
Cherchneff, I., & Sarangi, A. 2011, in Proc. IAU Symp. 280, The Molecular Universe, ed. J. Cernicharo & R. Bachiller (Cambridge: Cambridge Univ. Press), 228
Cherchneff, I., & Sarangi, A. 2017, in ASP Conf. Ser. 508, The B[e] Phenomenon: Forty Years of Studies, ed. A. Miroshnichenko (San Francisco, CA: ASP), 57
Chevalier, R. A. 1974, ApJ, 188, 501
Chevalier, R. A. 1982, ApJ, 258, 790
Chevalier, R. A., Blondin, J. M., & Emmering, R. T. 1992, ApJ, 392, 118
Chow, V. W., Mendis, D. A., & Rosenberg, M. 1993, JGR, 98, 19
Cook, D. L., Berger, E., Faestermann, T., et al. 2009, LPI, 40, 1129
Davidson, P. A. 2001, An Introduction to Magnetohydrodynamics (Cambridge: Cambridge Univ. Press)
de Avillez, M. A., & Breitschwerdt, D. 2005, A&A, 436, 585
Doherty, C. L., Gil-Pons, P., Lau, H. H. B., Lattanzio, J. C., & Siess, L. 2014, MNRAS, 437, 195
Douvion, T., Lagage, P. O., & Cesarsky, C. J. 1999, A&A, 352, L111
Draine, B. T. 2003, ARA&A, 41, 241
Draine, B. T. 2011, Physics of the Interstellar and Intergalactic Medium (Princeton, NJ: Princeton Univ. Press)
Draine, B. T., & Salpeter, E. E. 1979, ApJ, 231, 77
Draine, B. T., & Sutin, B. 1987, ApJ, 320, 803
Drouin, D., Couture, A. R., Joly, D., et al. 2007, Scanning, 29, 92
Dubinski, J., Narayan, R., & Phillips, T. G. 1995, ApJ, 448, 226
Duffell, P. C. 2016, ApJ, 821, 76
Dwek, E. 2016, ApJ, 825, 136
Dwek, E., & Arendt, R. G. 1992, ARA&A, 30, 11
Dwek, E., Foster, S. M., & Vancura, O. 1996, ApJ, 457, 244
Efstathiou, G., Davis, M., White, S. D. M., & Frenk, C. S. 1985, ApJS, 57, 241
Ellis, J., Fields, B. D., & Schramm, D. N. 1996, ApJ, 470, 1227
Ellis, J., & Schramm, D. N. 1995, PNAS, 92, 235
Ellison, D. C., Drury, L. O., & Meyer, J.-P. 1997, ApJ, 487, 197
Feige, J. 2014, Doctoral Dissertation, Univ. Vienna, http://othes.univie.ac.at/35089/
Feige, J. 2016, PhuZ, 47, 220
Feige, J., Breitschwerdt, D., Wallner, A., et al. 2017, in 14th Int. Symp. on Nuclei in the Cosmos, NIC2016, ed. S. Kubono et al. (Tokyo: Physical Society of Japan), 010304
Feige, J., Wallner, A., Altmeyer, R., et al. 2018, PhRvL, 121, 221103
Feige, J., Wallner, A., Fifield, L. K., et al. 2013, EPJWC, 63, 03003
Field, G. B. 1975, in The Dusty Universe, ed. G. B. Field & A. G. W. Cameron (New York: Neale Watson Academic Publ. Inc.), 89
Fields, B., Ellis, J. R., Binns, W. R., et al. 2019, BAAS, 51, 410
Fields, B. D., Athanassiadou, T., & Johnson, S. R. 2008, ApJ, 678, 549
Fimiani, L., Cook, D. L., Faestermann, T., et al. 2012, LPI, 43, 1279
Fimiani, L., Cook, D. L., Faestermann, T., et al. 2014, LPI, 45, 1778
Fimiani, L., Cook, D. L., Faestermann, T., et al. 2016, PhRvL, 116, 151104
Fitoussi, C., Raisbeck, G. M., Knie, K., et al. 2008, PhRvL, 101, 121101
Fitting, H.-J. 1974, PSSAR, 26, 525
Fremling, C., Sollerman, J., Taddia, F., et al. 2016, A&A, 593, A68
Freytag, B., Steffen, M., & Dorch, B. 2002, AN, 323, 213
Fry, B. J., Fields, B. D., & Ellis, J. R. 2015, ApJ, 800, 71
Fry, B. J., Fields, B. D., & Ellis, J. R. 2016, ApJ, 827, 48
Fuchs, B., Breitschwerdt, D., de Avillez, M. A., Dettbarn, C., & Flynn, C. 2006, MNRAS, 373, 993
Fürst, E., & Reich, W. 2004, in The Magnetized Interstellar Medium, ed. B. Uyaniker, W. Reich, & R. Wielebinski (Göttingen: Copernicus Publ.), 141
Galtier, S. 2016, Introduction to Modern Magnetohydrodynamics (Cambridge: Cambridge Univ. Press)
Goldreich, P., & Sridhar, S. 1995, ApJ, 438, 763
Grard, R. J. L. 1973, JGR, 78, 2885
Greengard, L., & Lee, J.-Y. 2004, SIAMR, 46, 443
Haid, S., Walch, S., Naab, T., et al. 2016, MNRAS, 460, 2962
Haines, G. V., & Jones, A. G. 1988, GeoJI, 92, 171
Hamilton, A. J. S. 2000, MNRAS, 312, 257
Hamilton, A. J. S. 2015, FFTLog: Fast Fourier or Hankel Transform, Astrophysics Source Code Library, ascl:1512.017
Han, J. L., Gao, X. Y., Sun, X. H., et al. 2014, in IAU Symp. 296, Supernova Environmental Impacts, ed. A. Ray & R. A. McCray (Cambridge: Cambridge Univ. Press), 202
Herant, M., & Woosley, S. E. 1994, ApJ, 425, 814
Herwig, F. 2005, ARA&A, 43, 435
Hoffman, R. D., Müller, B., & Janka, H.-T. 2008, ApJL, 676, L127
Horanyi, M., & Goertz, C. K. 1990, ApJ, 361, 155
Hyde, M., & Pecaut, M. J. 2018, AN, 339, 78
Inoue, T., Yamazaki, R., & Inutsuka, S.-i. 2009, ApJ, 695, 825
Iroshnikov, P. S. 1964, SvA, 7, 566
Jackson, J. D. 1998, Classical Electrodynamics (3rd ed.; Weinheim: Wiley-VCH)
Janev, R. K., Ralchenko, Y. V., Kenmotsu, T., & Hosaka, K. 2001, JNuM, 290, 104
Janka, H.-T., Melson, T., & Summa, A. 2016, ARNPS, 66, 341
Janka, H.-T., Müller, B., Kitaura, F. S., & Buras, R. 2008, A&A, 485, 199
Jones, A. P., Tielens, A. G. G. M., & Hollenbach, D. J. 1996, ApJ, 469, 740
Jones, S., Röpke, F. K., Pakmor, R., et al. 2016, A&A, 593, A72
Kachelrieß, M., Neronov, A., & Semikoz, D. V. 2015, PhRvL, 115, 181103
Kimura, H., & Mann, I. 1998, ApJ, 499, 454
Kirchschlager, F., Schmidt, F. D., Barlow, M. J., et al. 2019, MNRAS, 489, 4465
Klein, R. I., McKee, C. F., & Colella, P. 1994, ApJ, 420, 213
Knie, K., Korschinek, G., Faestermann, T., et al. 1999, PhRvL, 83, 18
Knie, K., Korschinek, G., Faestermann, T., et al. 2004, PhRvL, 93, 171103
Kolmogorov, A. N. 1941, DoSSR, 32, 16
Korschinek, G., & Faestermann, T. 2019, NIMPB, 438, 148
Korschinek, G., Faestermann, T., Knie, K., & Schmidt, C. 1996, Radiocarbon, 38, 68
Kozasa, T., Nozawa, T., Tominaga, N., et al. 2009, in ASP Conf. Ser. 414, Cosmic Dust—Near and Far, ed. T. Henning, E. Grün, & J. Steinacker (San Francisco, CA: ASP), 43

Kraichnan, R. H. 1965, PhFl, 8, 1385
Lafon, J.-P. J., Lamy, L., & Millet, J. 1981, A&A, 95, 295
Laming, J. M., & Hwang, U. 2003, ApJ, 597, 347
Lau, R. M., Herter, T. L., Morris, M. R., Li, Z., & Adams, J. D. 2015, Sci, 348, 413
Lide, D. R. 2008, in CRC Handbook of Chemistry and Physics: A Ready-reference Book of Chemical and Physical Data, ed. D. R. Lide (89th ed.; Boca Raton, FL: CRC Press)
Ludwig, P., Bishop, S., Egli, R., et al. 2016, PNAS, 113, 9232
Ma, Y. K., Ng, C.-Y., Bucciantini, N., et al. 2016, ApJ, 820, 100
Maeda, Y., Baganoff, F. K., Feigelson, E. D., et al. 2002, ApJ, 570, 671
Mamajek, E. E. 2016, in IAU Symp. 314, Young Stars & Planets Near the Sun, ed. J. H. Kastner, B. Stelzer, & S. A. Metchev (Cambridge: Cambridge Univ. Press), 21
Matsunami, N., Yamamura, Y., Itikawa, Y., et al. 1984, ADNDT, 31, 1
Matthaeus, W. H., & Goldstein, M. L. 1982, JGR, 87, 6011
McKee, C. F., & Draine, B. T. 1991, Sci, 252, 397
McKee, C. F., Hollenbach, D. J., Seab, G. C., & Tielens, A. G. G. M. 1987, ApJ, 318, 674
McNally, C. P. 2011, MNRAS, 413, L76
Melott, A. L., Thomas, B. C., Kachelrieß, M., Semikoz, D. V., & Overholt, A. C. 2017, ApJ, 840, 105
Meyer-Vernet, N. 1982, A&A, 105, 98
Mezger, P. G., Zylka, R., Salter, C. J., et al. 1989, A&A, 209, 337
Micelotta, E. R., Dwek, E., & Slavin, J. D. 2016, A&A, 590, A65
Murray, N., Weingartner, J. C., & Capobianco, C. 2004, ApJ, 600, 804
Nadezhin, D. K. 1985, Ap&SS, 112, 225
Nath, B. B., Laskar, T., & Shull, J. M. 2008, ApJ, 682, 1055
Neuhäuser, R., Gießler, F., & Hambaryan, V. V. 2019, MNRAS, in press
Northrop, T. G., & Morfill, G. E. 1984, AdSpR, 4, 63
Nozawa, T., Kozasa, T., & Habe, A. 2006, ApJ, 648, 435
Nozawa, T., Kozasa, T., Habe, A., et al. 2007, ApJ, 666, 955
Ostriker, J. P., & McKee, C. F. 1988, RvMP, 60, 1
Padmanabhan, T. 2001, in Theoretical Astrophysics—Vol. 2, Stars and Stellar Systems, ed. T. Padmanabhan (Cambridge: Cambridge Univ. Press), 594
Petit, P., Aurière, M., Konstantinova-Antova, R., et al. 2013, LPN, 857, 231
Poelarends, A. J. T., Herwig, F., Langer, N., & Heger, A. 2008, ApJ, 675, 614
Pollack, J. B., Hollenbach, D., Beckwith, S., et al. 1994, ApJ, 421, 615
Pumo, M. L. 2010, MSAIS, 14, 115
Pumo, M. L., Turatto, M., Botticella, M. T., et al. 2009, ApJL, 705, L138
Sarangi, A., & Cherchneff, I. 2013, ApJ, 776, 107
Sarangi, A., & Cherchneff, I. 2015, A&A, 575, A95
Savchenko, V., Kachelrieß, M., & Semikoz, D. V. 2015, ApJL, 809, L23
Scalo, J. M., Haff, P. K., Switkowski, Z. E., & Tombrello, T. A. 1977, PhLB, 70, 137
Schulreich, M., Breitschwerdt, D., Feige, J., et al. 2018, Galax, 6, 26
Schulreich, M. M., Breitschwerdt, D., Feige, J., & Dettbarn, C. 2017, A&A, 604, A81
Sedov, L. I. 1959, Similarity and Dimensional Methods in Mechanics (New York: Academic)
Shklovskij, I. S. 1969, Supernovae (New York: Interscience Publishers)
Shukla, P. K., & Mamun, A. A. 2002, in Introduction to Dusty Plasma Physics, ed. P. K. Shukla & A. A. Mamun (Bristol: IOP Publ.)
Shull, J. M. 1977, ApJ, 215, 805
Shull, J. M. 1978, ApJ, 226, 858
Sigmund, P. 1981, in Sputtering by Particle Bombardment. I. Physical Sputtering of Single-Element Solids, ed. R. Behrisch (Berlin: Springer), 9
Silvia, D. W., Smith, B. D., & Shull, J. M. 2010, ApJ, 715, 1575
Silvia, D. W., Smith, B. D., & Shull, J. M. 2012, ApJ, 748, 12
Sluder, A., Milosavljević, M., & Montgomery, M. H. 2018, MNRAS, 480, 5580
Smartt, S. J., Eldridge, J. J., Crockett, R. M., & Maund, J. R. 2009, MNRAS, 395, 1409
Sørensen, M., Svensmark, H., & Gråe Jørgensen, U. 2017, arXiv:1708.08248
Sorriso-Valvo, L., Carbone, V., Veltri, P., et al. 1999, GeoRL, 26, 1801
Spitzer, L., Jr. 1941, ApJ, 93, 369
Taylor, G. 1950, RSPSA, 201, 159
Tielens, A. G. G. M., Seab, C. G., Hollenbach, D. J., & McKee, C. F. 1987, ApJL, 319, L109
Truelove, J. K., & McKee, C. F. 1999, ApJS, 120, 299
Uyaniker, B., Reich, W., Yar-Uyaniker, A., Kothes, R., & Fürst, E. 2004, in The Magnetized Interstellar Medium, ed. B. Uyaniker, W. Reich, & R. Wielebinski (Göttingen: Copernicus Publ.), 153
Wallin, B. K., Watson, W. D., & Wyld, H. W. 1998, ApJ, 495, 774
Wallner, A., Feige, J., Kinoshita, N., et al. 2016, Natur, 532, 69
Wanajo, S., Janka, H.-T., & Müller, B. 2013a, ApJL, 774, L6
Wanajo, S., Janka, H.-T., & Müller, B. 2013b, ApJL, 767, L26
Wanajo, S., Nomoto, K., Janka, H. T., Kitaura, F. S., & Müller, B. 2009, ApJ, 695, 208
Wang, C.-Y., & Chevalier, R. A. 2002, ApJ, 574, 155
Watson, W. D., Wiebe, D. S., & Crutcher, R. M. 2001, ApJ, 549, 377
West, J. L., Jaffe, T., Ferrand, G., Safi-Harb, S., & Gaensler, B. M. 2017, ApJL, 849, L22
Wiebe, D. S., & Watson, W. D. 1998, ApJL, 503, L71
Williams, B. J., & Temim, T. 2016, Handbook of Supernovae (Living Reference Work Entry) (New York: Springer)
Wilson, D. K. 1998, Turbulence Models and the Synthesis of Random Fields for Acoustic Wave Propagation Calculations, Tech. Rep. ARL-TR-1677 (Adelphi, MD: Army Research Laboratory)
Woosley, S. E., & Heger, A. 2015, ApJ, 810, 34
Xu, S., & Lazarian, A. 2017, ApJ, 850, 126
Zel'dovich, Y. B. 1970, A&A, 5, 84
Ziegler, J. F., & Biersack, J. P. 1985, in Treatise on Heavy-Ion Science, ed. D. A. Bromley (New York: Springer), 93
Ziegler, J. F., Ziegler, M. D., & Biersack, J. P. 2010, NIMPB, 268, 1818